EFFECTS OF POLLEN AND METAL OXIDE POLLEN REPLICA MORPHOLOGY ON TAILORABLE DRY AND WET ADHESION

A Dissertation
Presented to
The Academic Faculty

by

Donglee Shin

In Partial Fulfillment
of the Requirements for the Degree
Doctor of Philosophy in the
School of Chemical and Biomolecular Engineering

Georgia Institute of Technology
May 2017

EFFECTS OF POLLEN AND METAL OXIDE POLLEN REPLICA MORPHOLOGY ON TAILORABLE DRY AND WET ADHESION

Approved by:

Dr. J. Carson Meredith, Advisor
School of Chemical and Biomolecular Engineering
Georgia Institute of Technology

Dr. Sven Behrens
School of Chemical and Biomolecular Engineering
Georgia Institute of Technology

Dr. Elsa Reichmanis
School of Chemical and Biomolecular Engineering
Georgia Institute of Technology

Dr. Yulin Deng
School of Chemical and Biomolecular Engineering
Georgia Institute of Technology

Dr. Meisha Shofner
School of Materials Science and Engineering
Georgia Institute of Technology

Date Approved: [March 29, 2017]

This work is dedicated to my God and family.

ACKNOWLEDGEMENTS

I would like to thank my family for giving me endless love and support; without their support, I would not be where I am today. To my parents, Ga Chul and Jung Hee, the sacrifices you have made to provide me with the opportunity to study in U.S. have always motivated me to succeed, and their love and encouragement have been constant sources of great comfort to me when times were difficult. I am also thankful to my younger sister, Dae ra, for her endless love and encouragement throughout the years. Finally, to my grandmother, Seok Hwa, your love and support lead me to success in this journey.

I would like to express my deepest gratitude to my advisor, Dr. Carson Meredith for his overwhelming guidance, patience, and support in this work. I feel very fortunate to have had him as my advisor and to have had the opportunity to learn from him. I would like to thank my committee members, Dr. Elsa Reichmanis, Dr. Meisha Shofner, Dr. Sven Behrens, and Dr. Yulin Deng for their time and assistance in helping me complete this work.

I would like to extend my gratitude to all the current and past members of Meredith group, Dr. Ismael Gomaz, Dr. Haisheng Lin, Dr. Shanghong Xu, Dr. Jie Wu, Dr. Timi Fadiran, Dr. Natalie Girouard, Dr. Yi Zhang, Zhihao Qu, Soncheng Wang, Chinmay Satam, Scott Essenmacher, for sharing their knowledge and support along with enjoyable moments.

I would like to thank my girlfriend Min Hea and her family, Min Joo and Todd O'Hara. Their love and encouragement help me to overcome the difficulty of living away from home. Special thanks to Min Hea Kim, whose love and support have made this work possible.

TABLE OF CONTENTS

LIST OF TABLES

LIST OF FIGURES

SUMMARY

The surface adhesion of micro-particles has been investigated with respect to many natural and environmental phenomena as well as engineering applications including drug delivery, coating, paints, separations, and sensors. Especially, the surface adhesion of smooth micro-particles with simple shapes (spheres, cylinders, hexahedrons) has been well-studied for the last four or five decades. However, there are far fewer studies of the adhesion of micro-particles with complex surface morphology. In this study, pollen grains are used as experimental samples and bio-templates since the pollen grains have chemically and physically stable surface with wide shape diversity. The purpose of this study is to understand the dry and wet adhesive mechanisms of pollen and pollen replica adhesion to tailor the magnitude and rate-dependence of the adhesion. During the investigation of the mechanisms, we have learned: i) how to analyze quantitatively and model the attraction force of micro-particles with complex surface micro- and nano-scale morphology ii) the effects of both particle morphology and liquid physical properties on wet adhesion of micro-particles on surfaces iii) how to tune the rate-dependence of the wet adhesion via control of surface morphology and the structure of liquid phases. Not only do these discoveries offer insight into the mechanisms operative in Nature, but they also offer inspiration for new adhesion mechanisms for micro-particles, particularly those that are responsive to the dynamics of particle detachment speed.

CHAPTER 1. INTRODUCTION AND BACKGROUND

1.1 Influence of Surface Topography on Adhesion and Bio-adhesion

Micro- or nano-structured surfaces have been studied widely due to the fascinating functions they enable, such as anti-wetting [1], anti-icing [2], water droplet harvesting [3] and mobilization [4], photonic color [5], turbulent fluid drag reduction [6], and glueless adhesion [7]. While man-made approaches for these functions exist, each of these functions is also naturally-occurring. The surface structures of animals and plants have evolved in many instances to confer specific functionalities that improve survival or reproduction. For example, lotus leaves possess a superhydrophobic (water-repellent) surface attributed to a micro- and nano-scale hierarchical structure (Figure 1 a and b) [8, 9], and this feature maximizes the efficiency of photosynthesis by facilitating self-cleaning mechanism. The micro-patterned structures of hydrophobic and hydrophilic regions on the back of desert beetles promote the water condensation to collect water droplets from humid air (Figure 1 c and d) [10]. Some butterflies utilize structural colors, created by controlling the transportation of light via photonic nanostructures, for vivid and bright colors of their wings with low energy consumption (Figure 1 e and f) [11]. The aligned riblet structures on shark skin reduce the drag experienced by fast-swimming sharks in turbulent flow (Figure 1 g and h) [12]

Many plants and animals have evolutionarily optimized surface structures that create strong and functional adhesion for locomotion or transportation. For example, the multi-branched structure of gecko foot-hairs creates exceptionally strong adhesion to enable climbing on both smooth and rough surfaces without an adhesive secretion [13].

The hairy structures (200-500 nm long and 15 nm thick) on the gecko setae (30-130 μm long) allow the foot pads to create contact area sufficient to sustain the gecko's body weight even on vertical walls. Tree frogs can strongly adhere to wet and rough surfaces. The adhesive pads of tree frogs have hexagonal cells (approximately 10μm diameter) separated by deep channels (1μm wide) filled with a mucus secretion. The micro-structured channels are the paths for distributing mucus over the whole contact area between the adhesive pad and a contact surface, and the channels also work to drain water, enabling attachment on water coated surfaces [14]. Insects have both hairy and smooth adhesive pads, whose adhesion is mediated by thin layers of adhesive secretions [15]. The tip radius of structures on the hairy adhesive pad are roughly in the size ranging from 1 μm to 10 μm and these can attach at multiple points to create a large contact area on a rough surface [15, 16], similar to the action of the gecko setae. The smooth adhesive pad, which is a "pillow-like" soft structure that consists of branching fibrils and the outer cuticle layer [17], can also adapt to surface roughness features to create large contact areas for strong adhesion. Pollens from different plant species display a remarkable variety of ornamentations with a unique size, shape, and density on their surface exine shell. When pollens interact with a structured flower stigma, their surface features cause pressure-sensitive adhesion mediated by mechanical interlocking [18]. Pollen grains exhibiting structural ornamentations have been shown to adhere strongly to the stigma surfaces within the same botanical family [19], which is thought to facilitate reproduction.

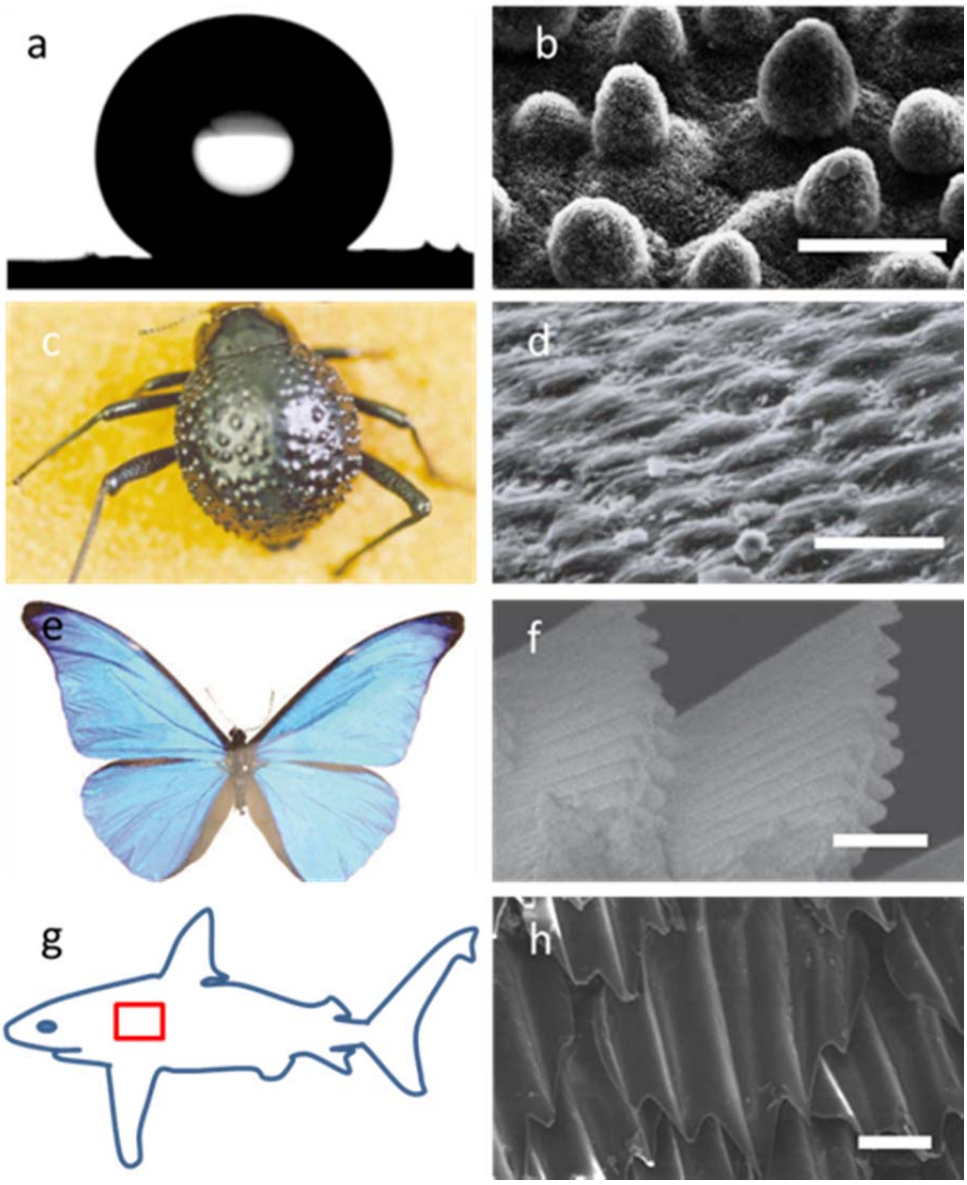

Figure 1 – a Water droplet on a lotus leaf CA=152° (reproduced with permission from [8]), b scanning electron microscopy (SEM) image of the lotus leaf (reproduced with permission from [9]), c photograph and d SEM image of the water-harvesting surface of the desert beetle (reproduced with permission from [10]), e photograph and f SEM image of distinctive iridescent blue color of the wings of Morpho butterfly (reproduced with permission from [11]), and g Cartoon and h SEM image of the scale structure of shark skin (reproduced with permission from [12]). Scale bars= 20 μm b, 10 μm d, 400 nm f, and 50μm h.

Using nature as well as man-made materials, this contribution reviews the effects of micro- and nano-scale topography on adhesion. Numerous researchers have studied the adhesion mechanisms of simple geometries, such as plane-plane, sphere-sphere, cone-cone, sphere-plane, sphere-cylinder, and cone-plane over the last several decades [20–26]. Based on this background knowledge, studies of the geometrical influence on adhesion have been more recently expanding to treat surfaces with complex fine features. The investigation of bio-adhesion, such as in the examples mentioned above, has been an important part of an emerging understanding of the effects of micro- and nano-scale topography on adhesion. Herein, we discuss the basic physical principles of adhesion with simple geometric models since the adhesion of complex structured surfaces are also based on the same physical principles. These include van der Waals (vdW), capillary and viscous forces (Section 2). Then, we discuss how the different surface geometries (hairy, smooth, and echinate) affect adhesive mechanisms and focus on the dependence of bio-adhesion on substrate structure (Section 3). We also review recent efforts to produce anti-adhesive surfaces based on surface topography designed from natural adhesive phenomena (Section 4).

1.2 Physical Principles of Adhesion

Animals and plants utilize transitory (non-permanent) adhesive force for transport and locomotion [27, 28], and this temporary adhesion is strongly affected by the topography of the adhesive surface. Adhesive mechanisms related to transitory bio-adhesion can be classified roughly into two categories: i) dry adhesion based on intermolecular forces and ii) wet adhesion based on liquid-mediated capillary forces. These mechanisms are also operative in synthetic adhesives in manmade materials, such

as pressure-sensitive adhesives [29], latex paints [30], ink toner and powder coatings [31]. In this section, we will discuss the physical principles of both dry and wet adhesive mechanisms with representative simple geometry models.

1.2.1 Dry Adhesion

In general, the adhesive force of neutral surfaces in a 'dry' atmosphere, such as nitrogen or vacuum, may comprise van der Waals (vdW) interactions, and hydrogen, covalent, or metallic bonds [32]. The energy of vdW interactions is normally much smaller than covalent or hydrogen bonds. However, the vdW interaction plays a prominent role in determining the attractive force magnitude of surfaces and colloids because the vdW interaction has a longer range (from 0.2 to 10 nm) than the other inter- or intramolecular bonding (covalent, hydrogen, and metallic bonding) scales (normally between 0.1and 0.2 nm) [33]. Even though there is no universal model that accounts for the influence of all contributions (e.g., elastic moduli, surface energy, temperature, relative humidity, and Hamaker constant) on vdW interactions, the following adhesion models for simple geometry help us to understand the physical principles of dry adhesion. Common classical models to estimate the adhesion force between two elastic spheres (or sphere and planar surfaces) originated from Hertzian theory [34]. Heinrich Hertz in 1882 developed a model for the contact area (a) of two elastic spheres (of radii of R_1 and R_2 with elastic moduli K) with external loading force (F) [33]:

$$a = \left(\frac{FR}{K}\right)^{1/3}, \tag{1}$$

where $R = R_1 R_2/(R_1 + R_2)$.

In Hertzian theory, the intermolecular attraction between contact surfaces was ignored, so the contact area is apparently zero when there is no (or negative) external load. In 1971, Johnson, Kendall, and Roberts (JKR) developed a theory to estimate the adhesion between two solid surfaces [35]. They observed that the experimentally measured contact areas were larger than values estimated by Hertz theory, and they confirmed that the solid surfaces still adhered under zero or small negative external loading force. They proposed that the surface interaction affects both deformed shape and overall loading force, which is represented by the sum of the external loading force and adhesion of the surfaces. The deformed contact area was derived by the following equation [36]:

$$a^3 = \frac{R}{K}\left(F + 3\pi W_{12}R + (6\pi W_{12}RF + (3\pi W_{12}R)^2)^{\frac{1}{2}}\right), \quad (2)$$

where F is external load and W_{12} is work of adhesion, which is the work done in separating a unit area of the interface. For a sphere (radius of sphere, $R_s = R_1$) on a flat surface ($R_2 = \infty$), the adhesion or pull-off force can be derived as [37]

$$F_{JKR} = \frac{3}{2}\pi R_s W_{12}. \quad (3)$$

Unlike the JKR case, Derjaguin Muller and Toporov (DMT) assumed that the deformed shape of contact is not affected by surface interaction, but only affected by the surface interaction like the Hertz theory [38]. Therefore, the deformed contact area could be derived as [36]:

$$a^3 = \frac{R}{K}(F + 2\pi W_{12}R), \tag{4}$$

and adhesion or pull-off force of a sphere on a flat surface can be derived as [37]

$$F_{DMT} = 2\pi R_s W_{12}. \tag{5}$$

The JKR and DMT models consider the deformation of the contact area, but neither model accounts for the influence of separation distance on adhesion. When the contact surfaces have roughness or geometrical features, the assumption of complete contact is no longer valid and the separation distance of the surfaces must be considered [39]. The separation distance is the most significant factor to define adhesive force magnitude in the non-retarded region (separation distance below 5 nm) [33]. Therefore, the adhesion models for rough or structured surfaces often use the Hamaker approach as a starting point. Hamaker proposed that the adhesion between two spherical particles can be estimated by the integration of the van der Waals pair potential between all atoms in one body and all atoms in the other body [20]. In his study, the vdW interaction between a sphere and a flat surface was derived as

$$F_{vdw} = -\frac{A_{132}}{24R_c}\left(\frac{2}{x} - \frac{1}{x^2} - \frac{2}{x+1} - \frac{1}{(x+1)^2}\right), \tag{6}$$

where A_{132} is the material-dependent nonretarded Hamaker constant, which represents the magnitude of interaction of the two interacting bodies (1 and 2) consisting of atoms with induced dipoles across a medium (3). The x in equation (6) represents the ratio between the contact radius (R_c), and half of the cutoff separation distance (D_0), which is the predicted separation distance of contacting surfaces. (Some references approximate the

cut off distance at around 0.3-0.4 nm [39, 40], but others evaluate it as 0.165 nm [13, 33]) The Hamaker constant can be simplely determined by [33]

$$A = \pi^2 C p_1 p_2, \tag{7}$$

where p_1 and p_2 are the number of atoms in unit volume of the two bodies (1 and 2), and *C* is the coefficient in the atom-atom pair potential. The Eq (2.1.6) can be simplified to Eq (2.1.8) in the limit of of $x << 1$ [33].

$$F_{vdw} = \frac{A_{132} R_c}{6D^2}, \tag{8}$$

where *D* is separation distance.

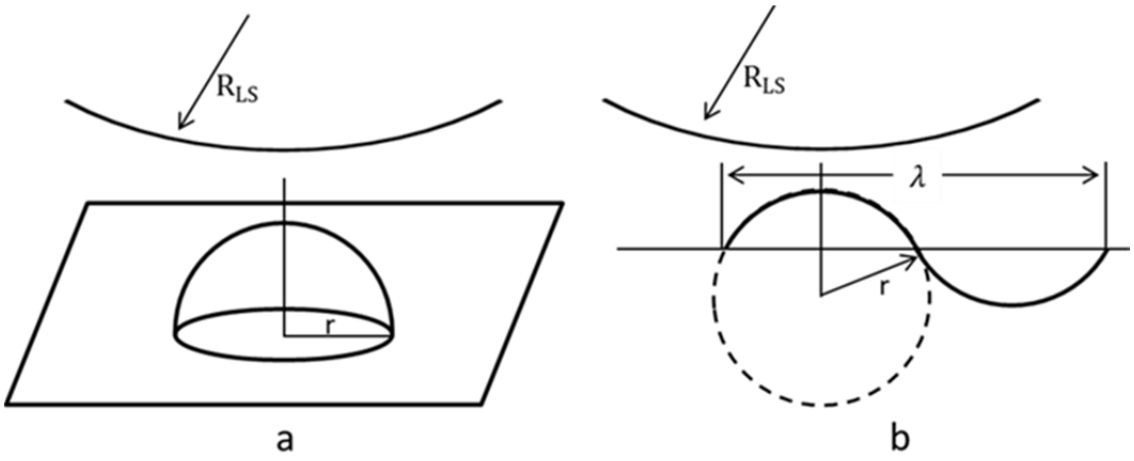

Figure 2 – Schematic illustration of the geometry proposed by Rumpf a and Rabinovish b.

It is well-known that the surface pattern and roughness reduce the adhesion between surfaces or a spherical particle and a planar surface [41, 42]. Rumpf's model is a common and simple model based on Hamaker approach to consider the effect of

nanoscale surface roughness on adhesion [43]. This model estimates the adhesion between a large spherical particle (radius, R_{LS}) and a flat surface covered with small hemispherical asperities (radius, *r*), and normal alignment of the center of the particle and asperity is assumed (Figure 2 a). Rumpf's model consists of two terms as shown in the following formula [43]:

$$F_{Rumpf} = \frac{A_{132}}{6D_0^2}\left[\frac{rR_{LS}}{r+R_{LS}} + \frac{R_{LS}}{\left(1+\frac{r}{D_0}\right)^2}\right], \quad (9)$$

where D_0 is the "cutoff" distance. The first term represents the adhesion between the particle and hemispherical asperity in contact, and the second term represents the "noncontact" attractive interaction between the particle and flat surface with separation distance at the radius of hemisphere asperity. Rabinovich et al. found that Rumpf's model is not accurate in real systems with low roughness surface since it requires the center of a small hemisphere to be at the surface as shown in Figure 2 a [40]. In the real systems, the center is located below the surface, and multiple surface asperities will have contact with the large spherical particle. They proposed the approximation of this case with root-mean-square (rms) roughness and peak-to-peak distance (λ) (Figure 2 b) as shown in the following equation [40]:

$$F_{Rabin.} = \frac{A_{132}R_{LS}}{6D_0^2}\left[\frac{1}{1+\left(\frac{32R_{LS}k_1 rms}{\lambda^2}\right)} + \frac{1}{\left(1+\frac{k_1 rms}{D_0}\right)^2}\right], \quad (10)$$

where k_1 is a proportionality factor determined to be 1.817. In conventional adhesion and bio-adhesion, surfaces can display surface roughness with a wide variety of structures

and shapes, and the previous dry adhesion models are limited because of assumptions made about the shape or distribution of asperities. Recent dry adhesion models have tried to account for the interaction of complex contact shapes [16, 44], asymmetric structures [45], multiple contacts [46], and mechanical interlocking [47].

1.2.2 Wet Adhesion

In practical industrial and natural applications, wet adhesion is common. Strong wet adhesion driven by water condensation or by the presence of thin liquid lubricant on the contact surfaces is a critical issue in operating of fine-scale devices, including as atomic force microscopy, magnetic storage devices, and fuel injectors [48]. For locomotion of animals, wet adhesion normally can create larger contact area on a rough surface compared to a dry surface due to strong capillary adhesion driven by the presence of a liquid secretion [49]. The mediating liquid can increase contact between the adhesive pad and a rough surface by filling into the gaps between the pad and surface. The wet adhesion force can be split into two main components, which are capillary (meniscus) and viscous forces [50], as shown in equation (11).

$$F_{Wet\ adhesion} = F_{Capillary\ force} + F_{Viscous\ force}. \tag{11}$$

The vdW interaction may dominate wet adhesion in the case of very thin films (less than 10 nm), but its contribution is in most cases smaller than the capillary or viscous forces. The contribution of these primary components to wet adhesion can be determined by considering the meniscus curvatures, dynamics and viscosity of liquid films [48].

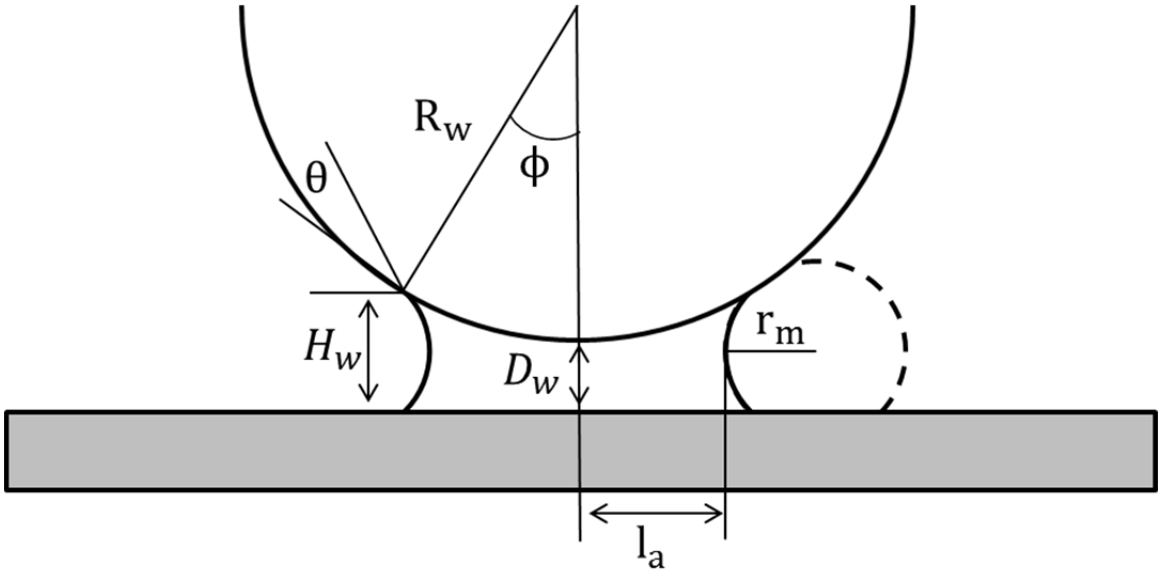

Figure 3 – Schematic of a meniscus bridge present at the interface between a sphere and a plane surfaces.

The capillary force is caused by a liquid meniscus (bridge) between two separated surfaces, and the curvature of the liquid meniscus is characterized by two radii which are the azimuthal radius (l_a) and the meridional radius (r_m), indicated Figure 3. The total capillary force between a sphere (radius, R_w) and a flat surface is defined as the summation of the surface tension and Laplace pressure contributions as shown in the following equation for a symmetric contact angle [48, 51]:

$$F_{Capillary\ force} = \Delta P \Omega + 2\pi R_w \gamma \sin\phi \sin(\phi + \theta), \quad (12)$$

where Ω is the meniscus area, ϕ is filling angle, θ is contact angle, γ is the surface tension of the liquid, and ΔP is Laplace pressure, estimated by the Young-Laplace equation (equation (13)).

$$\Delta P = \gamma(\frac{1}{l_a} - \frac{1}{r_m}). \quad (13)$$

The Young-Laplace equation describes the capillary pressure difference between two static phases. The surface tension and Laplace pressure forces explain the contribution of the capillary liquid bridges to wet adhesion, but neither expression has dynamic terms. The contribution of hydrodynamic response can be estimated by a viscous force model, often called "Stefan adhesion" [50]. The viscous term of wet adhesion is a significant component of the wet adhesion mediated by highly viscous liquid capillary bridges, but also it can dominate for liquids of modest viscosity at high shear rate [52]. The viscous force acting on a sphere and a flat surface connected by a capillary bridge (Figure 3) can be approximated by Equation (14). [48]

$$F_{Viscous\ force} = 6\pi\eta {R_w}^2 \left[1 - \frac{D_w}{H_w}\right]^2 \frac{1}{D_w}\frac{dD_w}{dt}, \quad (14)$$

where η is the viscosity, D_w is the distance between a sphere and a flat surface, R_w is the radius of the spheres, H_w is meniscus height, and dD_w/dt is the separation rate. The total wet adhesion between a sphere and a flat surface can be estimated by the summation of Equation (12) and (14).

The previous capillary (Equation (12)) and viscous (Equation (14)) force models are commonly used to estimate wet adhesion of a sphere and planar surface for simplicity, but the models fail to estimate wet adhesion for rough and patterned surfaces [53]. The topographical effect on capillary force is strongly dependent on the height of the liquid meniscus (the thickness of liquid) as shown in Figure 4. When the meniscus height is

larger than hemispherical asperity as shown in Figure 4 a (r_l > H), the contact line and the curvatures of the meniscus are determined by the larger separation distance H. The previous Equation (12) (sphere and flat surface model) is still valid as long as the increased separation distance is accounted. However, when meniscus height is smaller than the hemispherical asperity (Figure 4 b), the wet adhesion model between two spheres (a large sphere and a small hemisphere) should be considered. The capillary force for interaction between two spheres was studied by Willett et al. [54] and Rabinovich et al. [55]. For multiple asperity contacts, Bhushan proposed a capillary force model of a randomly rough surface in contact with a smooth surface with a continuous liquid film as shown in Figure 4 c [56]. Both contacting and near-contacting asperities have a liquid meniscus, peak radii (of the asperities) are assumed constant, and peak heights are assumed to follow a Gaussian distribution. By the summation of the wet adhesion on the asperities, the total wet adhesion of the surface is given as

$$F_{Capillary\ force} = 2\pi R_p \gamma_l (1 + \cos\theta_l) N \int_{d-h_l}^{\infty} p(z) dz, \quad (15)$$

where N is the total number of liquid bridges, R_p is the mean peak radius, γ_l is the liquid surface tension, θ_l is the contact angle of the liquid in contact with the rough surface, d is the interplanar separation [52], h_l is the thickness of liquid film, and $p(z)$ is the peak height distribution function.

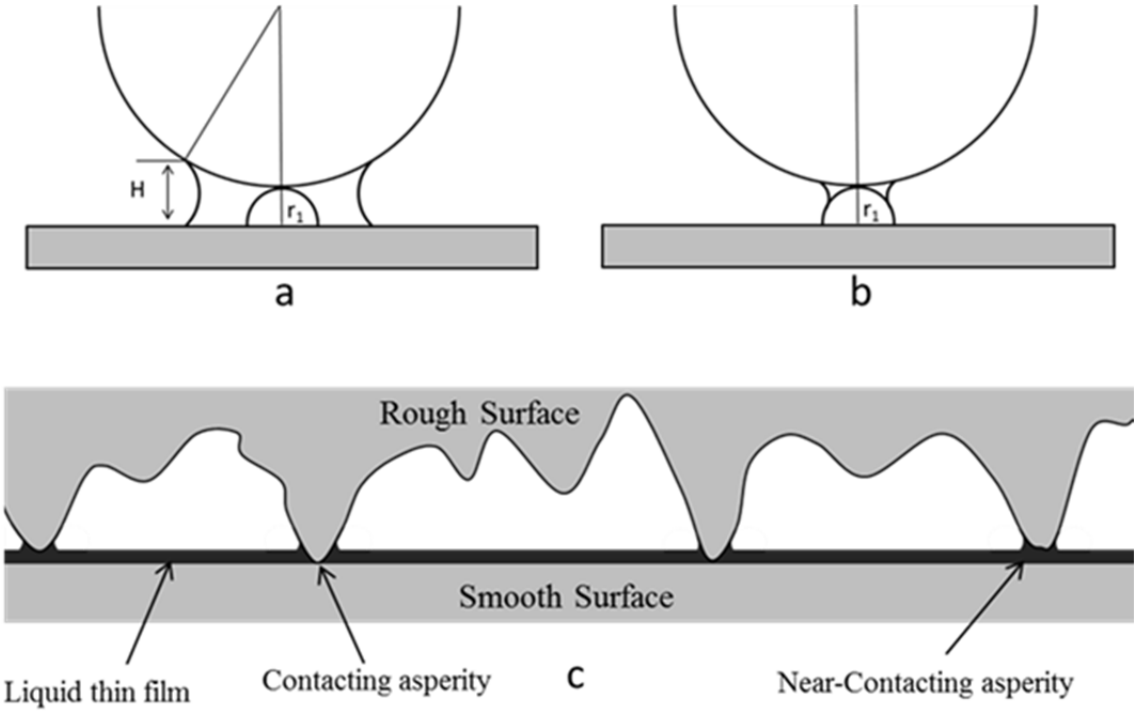

Figure 4 – Schematic of a liquid meniscus when H > r_1 a; H < r_1 b. c Schematic for a rough surface in contact with a flat surface coated by a thin liquid film.

The viscous force acting between a sphere and a flat surface is generated by hydrodynamic drainage of liquid in the gap separating the surfaces. The surface topography affects the viscous force magnitude by creating slip or partial slip boundary conditions [57]. Remarkable hydrodynamic force reduction has been observed in capillaries on micro- and nano-structured surfaces [58, 59], such as structured superhydrophobic surfaces. The reduction is commonly explained by the slip boundary of liquid on trapped air pockets [60]. The classical viscous model (Equation (14)) is originated from Reynolds' lubrication theory with non-slip boundary conditions. Vinogradova initially proposed multiplying a correction factor (f^*) to account for the effect of a partial slip boundary, assuming creeping flow and the same slip length b for the both surfaces [61].

$$f* = \frac{D_w}{3b}\left[(1+\frac{D_w}{3b})\ln\left(1+\frac{6b}{D_w}\right)-1\right], \quad (16)$$

In practice, it is still challenging to estimate precisely the effective slip length because it is dependent on multiple factors, such as wettability, surface structure, and rheological properties of the liquid. But, recent studies have made meaningful progress in understanding the influence of diverse surface structures on boundary conditions of the viscous force model [62, 63].

1.3 Functional Morphology of Bio-adhesive Surfaces

The evolutionarily adapted surfaces of animals and plants show how nature utilizes structured surfaces for functional adhesion. For example, the adhesive pads of animals support body weight on varying surfaces, such as smooth or rough, hydrophilic or hydrophobic, and clean or contaminated [64]. The structured adhesive pads, secretions, or both have a critical function to adhere on surfaces strongly but reversibly for locomotion [28]. Plants also use structural surfaces and bio-adhesives. For example, pollen grains use complex surface asperities and an adhesive coating to facilitate transfer from anthers to pollinators, and from pollinators to stigmas. In this section, we will discuss adhesive functional morphology in nature, focusing on geckos, insects, tree frogs, and pollens. We will also introduce experimental studies of the influence of structure on dry and wet adhesion, including the complex interactions of structure with surface roughness.

1.3.1 Fibrillar Structure

It has been suggested that the adhesion of fibrillar structures on a rough surface can be stronger than their adhesion on a smooth surface [37], because fibrils with small

effective elastic modulus can adapt to rough surfaces. Fine-scale hairs, with tip size less than the opposing surface roughness, can adapt to surface features with low strains on the hairs, so the fibrils can have a large total contact area [65]. In addition, it is well-known that the detachment of multi fibrillar contacts requires more work than required to hold continuous contact [66], because the stored energy in a peeling fibril is not available for the detachment of the next fibril [37]. Therefore, many animals, from tiny mites to geckos and some mammals, take advantage of fibrillar adhesive pads to achieve strong adhesion on both smooth and rough surfaces.

In nature, the bio-adhesive mechanism of hairy surfaces could be classified as dry or wet adhesion. Using a scaling analysis from mites to geckos, Gorb discussed the dependence of contact density on body mass [28]. He suggested that heavier animals rely more on dry adhesion, such as geckos and spiders, and these animals tend to have compactly packed small fibrillar ends to create large peeling lines for strong adhesion [67]. However, recent studies claim that the total pad area of fibrillar systems is a main contributor to the strong dry adhesion, not the high density of the fibrillar ends [68, 69].

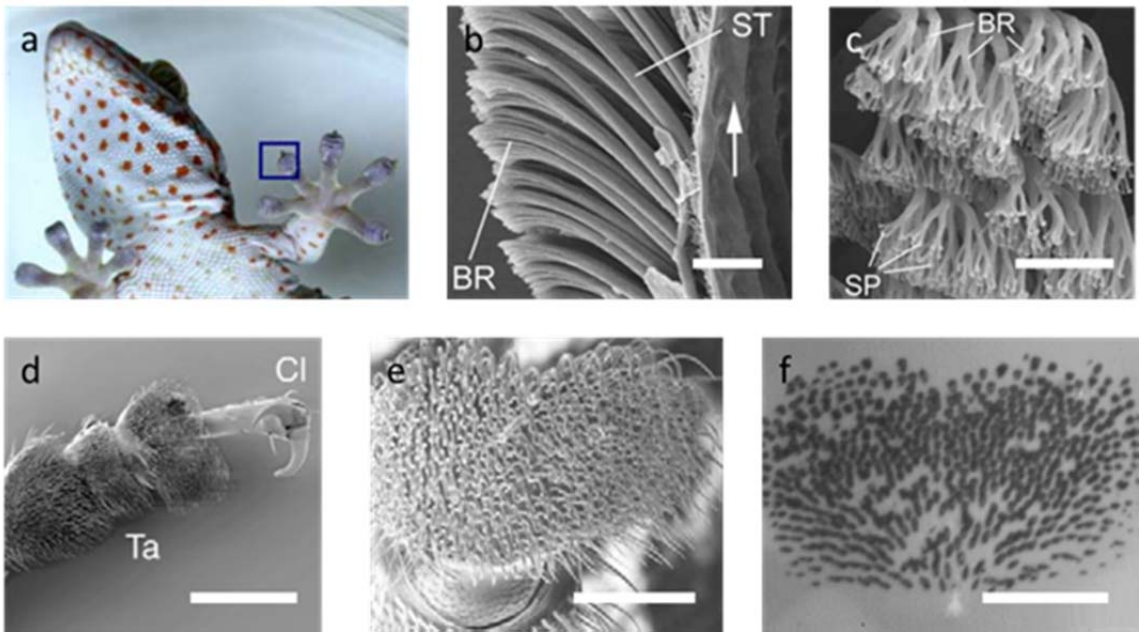

Figure 5 – The hierarchical structure of Gekko gecko adhesive pads (a-c). a Photograph of gecko toe; scanning electron microscopy (SEM) images of branch (BR), seta (ST), and spatula (SP) in the adhesive pad of geckos (b and c). (Reproduced with permission from [70]) The adhesive pad structure of a male dock beetle (G.Viridula) (d-f). SEM images of the adhesive pad (d and e) (Cl, claws; Ta, tarsal segments), and f visualized contact area of the beetle adhesive pad with glass via epi-illumination. (Reproduced with permission from [71]) Scale bars= 20 μm b, 5 μm c, 250 μm d, 100 μm e, and 100 μm f.

Autumn et al. claimed that molecular adhesion (vdW interaction) is the dominant adhesion mechanism of the gecko, since gecko adhesion was not affected by the hydrophobicity of the surface [13, 72]. Most gecko feet have hierarchical fibrillar structures consisting of lamellae, setae, branches, and spatulae [73] as shown in Figure 5 a-c. The second-level of the hierarchy, called the 'seta' (ST in Figure 5 b), is typically 30-130 µm in length and 5-10 µm in diameter, and the density of setae is about 14,000 setae /mm^2. In many species, these setae are split into multiple branches (BR in Figure 5 b and c) which are 20-30 µm long and 1-2 µm wide. Most setae terminate into 100-1000 spatulae (SP in Figure 5 c) with a diameter of 0.1- 0.2 µm [73]. In order to create strong

adhesion, the fibrillar structures should be mechanically soft to achieve a large number of contacting hairs with low strains. However, if the hairs are too soft, the hairs will be intricately entangled, and adhesion will be reduced significantly. The hierarchical structure is a solution to this problem. Hierarchical structures, such as lamellae and setae, provide the mechanical stability attributed to relatively high modulus and thick diameter structures, while lower level hierarchy, such as branches and spatulae, provide compliance and adaptability to roughness [28, 74]. Another significant feature of gecko adhesion is the asymmetrical structure (slope) of setae. When setae are attached on a surface, they are not vertical, but tilted with respect to the surface, and that is the reason why the pull-off force of single seta is strongly dependent on the pulling orientation [13]. It was observed that single seta adhesion was enhanced by more than an order of magnitude when the pulling angle was reduced from 90° to 30° [28, 75]. This result indicates that the asymmetrical structure of setae plays a significant role in achieving reversible adhesion, which can be easily switched between attachment and detachment for locomotion.

Insects with fibrillar adhesive pads, such as reduviid bugs, flies, and beetles, utilize liquid adhesive secretions to increase attachment force [49]. Unlike geckos, the insects don't have complex hierarchical structures, and the setae of most insects end in a single and relatively large spatula (the areas of terminal contact of beetles and flies are larger than 1 μm) as shown in Figure 5 d-f. To increase the contact area of the large spatulae on a rough surface, insects fill the gap between the spatula and surface with a liquid adhesive secretion. It was observed that the adhesion of insect pads was reduced significantly by organic solvent washing [76], and insufficient adhesive forces were

recorded when beetles were tested on a liquid absorbing nanoporous substrate [77]. Those studies show that the force magnitude of overall adhesion strongly relies on the capillary adhesion of the liquid bridges. In addition, the fibrillar structure allows multiple liquid bridges, which can produce a stronger total capillary force than a single liquid bridge with equal total liquid volume [78].

The contact geometries strongly affect the adhesive functions of the fibrillar adhesive pad [16, 79], and mushroom- and spatula-shaped elements are commonly observed contact geometries in nature. It was found that the contact element shapes, such as mushroom and spatula, are strongly related to the duration of adhesion [80]. Spatula-shaped elements require a shear force to generate adhesion, and these terminal elements are useful for short-term dynamic adhesion during fast locomotion because the contact can be easily detached by peeling within a few milliseconds. By contrast, the mushroom-shaped terminal elements are more suitable to create long-term adhesion. These elements do not require external applied shear forces, and a relatively higher pull-off force is required to rupture the contact.

1.3.2 Smooth Structure

Smooth adhesive pads are observed from diverse animals such as ants, bees, stick insects, grasshoppers, tree frogs, and arboreal possums [81]. As mentioned before, continuous surfaces cannot make a large number of contacts that adapt to the geometry of a rough surface like fibrillar adhesive systems. Thus, animals with smooth adhesive pads have developed strategies to overcome this limitation. One adaptation is the soft mechanical properties of the smooth adhesive pads, which have high deformation to

adapt a larger contact area on rough surfaces. For example, the reported effective elastic modulus of the adhesive pad of tree frogs is in the range of 4-25 kPa [82], and it is one of the softest biological structures. The smooth pads have an ultrastructure consisting of cuticular rods (insects) [17] or hexagonal epithelial cells (tree frogs) [14], and the fine structures of the pads allow close contact with low strain on the rough surfaces. All known smooth adhesive pads utilize thin liquid films, such as watery mucus of tree frogs, multi-phase adhesive secretion of insects, and sweat of arboreal possums, to fill the gap between the pads and substrates, and this liquid film helps the smooth pad to create a large contact area on rough surfaces.

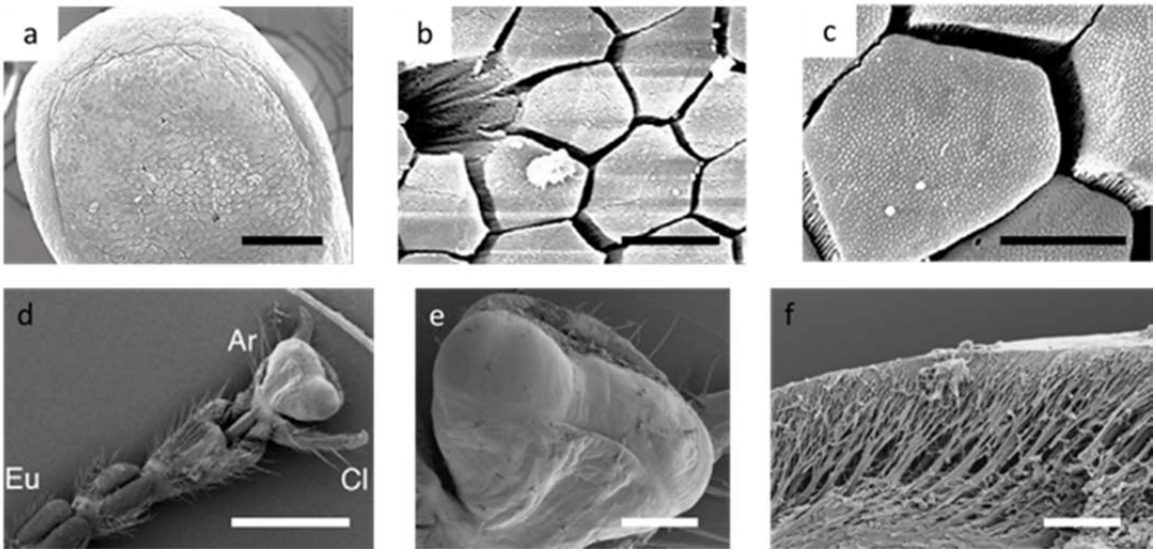

Figure 6 – Scanning electron microscopy (SEM) images of tree fog (Litoria caerulea) adhesive pad (a-c). a Toe pad, b hexagonal epithelial cell, and c densely packed nanopillars. (Reproduced with permission from [83]) SEM images of Indian stick insect (C. morosus) adhesive pad (d–f). d The front view of tarsal segments (Cl, claws; Eu, euplantulae; Ar, arolium), e the distal adhesive pad. (reproduced with permission from [71]) f Cross-section view of the distal adhesive pad within the smooth cuticle layer (branching fibrillars oriented almost perpendicular to the contact surface). (Reproduced with permission from [17]) Scale bars= 100 μm a, 10 μm b, 5 μm c, 1000 μm d, 200 μm e, and 20 μm f.

Tree frogs are well-known heavy body mass amphibians who utilize smooth adhesive pads. The details of the adhesive mechanism still remain elusive, but it was found that the physical properties and surface structures of the smooth adhesive pad have a critical role in attachment on vertical and overhanging surfaces [84]. Their adhesive pad consists of regular hexagonal epithelial cells (10-15 μm) (Figure 6 b) separated by watery mucus-filled channels (1 μm wide). Each cell consists of densely packed nanopillars (Figure 6 c), which are 300-400 nm in diameter with concave end shape [83]. The thin intervening watery mucus layer between the pad and surface forms an essential part of wet adhesion. The capillary force generated by a liquid bridge around the edge of the pad, and the viscous force generated over the whole contact area, strongly contribute to the adhesion of tree frogs [83]. The channel structure on the pad surface works to distribute fluid across the pad like a tire tread which allows for rapid drainage of liquid. The structured adhesive pad maintains an extremely thin liquid film for strong wet adhesion in air, and allows for the close contact of the pad with the surface under wet conditions [14]. Recently, the smooth pad morphology of torrent frogs, which are able to climb a vertical surface covered by high flow rate water, have been under investigation [85, 86].It is proposed that the straight channels between elongated cells can accelerate drainage rate of excess fluid underneath the pad.

Many insects with smooth adhesive pads also utilize wet adhesion of the adhesive secretion like the insects with fibillar pads. The smooth pads of the insects are a “pillow-like” soft structure (Figure 6 e) that consists of branching fibrils (Figure 6 f), oriented perpendicular to the surface, within the outer cuticle layer [17]. This internal fibrous structure helps to increase adaptability to surface roughness, and it can be used to

facilitate manipulation of the pad contact area via proximal pulling by the insects. It is not well understood how the presence of a continuous liquid film between a smooth pad and substrate can create strong static attachment ability on a vertical surface. It was suggested that the two-phase emulsion structure of the pad secretion could prevent insects from slipping [87]. The hydrophobic droplets dispersed in a watery continuous phase could provide viscous and non-Newtonian (shear thinning) properties of the secretion for maximizing static adhesion. Simple wet adhesion models, considering the contribution of the capillary and viscous forces, are often used to explain insect adhesion. However, for a more accurate representation, models should be expanded or even replaced to include the contribution of both the pad mechanical properties and non-Newtonian properties of the liquid adhesive. One recent study shows that the elastic deformation of the adhesive pad likely dominates the mechanical response when the adhesive secretions of animal are confined between elastic solids [88], and the authors utilize a fracture mechanics approach to estimate the adhesive mechanism of insects with the smooth adhesive pad.

1.3.3 Echinate Structure

Echinate structures normally have a limited contact area on hard and smooth surfaces since the adhesive force relies on the interaction between a few contacting tips of spines and a hard surface [89]. However, when the substrate is a soft, or a fibrillar/hairy surface, the spiny structures can create unexpectedly strong adhesion by penetrating the surface and/or creating mechanical interlocking [18]. Adhesion associated with penetration is much harder to explain with simple models of dry or wet adhesion, and fibrillar or smooth structures, so the details of the comprehensive mechanism still remain elusive.

Strong and tailored adhesion based on surface topography has a significant role in the active locomotion of animals, but it is also essential for the passive transport of plant pollens and seeds. Pollens are one example to show how the size and shape of nanoscale features can be utilized for adhering selectively to specific surfaces [19]. The surface of some flowering pollens consists of a structured exine, which interacts with pollinators and stigmas, and the exine is often covered by a viscous liquid coating, pollenkitt [90]. It is known that the adhesion of pollens to the stigma of the same species is much stronger than to another species, suggesting species-specific adhesion [91, 92]. For instance, the adhesive force magnitude of pollens from *Asteraceae* (sunflower) and *Oleaceae* (olive) families on stigma from *Asteraceae* (sunflower) was directly measured by AFM, and the results show that the echinate (spiny) structure of sunflower pollens strongly affects the adhesive mechanism of the pollen-stigma interaction on *Asteraceae* but not *Oleaceae* [18].

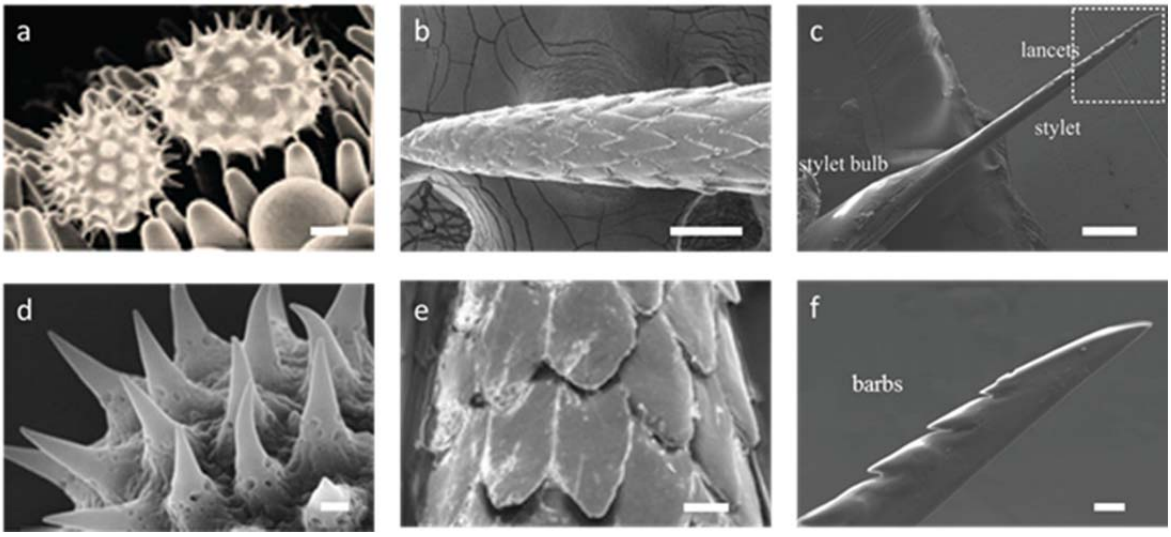

Figure 7 – Scanning electron microscopy (SEM) images of sunflower (Helianthus annuus) pollen on the stigma a, and spiny structures on the sunflower pollen d. (Reproduced from [18] with permission from Royal Society of Chemistry) SEM images of the tip of a North American porcupine quill b, and microstructures (barbs) on the tip e. (Reproduced with permission from [93]) SEM images of stinger of honeybee (Apis cerana cerana) c, and the tip of stinger and barbs near tip f. (Reproduced with permission from [94]) Scale bars= 5 μm a, 100 μm b, 200 μm c, 500 nm d, 20 μm e, and 10 μm f.

The sunflower pollen particle has a spherical core body (30 ± 4 μm in diameter) with 1.5-2 μm long spines, as shown in Figure 7 d. Structurally-derived load-dependent adhesion was attributed to the interlocking between the conical spines on the pollen surface and the stigma's receptive papillae (Figure 7 a). Previously, it was reported that the main contribution of the selective pollen-stigma interaction was dry adhesion (vdW interaction), since no significant difference of force magnitude was observed when the viscous liquid (pollenkitt) on the pollen surfaces was washed by organic solvents [19]. However, it is hard to generalize this observation because different species of pollens carry different amounts of pollenkitt. The contribution of the wet adhesive force attributed to pollenkitt seems to be comparable to the contribution of dry adhesion when pollens are coated with the sufficient amount (more than 30 wt% of innate pollens) of

pollenkitt [95]. Moreover, it was shown that adhesion between unpurified pollens (coated with pollenkitt) and stigma-mimetic polymer surfaces had more than doubled adhesive magnitude when compared to purified pollens. In addition the selective interaction between pollens and stigmas from the same botanical families was also observed when liquid pollenkitt wetted the surfaces [18].

In nature, many animals and plants utilize spiny features to protect themselves from natural predators, and these 'weapons' are optimized for easy penetration into and high adhesion on tissue surfaces. North American porcupines utilize the micro-structured barbs (Figure 7 b and e) on the tip of their specialized quills [93]. The conical shape of the tip is covered by a layer of backward facing micro-structured barbs, which are 100-120 μm in length and 35-45 μm in width (Figure 7 e). Compared with the barbless quills, the structured quills required 54% less loading force to penetrate into tissue, but required about 4 times larger pull-out force to be detached from the tissue surface. It suggests that the high-stress concentration near the barbs reduces the required force to deform the tissue around the tip of the quill, and the enhanced adhesion is attributed to the mechanical interlocking between barbs and tissue [93]. Micro-structured barbs (Figure 7 c and f) are also observed from the stingers of honeybees and paper wasps [96]. Different shapes of the barbs are observed from those two animals, and the shape and size of the barbs strongly affect the penetration, extraction, and the repeatable usage of their stingers. Similar mechanical interlocking adhesion on tissue surfaces is also observed in spiny-headed worms, such as *Pomphorhynchus laevis* [97]. This endoparasitic worm utilizes a barbed proboscis, which is swollen after embedding into the soft tissue of its host, to create strong adhesion.

1.4 Thesis Overview

In the previous sections, I showed the influence of surface morphology on both dry and wet adhesive mechanisms, and I introduced the examples of bio-adhesive systems, which utilize unique morphologies to control adhesion magnitude and create unique functionalities. In this research, I investigated the adhesion of pollens and pollen-shaped microparticles. Pollens have a structural diversity from a simple smooth surface to complex and spiny surface morphologies, making them outstanding experimental samples to study structural effects on particle adhesion. The adhesive force magnitude of microparticles was investigated by using colloidal probe microscopy. In chapter 2, I suggest a possible way for manipulating the adhesive force magnitude and range of pollen-shaped microparticles. In this chapter, I introduce how the short and long range force magnitude of the particles can be tuned simultaneously. In chapter 3, I discuss the influence of unique surface features of pollens on their wet adhesive mechanisms and correlation between the structural effect and the volume of liquid adhesive. In chapter 4, the discovery of a novel functionality from a pollen adhesive is introduced. In this chapter, I discuss the reason why the adhesive property of pollen adhesive can be preserved under dry and humid environments. Though this studies, I have learned: i) how to analyze quantitatively and model the attraction force of micro-particles with complex surface micro- and nano-scale morphology ii) the effects of both particle morphology and liquid physical properties on wet adhesion of micro-particles iii) how to stabilize the humidity-dependence of wet adhesives via control the structure of liquid phases.

CHAPTER 2. TUNABLE MULTIMODAL ADHESION OF $COFE_2O_4$ CERAMIC BIOGENIC REPLICAS ACHIEVED VIA GRAIN SIZE CONTROL

Note: The experiments and results described in Chapter 2 were planned, performed, and analyzed in collaboration with W. Brandon Goodwin, Georgia Institute of Technology, Atlanta, GA, USA.

2.1 Overview

Three-dimensional (3-D) multicomponent $CoFe_2O_4$ replicas of pollen microparticles have been synthesized with tunable multimodal (VDW and magnetic) adhesion properties through the use of surface sol–gel (SSG) processing. High-fidelity replication allowed the fine-tuning of particle adhesion via control of the crystallite size on the replica's surface features. The crystallite size controlled the contact area and number of contacts, allowing adjustment of the magnitude of short-range (~10 nm) van der Waals (VDW) attraction that controls adhesion. The crystallite size also allowed simultaneous fine-tuning of the magnetization of the $CoFe_2O_4$ particles in the pollen replicas, resulting in remarkable control over the magnetic component of particle attraction at long ranges (up to ~1 mm). The combined ability to control both short-range VDW and long-range magnetic forces by using crystallite size is a unique approach to designing biogenic, geometrically-complex 3-D microparticle replicas with tunable short- and long-range adhesion.

2.2 Introduction

The tuning of magnetic and van der Waals (VDW) attractive forces of particles through the use of chemistry and increasingly, particle shape and nanotopography, are valuable approaches to controlling particle adhesion in a wide range of developing and mature technologies, including targeted drug delivery, catalysis, water purification, chemical separations, sensing, anti-fouling coatings, semiconductor device processing, composite processing, printing inks, toners, paints, and the self-assembly of hierarchical structures. [98–108] The predominant models for understanding adhesion are based on smooth, spherical particles and many experimental studies utilize such model particles. [35, 38, 109–113] Thus, there is a strong interest in understanding how adhesion can be tuned by the use of non-spherical shaped particles with nanoscale roughness or topography. [103, 106, 114] However, the synthesis of micro-particles with regular, complex, and well-controlled three-dimensional (3D) nanoscale morphologies remains a difficult challenge. Thus, an understanding of the adhesive capabilities of these particles is at an immature stage.

Pollens are naturally-occurring microparticles that are available in a wide variety of complex 3D shapes and surface topographies, based on species. [115–125] They are an ideal source of non-spherical particles with reproducible, complex morphological features. Previous studies show that the adhesion between an echinate (spiny) pollen and a planar substrate is governed by the VDW interaction between the spine tip and the substrate. Thus, the spine tip end radius, which is significantly smaller than the particle overall radius, is the critical dimension that determines the magnitude of particle adhesion. [89] Native pollen particles can be used as templates and converted into 3D oxide replicas via use of a highly-conformal surface sol-gel (SSG) coating process. [126–

128] The process allows the capability of further tuning particle adhesion through magnetic or electrostatic interactions. Recently, adhesion measurements on SSG-produced pollen replicas comprised of ferromagnetic hematite (α-Fe_2O_3) [127] or ferrimagnetic magnetite (Fe_3O_4), [127] suggested that VDW adhesion with a planar surface may be based on the crystallite size within the spine tip, as opposed to the spine tip radius observed for native amorphous pollen. [95]

The purpose of this work is to explore the powerful capability that is enabled by utilizing the crystallite size of ceramic replicas to tailor the attraction forces of such 3-D biogenic microparticles. Native pollen particles were converted into a 3-D multicomponent oxide ($CoFe_2O_4$) via SSG coating and thermal annealing was used to control the average crystallite radius (R_C) of the ceramic replicas to investigate its influence on the fine-tuning of adhesion. The replicas were attached to AFM cantilevers, and short- and long-range attraction forces between the replicas and substrates (Ni, Cu, Au, and Ni-Nd) were evaluated with AFM.

The results indicate that the combination of specific nanoscale surface topography and magnetic oxide content of high-fidelity 3-D replicas provide for tuning the multimodal attraction to surfaces via both short-range VDW and short-to-long-range magnetic forces. Although coating or infiltration methods have been used previously to chemically modify or transform pollen [129–132] and other biological microparticles, [133–136] the conversion of sustainable biogenic particles into all-inorganic spinel ferrite 3-D replicas for the purpose of achieving controlled multimodal adhesion based on grain size has not been reported.

2.3 Experimental

2.3.1 Replica Fabrication and Analysis

Fe-O-bearing and Co-O-bearing coatings were applied to cleaned, acid washed pollen grains via a computer-automated (in a N_2 atmosphere glove box), layer-by-layer (LbL) SSG deposition process by: [137, 138] i) immersing pollen grains for 10 min, with stirring, in a solution of either 0.0125 M Fe(III) isopropoxide (Alfa Aesar, Ward Hill, MA USA) in anhydrous 2-propanol (>99.8% purity, Acros Organics, Geel, Belgium) for the Fe-O-bearing layers or 0.0125 M Co(II) isopropoxide (Alfa Aesar, Ward Hill, MA USA) in anhydrous 2-propanol (>99.8% purity, Acros Organics, Geel, Belgium) for the Co-O-bearing layers, to allow for the chemisorption of a Fe-O-bearing or Co-O-bearing layer, ii) rinsing three times with anhydrous 2-propanol followed by vacuum filtration, iii) immersion in de-ionized water (DIW) with stirring, for 5 min, to allow for hydrolysis of the chemisorbed alkoxide layer, iv) rinsing three times with anhydrous 2-propanol followed by vacuum filtration, and v) and drying by vacuum aspiration for 5 min. This process (alkoxide exposure, alcohol rinsing, water exposure, alcohol rinsing, drying) was repeated 50 times (for a total of 51 cycles) to build up a continuous and conformal coating. The pollen particles were coated with alternating Fe-O and Co-O layers, in a Fe-O:Co-O ratio of 2:1, so as to achieve the desired stoichiometry for the $CoFe_2O_4$ spinel. The SSG-coated pollen particles were prepared for pyrolysis in the following manner: i) SSG-coated pollen particles were suspended in IPA and then dispersed onto nickel foil (25.4 μm thick, McMaster-Carr, Cleveland, OH, USA) using a pipette, ii) SSG-coated pollen particles were suspended in IPA and then dispersed onto silicon wafers (Wafernet, Inc., San Jose, CA, USA) using a pipette, and iii) SSG-coated pollen particles were also

placed in a MgO crucible. Samples were fired in air using a tube furnace (Lindberg / Blue M, NC, USA,) with a ramp rate of 3°C min^{-1} to a peak temperature 600°C, 700°C, 800°C, or 900°C and held at this temperature for 2 h to allow for organic pyrolysis and oxide crystallization. The pyrolysis process was also studied using thermogravimetric analysis (TGA) (Netzsch STA 449C, Wolverhampton, UK). The TGA measurements were performed with the as received pollen and as coated pollen grains at a heating rate of 5 ºC min^{-1} up to 600 ºC in a flowing (flow rate of 50 cm^3min^{-1}) synthetic air gas mixture. The phase identification for the fired pollen replicas were evaluated at room temperature using X-ray diffraction (XRD) analyses. XRD analyses were conducted on a diffractometer (X'Pert Pro Alpha-1, PANalytical B.V., ALMELO, Netherlands) with $Cu_{K\alpha 1}$(1.5405980 Å) radiation emanating from a 1.8 kW ceramic X-ray tube with a copper anode (45 kV, 40 mA) through an incident beam Johansson monochromator (PANalytical) and detected by an X'Celerator detector. The incident beam optics were outfitted with 0.04 rad soller slits, a 2° fixed anti-scatter slit, a programmable divergence slit set to 5.5 mm irradiated length, and a 10 mm mask. The diffracted beam optics were outfitted with a 5.5 mm anti-scatter slit and 0.04 rad soller slits placed before the X'Celerator detector. Each pattern was produced with a summation of 40 identical 30 minute scans conducted with Bragg-Brentano geometry and a step size of 0.017° 2θ ranging from 20° to 90° 2θ. The minimum setting on the Pulse Height Discrimination (PHD) for the X'Celerator detector was increased to from 36 to 42 to help discriminate between the diffracted signals and fluorescence photons from the Fe and Co atoms. [139] Diffraction specimens were dispersed on quartz cut (6° from (0001)) low background specimen support (GEM dugout, PA, USA) via pipetting an aliquot of IPA/powder slurry

onto the specimen support and allowing the IPA to evaporate. Phase identification and average crystallite radius (R_C) were determined using the HighScore Plus software (PANalytical B.V, Almelo, The Netherlands) using a profile fit function. A Pseudo-Voigt profile fit function was used in conjunction with a Williamson Hall plot to determine the average grain size of the pollen replicas. Elemental analysis was obtained by ICP-MS (Inductively coupled plasma mass spectroscopy: PerkinElmer ICP-MS model-ELAN 9000) and with the use of an energy dispersive X-ray spectrometer (EDS) (INCA Model 7426, Oxford Instruments, Bucks, UK) equipped to a scanning electron microscope (1530 FEG SEM, LEO / Carl Zeiss SMT, Ltd., Thorn-wood, NY USA). ICP-MS and EDS analyses were both conducted on three different samples in order to obtain the Fe/Co ratio.

2.3.2 Metal Substrate Preparation

To study the short-range (VDW) and long range (magnetic) adhesion four types of substrates were utilize: copper (Cu), gold (Au), nickel (Ni), and a nickel-coated neodymium (Ni-Nd) alloy. The three different metal substrates (Ni, Au and Cu) were chosen to analyze intermolecular force between the metal surface and the replica. To minimize the effect of the surface roughness, 100 nm of Copper and Gold were deposited on the silicon (Silicon, Inc., Boise, ID) by CHA Ex e-beam evaporator (CHA Industries, Fremont, CA, USA) at a rate of 2Å/sec and a background pressure of 10-6 torr. Nickel substrates (0.150 mm thickness, grade 200, 99.5% purity, Shop-aid, Inc., Woburn, MA) in the area of 38.5 mm2 was prepared by electro polishing under 1.3 A current for 120 sec with 8.9 mol L-1 of sulfuric acid as electrolyte and platinum rod as cathode. Both metal substrates were washed by acetone (99.5% purity, BDH Chemicals Ltd., Radnor,

PA USA) in the ultrasonic cleaner (FS20, Fisher Scientific, Pittsburgh, PA, USA) for 10 min at room temperature before the experiment. The Ni-Nd substrate consisted of an axially-poled, neodymium-iron-boron alloy permanent magnet disk (ND022N-35, 5 mm diameter, 1.5 mm thick, Master Magnetics, Inc., Castle Rock, CO USA) onto which was attached the polished nickel foil. The surface roughness of each type of substrate was evaluated with a scanning probe microscope (Dimension 3100 SPM equipped with a Nanoscope V Controller, Veeco Instruments, Inc., Plainview, NY USA) operated in tapping mode at 200-400 Hz using a pyramidal tip silicon cantilever (Applied Nano Structures, Inc., Santa Clara, CA USA). For each particular substrate, 3 randomly-located scans (10 μm x 10 μm) were conducted, with each scan area split into 10 sectors, and 4 sectors (1μm x 1μm) were randomly selected. The average roughness value for a given substrate was obtained from analysis of these 12 sectors.

2.3.3 Adhesion Measurement

To perform the adhesion measurements, single particle (a native sunflower pollen particle or oxide replica particle) were attached to an atomic force microscope (AFM) cantilever. A small amount of epoxy resin (Epoxy Marine, Loctite, Westlake, OH USA) was used to attach a given particle to a tipless silicon AFM cantilever (FORT-TL, Applied NanoStructures, Inc.). For each type of pollen-shaped particle (cleaned sunflower pollen and $CoFe_2O_4$ replica) and firing condition used (600°C, 700°C, 800°C, and 900°C), 3 single-particle-bearing cantilever probes were prepared by using a procedure described previously [127] (for a total of 12 particle/cantilever probes). The spring constants, as determined with the scanning probe microscope, of the sunflower-pollen-bearing, 600°C, 700°C, 800°C, and 900°C $CoFe_2O_4$-replica-bearing cantilever

probes fell in the ranges of 0.867-0.973 N/m, 0.899-1.145 N/m, 1.040-1.208 N/m, and 1.020-1.287 N/m, respectively. The adhesion force between an individual sunflower pollen particle, or oxide replica particle, and a particular substrate was evaluated with the scanning probe microscope operated in contact mode. For each particular particle/cantilever probe and particular substrate, 10 separate force-distance scans were randomly obtained, and the depth of adhesion wells upon retraction were aver-aged. The load force applied during the contact adhesion measurements was 2.5 nN. The ambient relative humidity in the laboratory during the adhesion measurements ranged from 30 to 35%. Magnetic properties of $CoFe_2O_4$ spinel ferrite sunflower replicas were studied using a superconducting quantum interference device (SQUID) magnetometer (Quantum Design MPMS-5S, San Diego, CA USA) with a magnetic field up to 5 T. Measurements were conducted at 300K.

2.4 Result and Discussion

2.4.1 Controlled Crystal Size by Firing Temperature

The pollen particles were coated with alternating Fe-O and Co-O bearing layers, in a Fe-O:Co-O ratio of 2:1, so as to achieve the desired stoichiometry for the $CoFe_2O_4$ spinel. Sunflower pollen particles were exposed to 51 SSG deposition cycles (17 Co-O cycles and 34 Fe-O cycles) and fired at 600 ^oC, 700 ^oC, 800 ^oC or 900 ^oC. Secondary Electron (SE) images of the sunflower pollen particle after exposure to 51 SSG deposition cycles (17 Co-O cycles and 34 Fe-O cycles) and after firing at a peak temperature 700 ^oC for 2 h are shown in Figure 8 a and b. White arrows mark individual features that were preserved from the as-coated samples by the pyrolyzed samples. The 3-

D morphology and sharp echini of the sunflower pollen were retained by the $CoFe_2O_4$ ferrite replicas, even after firing to a peak temperature of 900 ^oC in air for 2 h. TG analyses confirmed that these replicas were freestanding oxides with complete pyrolysis of the sporopollenin achieved within 100 min at 600 ^oC.

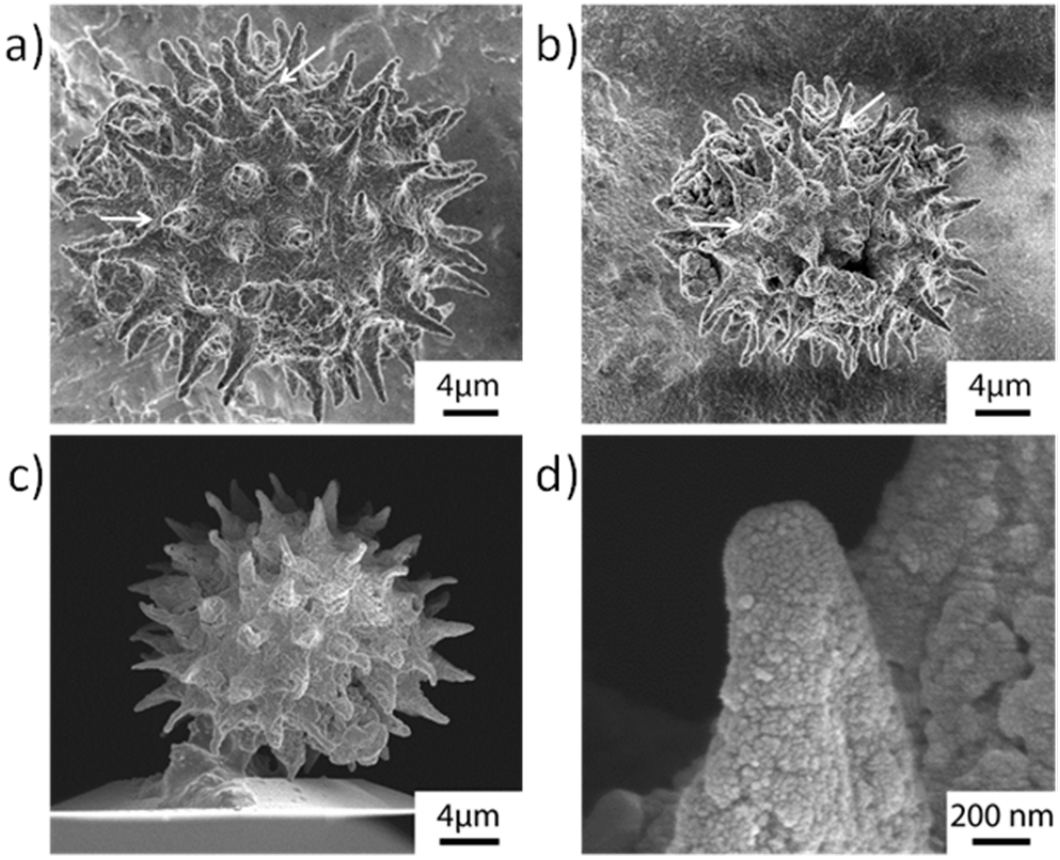

Figure 8 – SE images of a) Co-Fe-O-coated sunflower pollen particle exposed to 51 cycles of the surface sol-gel deposition process; and (b) the same coated particle after pyrolysis for 2 h in air at a peak temperature of 700 ºC. Arrows point to select features that were preserved after thermal treatment. c) SE image of a single-particle-bearing cantilever probe with CoFe2O4 sunflower pollen replica fired in air for 2 h at a peak temperature of 700 ºC. d) SE image of spike tips of CoFe2O4 sunflower pollen replica on probe of image (c). Reproduced with permission from [140]

Inductively-coupled plasma mass spectrometry (ICP-MS) analysis (ICP-MS, Wellesley, MA) of the $CoFe_2O_4$ pollen replicas fired at a peak temperature of 600 ^oC 2 h,

was conducted by digesting the samples with aqua regia and heating in a sealed Teflon container in a microwave operated at 400 W for 25 min. The ICP-MS analyses were repeated three times and yielded Fe/Co atomic ratios of 1.96, 1.91, and 1.86. EDS analyses (Figure 9 a) of the $CoFe_2O_4$ pollen replicas yielded an average Fe/Co ratio of 1.98 ± 0.05. The phosphorus and sulfur peak present originated due to residual ash from the native pollen grains. The average measured values give a formula composition of $Co_{1.03}Fe_{1.97}O_4$ and of $Co_{1.01}Fe_{1.99}O_4$ for ICP-MS and EDS results, respectively.

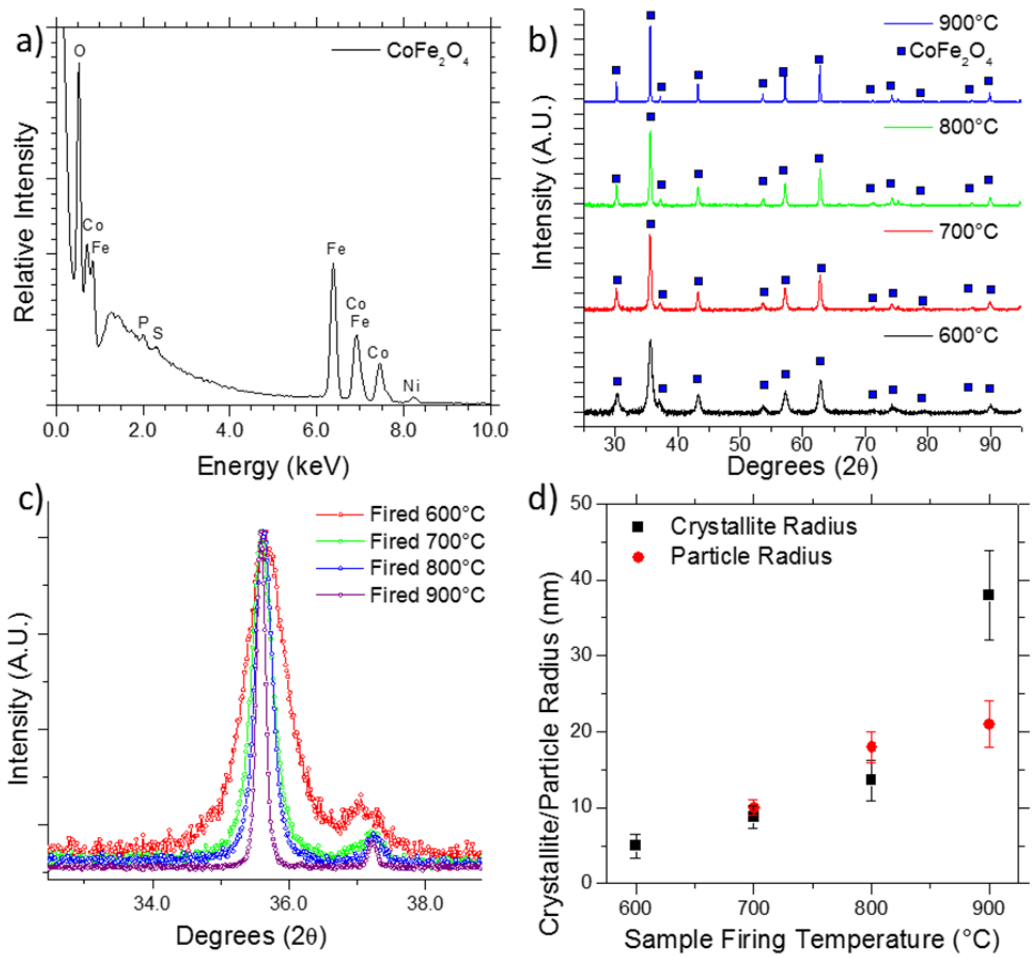

Figure 9 – a) Representative EDS spectrum of CoFe2O4 ferrite sunflower replicas after firing in air to a peak temperature of 600 ºC for 2 h, b) XRD pattern obtained CoFe2O4 pollen replicas, c) (311) diffraction peak of CoFe2O4 replicas showing a decrease in the FWHM of this peak as firing temperature (2 h) increased, d) The crystallite and nanoparticle radii as determined from XRD (black) and SEM (red) analyses for CoFe2O4 pollen replicas fired in air for 2 h at a peak temperature in the range of 600-900 ºC. Reproduced with permission from [140]

XRD analyses were then used to evaluate the phase content of the $CoFe_2O_4$ ferrite replicas, and to determine the grain size resulting from each firing temperature. Figure 9 b shows the XRD patterns obtained from $CoFe_2O_4$ pollen replicas for each firing temperature, which indicate that each sample was comprised of single phase $CoFe_2O_4$. The peak width became narrower at higher firing temperatures, consistent with an

increase in average crystal size with firing temperature. Comparison of the experimental (311) diffraction peaks for the different peak firing temperatures can be seen in Figure 9 c. Full pattern profile fitting was conducted on these XRD patterns for crystallite size analyses. An increase in R_C was observed with increasing peak firing temperature (Figure 9 d).

SEM images of individual pollen grains attached to the ends of AFM cantilever tips are shown in (Figure 8 c). Higher magnification images were obtained of the individual spine tips (Figure 8 d) to enable measurement of the sizes of oxide nanoparticles present on the spine surfaces. Twenty particles were measured on 3 spine replica tips for each replica sample. For the 600 ^{o}C samples, individual nanoparticles were too fine to allow for unambiguous nanoparticle size determination. For T > 600 °C, Figure 9 d provides the average nanoparticle radius (R_P) measured by SEM analyses, in addition to XRD-determined R_C values mentioned above. There are differences in magnitude between the XRD and SEM results for crystallite size, possibly due to grain size differences on the spine tips vs. within the $CoFe_2O_4$ wall of replicas or due to the partial exposure of the grains on the surface. However, both analytical methods clearly indicate an increase in crystallite size with increasing peak firing temperature.

2.4.2 Influence of Crystal Size on Short Range Adhesion

In order to determine the influence of the average crystal/particle size of $CoFe_2O_4$ pollen replicas on short-range van der Waals (VDW) attraction, contact mode AFM measurements were conducted to measure the force of adhesion of $CoFe_2O_4$ sunflower replica particles (attached to AFM cantilevers) to three different planar metallic

substrates: Ni, Au, and Cu films on a silicon wafer. The measured roughness of all substrates fell within the range of 0.9-1.1 nm. Plots of the measured average VDW adhesion force on each substrate, as a function of surface nanoparticle size (as measured from SEM analyses of the 700-900 °C samples) and crystallite size (as measured from XRD for the 600-900°C samples) for the $CoFe_2O_4$ replicas are presented in Figures 10 a and b, respectively.

The plots in Figures 10 a and b. reveal a similar non-monotonic trend for all three metallic substrates; that is, the average adhesion force initially decreased with increasing crystal and nanoparticle size, reached a minimum value at crystal and nanoparticle radii of 14 nm and 18 nm, respectively (peak firing temperature of 800°C), and then increased with further increases in crystal and particle radii. Previous work has indicated that crystallite size played a role in the short range VDW adhesion of sunflower ceramic replicas (Fe_2O_3 and Fe_3O_4).[127] The reported adhesion values were consistent with the contact of one or two nanocrystals (average crystallite radii, 17-18 nm) located at the spine tips with the substrates.

The nonlinear behavior in the present case has been further evaluated with the use of the following simple Hamaker model for the adhesion force between a sphere and a plate:[20]

$$F_{vdw} = -\frac{A_{132}}{24R}\left(\frac{2}{x} - \frac{1}{x^2} - \frac{2}{x+1} - \frac{1}{(x+1)^2}\right), \quad (17)$$

where A_{132} is the non-retarded Hamaker constant of material 1 (metal substrate) interacting with medium 2 ($CoFe_2O_4$) across a medium 3 (air); R is the contact radius of

the sphere (or spherical nanoparticle or crystal); $x = D/2R$; and D is the separation distance between the sphere and the plate. An approximate value of A_{132} (≈ 3.3 X 10^{-19} J) for $CoFe_2O_4$ sunflower pollen replicas on the metal substrates was calculated by using the following equation [33]

$$A_{132} \approx \left(\sqrt{A_{11}} - \sqrt{A_{33}}\right)\left(\sqrt{A_{22}} - \sqrt{A_{33}}\right), \quad (18)$$

with A_{11} (≈ 4 X 10^{-19} J) [33] and A_{22} (≈ 4 X 10^{-19} J) [141] values obtained from the literature, and $A_{33} = 0$. The value of F_{vdw} predicted by Equation (17) should be linearly proportional to R for cases when D is much smaller than $2R$ (i.e., for these cases, the second term on the right side of this equation, $A_{132}R/6D^2$, becomes dominant). For contact radii in the range of values of the measured crystal/particle radii shown in Figures 10 a and b, the predicted values of the VDW adhesion force associated with such a single crystal/particle contact (by $A_{132}R/6D^2$) are linearly proportional to the radius of the crystal/particle. The monotonic dependence of adhesion on crystal/nanoparticle radius predicted by the single contact radius model is not consistent with the nonmonotonic dependence observed experimentally (Figures 10 a and b).

Equation (17) was then used to extract values of the effective contact radius (R_H) for each sample from measured adhesion force values, by solving for the R value (called R_H) that resulted in a force equal to the measured value. The ratio of R_H to the measured surface nanoparticle radius (R_P) or crystal radius (R_C) is plotted versus R_P or R_C in Figures 10 c and 3d. An R_H/R_P or R_H/R_C ratio of unity would be consistent with adhesion via contact of a single nanoparticle or crystal according to Equation (17). As seen in Figures 10 c and d, this condition is roughly met at the values of R_P = 18 nm and R_C = 14

nm, i.e., the replicas fired at 800 °C peak temperature. In this case the measured adhesion force values of 35-38 nN were close to the values of 27 nN (with R_C = 14 nm) or 36 nN (with R_P = 18nm) predicted by the single contact Hamaker model, Equation (17). However, the extracted values of R_H were always noticeably different from the measured values of R_P and R_C for the samples fired at 600 °C, 700 °C, and 800 °C, indicating that a single contact point cannot explain the adhesion of replicas fired at those temperatures.

As illustrated in Figure 10 e for a curved surface containing fine particles (representing the crystalline grains, assumed simplistically to be spherical in shape with uniform radii of R_S), the number of particles located within the VDW interaction region with the substrate will depend on the particle size. At a sufficiently large particle size, a single contacting particle will dominate the short-range van der Waals attraction, indicated in Figure 10 e, left side. As shown in the estimated values by Hamaker model ($A_{132}R/6D^2$), such a single-contact model leads to a monotonic increase in the adhesion force with an increase in the particle radius. However, for smaller R_S values, the adhesion force will be dependent on multiple particles interacting within the short VDW range, ~10 nm. In this "multiparticle" attraction case, an increase in VDW force may be observed with a decrease in particle size, due to the corresponding increase in the number of particles interacting with the surface, illustrated in Figure 10 e, right side The switching between these two competing effects of particle size on the total VDW adhesion is expected to occur at a particle radius within the VDW interaction range, e.g., ~10 nm. This is consistent with the experimentally-observed minimum point in Figure 10 a and b, and can explain the nonmonotonic relationship between adhesion and the particle or crystallite size.

To provide further support for this hypothesis, a simple computer simulation model was utilized. The number of crystallites in the VDW interaction zone (~ \10 nm) of the substrate surface and their positions relative to the substrate were determined by modeling the grain structure of the replica spine tip as perfectly packed small spheres on a large hemisphere. The small spheres represent the crystallites and the large hemisphere represents the end of the replica spike (average radius, 196 ± 17 nm), as indicated in Figure 11 a for spheres of size R_S = 8 and 16 nm.

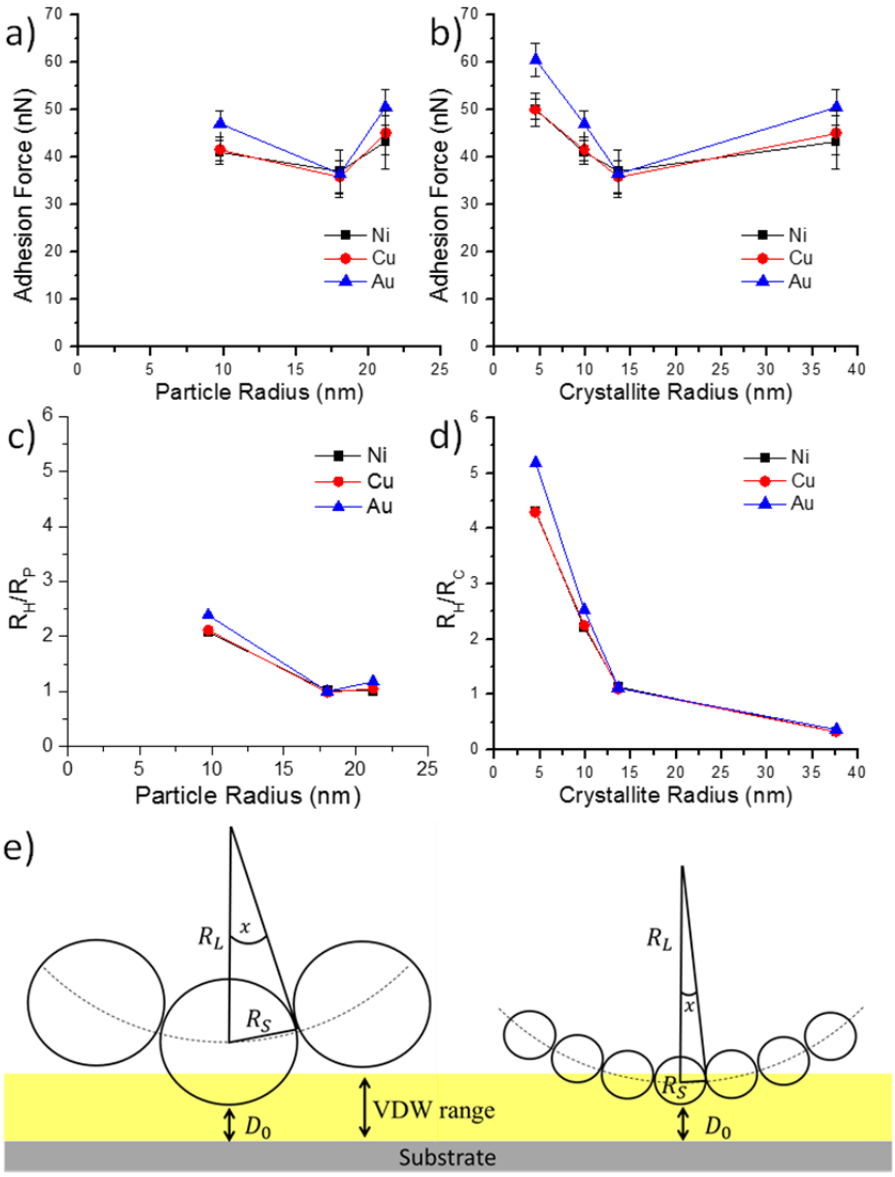

Figure 10 – AFM measurements of the short-range VDW-based adhesion force for CoFe2O4 sunflower replicas of various: a) surface nanoparticle radii (from SEM analyses) and b) crystallite radii (from XRD analyses) on metallic substrates. The error bars indicate 95% confidence intervals. (c) The ratio of the effective contact radius derived from the Hamaker model to nanoparticle radius measured by SEM, (RH/RP), versus RP. (c) The ratio of the effective contact radius derived from the Hamaker model to crystallite radius measured by XRD, (RH/RC), versus RC. e) 2-D diagram illustrating the multiparticle model of VDW adhesion consisting of an assembly of symmetrical small spheres of radius (RS) arranged on a larger hemisphere of radius RL) Reproduced with permission from [140]

Figure 11 b presents the number of spheres in the range of 10 nm from the substrate over a range of representative small sphere (crystallize) sizes, R_S. It is clear that the number of adhesive contacts is large when R_S is small, and drops to a limiting value as R_S increases above ~10nm. The adhesion of each small sphere in the VDW interaction zone with the substrate was calculated by Equation (17) by taking the separation distances from the substrate as $D = H + 0.165$ nm (cutoff distance) [33] and by using the previously estimated Hamaker constant of $A_{132} \approx 3.3 \text{ X } 10^{-19}$ J. The total adhesion between the large hemisphere (spine tip composed of many small crystallites) and the substrate was calculated by summation of the adhesion forces of each small sphere (crystallite) with the substrate, indicated in Figure 11 c. The suitability of the assumptions made for the model should be considered. First, it is assumed that only one spike of the replica contacts to the metal substrate, and this assumption was proved reasonable in a previous study of magnetite pollen replica adhesion. [127] The crystallites are assumed to be uniform spheres for the simplification of the adhesion estimation. The size of crystallites on the spine tips varies by less than 14 % (Figure 9 d) and the structures of crystallites are roughly spherical according to the SEM image of the spine tip (Figure 8 d). In summing the individual adhesion of each nanoparticle with the flat substrate, we are assuming that any permanent or induced dipoles in the crystals or surface do not interact with one another. Finally, the individual nanoparticles are assumed to be tightly packed on the spine tip surface in our model. Despite these assumptions, the intention of the model is to reproduce the first order dependence of the total adhesion on the nanoparticle size. The model does show that the qualitative non-monotonic relationship

between crystal size and adhesion can be attributed to the counteracting effects of crystal size on the VDW force and the number of crystals in the VDW interaction zone.

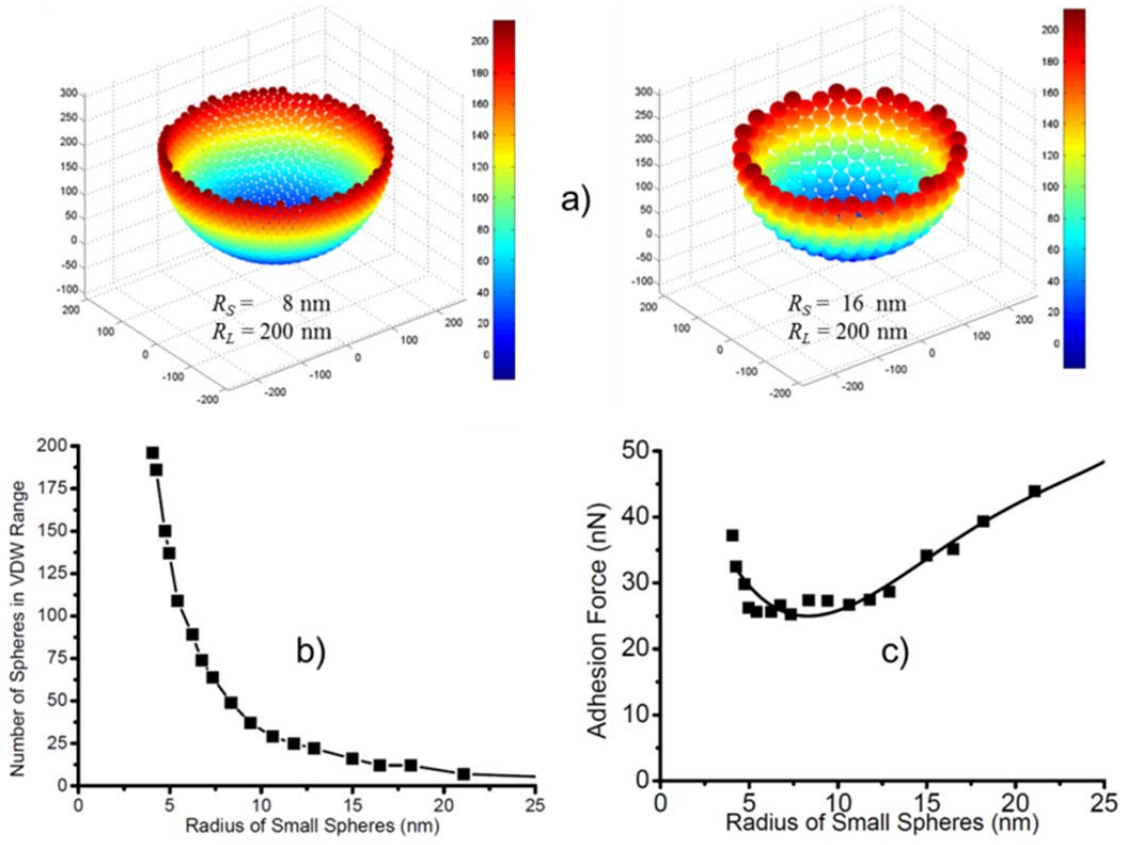

Figure 11 – a) 3-D schematic of the model of nanoparticles on a spine tip, consisting of perfectly packed small spheres on a large hemisphere. (R_s- radius of small spheres, R_L- radius of large hemisphere). Calculated relationship between b) the number of small spheres in VDW range (~ 10nm) and radius of small spheres, (R_s) and c) total adhesion force and radius of small spheres (R_s) by the model simulation.

2.4.3 Influence of Crystal Size on Long Range Magnetic Force

The magnetic hysteresis behavior of the $CoFe_2O_4$ replicas with varying grain size was examined with a SQUID magnetometer at room temperature (300 K) via active temperature control and at 5 K. As shown in Figure 12 a and b, distinct magnetic hysteresis loops, consistent with ferrimagnetic materials, were obtained for all samples at

5 K and 300 K, respectively. The values of saturation magnetization (M_s) of the fired replicas at 5 K were 58 Am^2/Kg, 67 Am^2/Kg, 78 Am^2/Kg, and 85 Am^2/Kg and at 300 K were 53 Am^2/Kg, 60 Am^2/Kg, 72 Am^2/Kg, and 80 Am^2/Kg for samples fired at a peak temperature of 600°C, 700°C, 800°C, and 900°C, respectively. The values of remanent magnetization (M_r), (the magnetization values of the fired replicas retained after the applied field was removed), at 5 K were 38 Am^2/Kg, 46 Am^2/Kg, 52 Am^2/Kg, and 54 Am^2/Kg and at 300 K measurements were 9 EMU/g, 20 Am^2/Kg, 27 Am^2/Kg, and 30 Am^2/Kg for samples fired at peak temperature of 600°C, 700°C, 800°C, or 900°C, respectively. The values of coercive field (H_c), (the minimum magnetic field required to switch the magnetic moment of the $CoFe_2O_4$ replicas to the direction of the applied field), at 5 K were 1.35 T, 1.22 T, 1.08 T, and 0.45 T, and at 300 K were 0.0490 T, 0.0885 T, 0.0940 T, and 0.0619 T, for samples fired at 600°C, 700°C, 800°C, or 900°C, respectively. For both room temperature and 5 K measurements, M_r and M_s values increased with increased peak firing temperature. The increase in saturation magnetization values for $CoFe_2O_4$, as a function of crystallite size (firing temperature) has been reported previously. [142, 143] The referenced magnetic saturation values were obtained from nanoparticles synthesized at room temperature by either a solution precipitation reaction or prepared by a redox process.

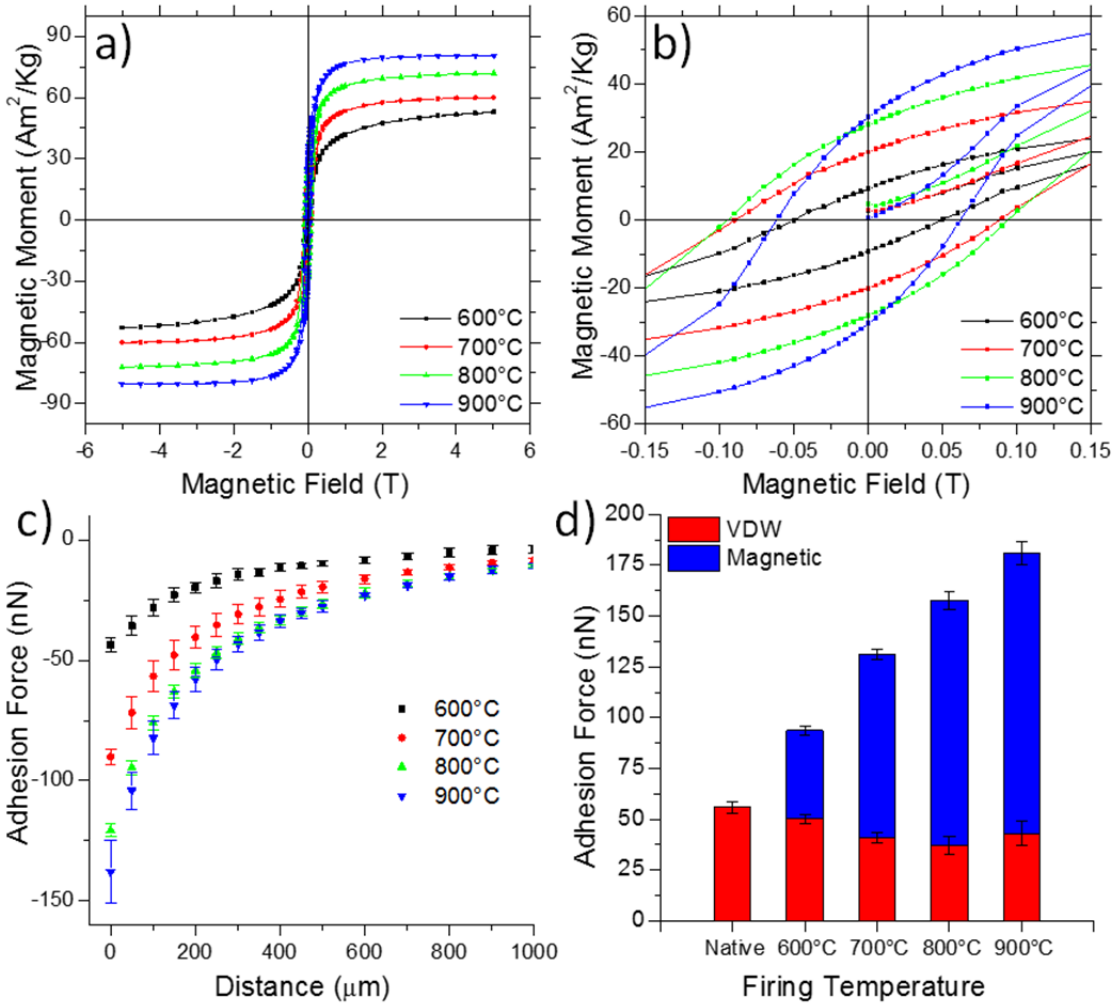

Figure 12 – Superconducting Quantum Interference Device (SQUID) analyses conducted at 300 K for CoFe2O4 sunflower replicas synthesized at various peak reaction temperatures. a) Entire plots and b) magnified sections. c) AFM measurement of the magnetic adhesion force vs. distance for CoFe2O4 sunflower replica probe on a Ni-Nd substrate (dots). The force was obtained at ~300 μm from the edge of the disk-shaped Ni-Nd substrate. d) Combined short range (VDW) and short to long range (magnetic) adhesion for native sunflower pollen and sunflower pollen replicas. Reproduced with permission from [140]

To investigate the effect of crystallite size on the longer-range magnetic force, the attraction forces between $CoFe_2O_4$ sunflower replicas with various crystallite sizes and a permanent magnet Ni-Nd substrate were measured by AFM. The force measurements were conducted at a lateral distance ~300 μm from the outer edge of the disk-shaped Ni-

Nd magnet and measured at height intervals of 50 μm from the surface. The measured attraction forces for the 600°C, 700°C, 800°C, and 900°C samples are shown in Figure 12 c. This figure reveals a monotonic increase in the measured magnetic force of attraction with peak firing temperature, which is consistent with an increase in the RC or RP with peak firing temperature (Figure 9 d). Such an increase in magnetic force with average crystal size is consistent with the measured increase in the values of magnetization (at a given applied magnetic field) with crystal size of the CoFe2O4 replicas (Figures 12 a and b). Control over the average crystal/nanoparticle size of the nanocrystalline CoFe2O4 pollen replicas, through adjustment of the peak firing temperature, provided a means for controlling both the short-range (VDW) and long-range (magnetic) forces of attraction. To reveal the extent to which the total force of attraction (short-range + long-range) of the CoFe2O4 pollen replicas could be tailored relative to the native (cleaned) sunflower pollen, the total attraction of such pollen replicas and native pollen to the magnetic substrate is shown in Figure 12 d. The total force of adhesion of the CoFe2O4 replicas to the Ni-Nd substrate could be increased by a factor of ~3 (for a peak firing temperature of 900oC) relative to the native pollen grains.

2.5 Conclusion

This work demonstrates that a highly-conformal SSG-coating process can be used, along with controlled thermal treatments, to convert sunflower pollen particles into nanocrystalline ferrimagnetic ($CoFe_2O_4$) replicas exhibiting controlled multimodal adhesion via short-range (~10 nm) VDW-based attraction and short-to-long-range (up to ~1 mm) magnetic attraction. An increase in crystallite size, from higher temperature thermal treatments, resulted in increases in the values of both remanent and saturation

magnetization. The improved magnetic properties led to a detectable increase in long-range attraction to magnetic substrate. A reproducible nonmonotonic relationship was also observed between average $CoFe_2O_4$ crystal size and short-range VDW adhesion. The crystallite size correlation with VDW adhesion correlation was attributed to the counteracting effects of crystal size on the VDW force of an individual crystal and on the number of crystals within the VDW interaction zone. This tendency was explained by a multi-sphere Hamaker model. The long-range magnetic force was also tailored by adjusting the average crystal size, because an increase in grain size resulted in an increase in the magnetization of the replicas. By controlling the crystallite size of the ceramic pollen replicas, both the long-range (magnetic) and short-range (VDW) adhesion force could be tuned.

Acknowledgement: I am grateful to Dr. Ken Sandhage and Brandon Goodwin for their contributions to this work. They performed the preparation and characterization of magnetite pollen replicas and supplied the data in Figures 8 (a and b), 9, and 10 (a and b).

CHAPTER 3. INFLUENCE OF SURFACE MORPHOLOGY ON STATIC AND VISCOUS ADHESIVE FORCE OF CAPILLARY LIQUID BRIDGES

3.1 Overview

Most of current knowledge of the wet adhesive mechanism with a viscous liquid bridge is still under the limit of simple geometries without considering organized fine-scale surface features. We investigated and discussed how the fine-scale morphology on a surface could affect the wet adhesive mechanism of the viscous liquid bridge at various separation rates and film thicknesses. To investigate the surface morphology effect on the wet adhesive mechanism with a viscous liquid bridge, the wet adhesive mechanism of pollen grains on pollenkitt liquid bridges was studied qualitatively and quantitatively. Pollens are well-known microparticles with organized fine-scale surface morphology, and pollenkitt is the common adhesive material coating the surface of pollen pollinated by animals. Two different pollens (ragweed and sunflower) were used to examine the effect of surface morphology on the wet adhesion mechanism.

3.2 Introduction

For two surfaces in contact to separate, the adhesion between them must be overcome. It is well known that adhesion of solid surfaces can be enhanced or weakened by the formation of a liquid bridge, depending on the physical properties and volume of the liquid. [144][145] The two main contributors to wet adhesion resulting from liquid bridges are static capillary forces and hydrodynamic viscous forces. [144][146] Under

static conditions, wet adhesion is controlled by capillary forces, but the contribution of viscous forces becomes important as viscosity and shear rate increase. [52] The adhesion of liquid bridges is important for wet adhesion in Nature, including pollens [147], spiders [148], insects [149], tree frogs [150], and geckos [151]. It is also very important for applications involving granular materials [152], particles (e.g., hard disk drives [153], dust filters [154]), nanolithography [155], and aerosols [156]. For a fluid that wets the substrates that it bridges, the combination of the surface tension of the liquid and Laplace pressure in the meniscus leads to an attractive force. [157] The capillary forces of thin water films (low viscosity) and surfaces with simple geometries, such as planes, cones, cylinders, and spheres, have been studied by numerous researchers. [21] Since Matthewson proposed a model for viscous forces between spheres connected by a liquid film[158], the influence of viscosity, initial film thickness, and separation distance on the wet adhesion of simple geometries has been studied in detail. [144][146][159][160] In Nature, many of the surfaces spanned by liquid bridges have complex geometries, such as spiky, hairy, fibrillar and other hierarchically-structured surfaces. These include the adhesive pads on the feet of flies [161], stick insects [162], beetles [149], and spiders [163]. However, knowledge of the wet adhesive mechanisms of viscous liquid bridges between surfaces with such complex geometries is quite limited.

Pollens are well-known microparticles with organized fine-scale surface morphology, [122] and pollenkitt is a liquid adhesive material coating the surface of many pollens, especially those pollinated by animals. [147] Pollens are known to be widely dispersed in Nature and their adhesion to surfaces is critical to their successful transport to the flower stigma. Pollenkitt liquid coatings form capillary bridges that are

significant in dictating the magnitude and humidity dependence of pollen adhesion forces. [89][90] Pollens display a wide variety of structural variations, [122] through evolutionary optimization. [164][165] In addition, the pollen outer shell (exine) is extremely resistant to non-oxidative physical, biological, and chemical degradation. [166] Therefore, the wet adhesion of pollens is an ideal system to study viscous effects on adhesion liquid bridges between complex geometrical surfaces.

In this paper, we report that viscous liquid pollenkitt bridges result in a remarkable dynamic rate-dependent wet adhesion, which is a sensitive function of the size of spiny features on the pollen surface. The adhesion of pollen grains with pollenkitt was studied quantitatively by using atomic force microscopy (AFM). Two pollens with different morphologies (ragweed and sunflower) were used to examine the effect of surface morphology on the wet adhesion mechanism. The magnitude and hydrodynamic response of the wet adhesion due to the shear thinning viscous liquid bridge were modeled by combining expressions for the static capillary and dynamic viscous forces. This model allows accurate determination of pollenkitt viscosity directly from the AFM measurements on pollens. The length of pollen spines is found to control whether the liquid bridges form around a single spine or multiple spines, allowing tuning of the magnitude and dynamic range of viscous forces. Not only do these discoveries offer insight into the mechanisms operative in Nature, but they also are relevant to understanding pollen accumulation in indoor environments. Mimicry of these features may offer inspiration for new adhesion mechanisms for microparticles, particularly those that are responsive to the dynamics of particle detachment speed.

3.3 Experimental

3.3.1 Pollen Preparation

Native non-defatted grains of ragweed (*Ambrosia artemisiifolia*) and sunflower (*Helianthus annuus*) pollens were purchased from Greer Laboratories (Lenoir, NC) and stored at 0 °C prior to use. The pollen grains were immersed in a chloroform and methanol mixture (3:1) for 24 h, [167] in order to extract pollenkitt, before being deposited on filter paper (P5, Fisher Scientific, Pittsburg, PA) supported on a stainless steel 47 mm screen (Kontes Glass, Vineland, NJ) and dried under vacuum at 60 °C for 12 h. A second immersion was conducted in 1 M hydrochloric acid (VWR, Suwanee, GA) for 1 h to remove residual external organic material followed by rinsing three times with deionized water.

3.3.2 Pollenkitt Preparation

The separation and collection of pollenkitt were accomplished by a chloroform and methanol mixture (3:1) solvent extraction from dandelion (*Taraxacum officinale*) as described in a previous study. [95] The dandelion pollens were used as a source of pollenkitt because it was desired to use a single source of pollenkitt when making comparisons of the geometry effects of the two different pollens on viscous forces. In addition, dandelion pollens are coated with a relatively large volume of pollenkitt, about 60 wt%, compared to sunflower (30 wt%) and ragweed (15 wt%) pollen, facilitating recovery of volumes sufficient for rheometry. While it is known that there are differences in the composition of pollenkitt from different plant species, the wetting properties of dandelion and sunflower pollenkitt were almost undistinguishable as reported previously.

[95] The wettability of the dandelion pollenkitt on the surface of both ragweed and sunflower pollens is expected to be very similar because sunflower and ragweed are from the same family (*Asteraceae*) and IR spectra of the surface of both pollens are nearly identical. The solution containing extracted pollenkitt was dried under vacuum for 1 day at room temperature and stored at ambient condition for 5 days. The pollenkitt solution was prepared by re-dissolving approximatively 50 mg as obtained 'dry' pollenkitt in 5 mL of the chloroform and methanol mixture (3:1). Pollenkitt samples with a range of thicknesses from 30 nm up to 2 μm were fabricated on a clean silicon substrate by spin-coating (WS-400, Laurell Technologies Corporation, North Wales, PA) of the pollenkitt solution at 2000 rpm for 1 min.

3.3.3 Force Measurement

Adhesion of pollens was measured using atomic force microscopy (AFM, Veeco Dimension 3100) at different separation rates (from 500 to 67000 nm/s). The AFM cantilever was located 6 μm above the silicon support prior to approach and the same approach rate of 500 nm/s was used for all experiments, even those in which separation rate was varied. Holding the initial approach velocity constant allows for a consistent particle contact with the pollenkitt films as well as an initial volume of liquid wetting the particles. Tipless rectangular cantilevers (Fort-TL, AppNano Inc., Santa Clara, CA) with nominal spring constants of 0.6-3.7 N/m were used to fabricate colloidal probes consisting of a single pollen grain attached by a small amount of epoxy resin (Epoxy Marine, Loctite, Westlake, OH). [127] The actual spring constants for the fabricated cantilevers were directly determined by the methods of Burnham and Hutter et al. [168][169] A series of 3 force-distance curves were measured for separation rates of 500,

1000, 5000, 15000, 30000, and 67000 nm/s. The humidity was controlled under normal air condition (RH of 25-35%), and the loading force on the cantilevers were controlled at 25 nN in all experiments

3.3.4 Scanning Electron Microscopy (SEM)

The surface morphology of the pollen grains was characterized by scanning electron microscopy (SEM) (Zeiss Ultra60 FE-SEM, Zeiss, Germany) at accelerating the potential of 5.0 kV. Cleaned defatted pollens were sputtered with gold and then mounted on metal stubs using carbon tape.

3.3.5 Viscosity Measurement

The viscosity of the pollenkitt solution was measured with a rotational rheometer (PHYSICA MCR 300, Anton Paar) in a cone and plate geometry with a plate diameter of 25 mm. The measurement was performed over a range of shear rate from 1-100 s^{-1} at room temperature.

3.4 Results and Discussion

SEM images of typical ragweed and sunflower pollens utilized in the AFM adhesion experiments are shown in Figure 13. Ragweed pollens have a spherical core shape with fine-scale (800-1000 nm length) spiny asperities (sharp and short) distributed on the surface. Sunflower pollens also have a spherical core with coarser scale (3-4 μm length) surface asperities (blunt and long). The detailed quantitative metrics derived from the images are listed in Table 1. As shown in Figure 13, the exine surfaces of both pollen grains were free of pollenkitt after washing with the chloroform and methanol mixture.

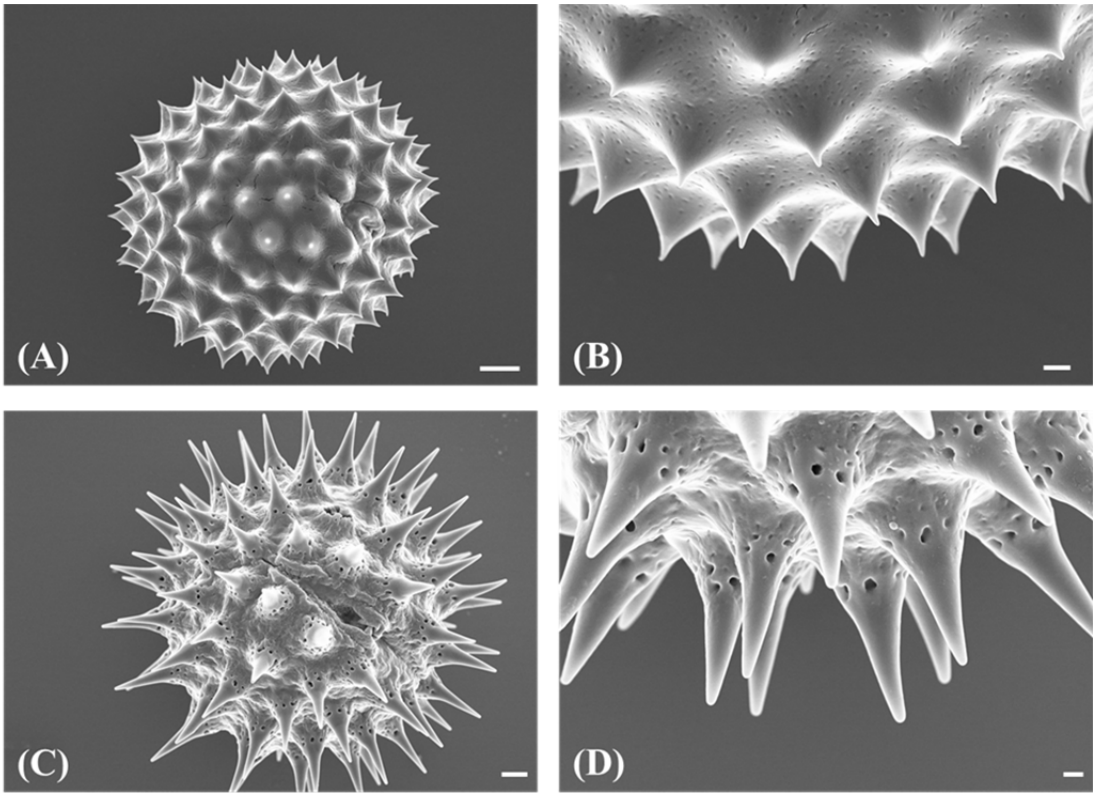

Figure 13 – SEM images indicating the surface morphology of pollen grains: ragweed pollen at low (A) and high (B) magnification, and sunflower pollen at low (C) and high (D) magnification. The scale bars are 2 μm for (A) and (C), and 500 nm for (B) and (D).

Table 1 – Characteristics of pollen grains and surface morphology from SEM image analysis.

Pollen	Size (D, μm)	Average slant of Spines (α, °)	Spine Length (μm)	Spine Tip radius (nm)
Ragweed	15 ± 3	30	0.8 ~ 1	25 ± 3
Sunflower	25 ± 3	9	3 ~ 4	125 ± 10

3.4.1 Differences between Dry Adhesion and Pollenkitt-mediated Wet Adhesion

To provide a pollenkitt-free control, the dry adhesion between cleaned ragweed pollen and Si was measured and is presented in Figure 14 (A). The wet adhesion of ragweed pollen on Si mediated by a pollenkitt liquid bridge is presented in Figure 14 (B). Contributions to dry adhesive forces caused by water condensation on the pollen tip, such as enhanced jump-in distance (step (g) in Figure 14 (C)) or RH-dependent adhesion forces, were not observed over 25-35% RH, in agreement with previous studies. [95] For the 'wet' adhesive studies in the presence of liquid pollenkitt bridges, the control of relative humidity and temperature was important to maintain consistent wetting properties of pollenkitt. No significant changes of pollenkitt wetting and viscous properties was observed between 25-35% RH at room temperature, as reported in a previous study. [90] Within each data set in which the separation rate was varied (both for the dry and wet), the approach curves at an approach rate of 500 nm/s were very consistent and nearly overlapping. The approach curves for wet adhesion showed much stronger jump-in forces (≈ 450 nN) than for dry adhesion, and the jump-in force occurred at a longer separation distance of ~1.8 μm from the Si substrate (Figure 14 (B)). A prominent feature of the results was that the magnitude and range of wet adhesion became stronger as the speed of retraction increased, eventually doubling in magnitude at the highest rate probed of 67000 nm/s. On the other hand, retraction curves of dry adhesion were independent of separation rate (Figure 14 (A)). The jump-in force of the pollen dry adhesion mainly consists of the vdW interaction which has a ~10 nm force range, [89] and the magnitude of the vdW interaction of ragweed pollen is known to be dominated by the interaction between the surface and the single contacting spine tip. The

measured dry adhesion force (40-50 nN) was similar to that observed in a previous study. [95]

In contrast, the jump-in force of the wet adhesion was attributed to the capillary forces of the liquid bridge. [159] Figure 14 (C) shows the wet adhesion events and their correlation with cantilever bending. When the pollen particle contacted (Figure 14 (B)) the liquid surface, the pollen experienced both a capillary force toward the pollenkitt film and the elastic force of cantilever in the opposite direction. The jump-in distance was dependent on the initial thickness of the liquid pollenkitt. [160] The jump-in distance of wet adhesion in this experiment was about 1.8 μm, much longer than for dry adhesion (about 10 nm). The maximum bending of the cantilever by the jump-in force occurred at 1.2 μm above the surface (Figure 14 (C)), and the approach rate of the particle became slower than the cantilever after the maximum bending point due to the viscous resistance of the liquid (Figure 14 (D)). Finally, the pollen didn't move further after it reached the minimum separation distance from the solid surface (Figure 14 (E)).

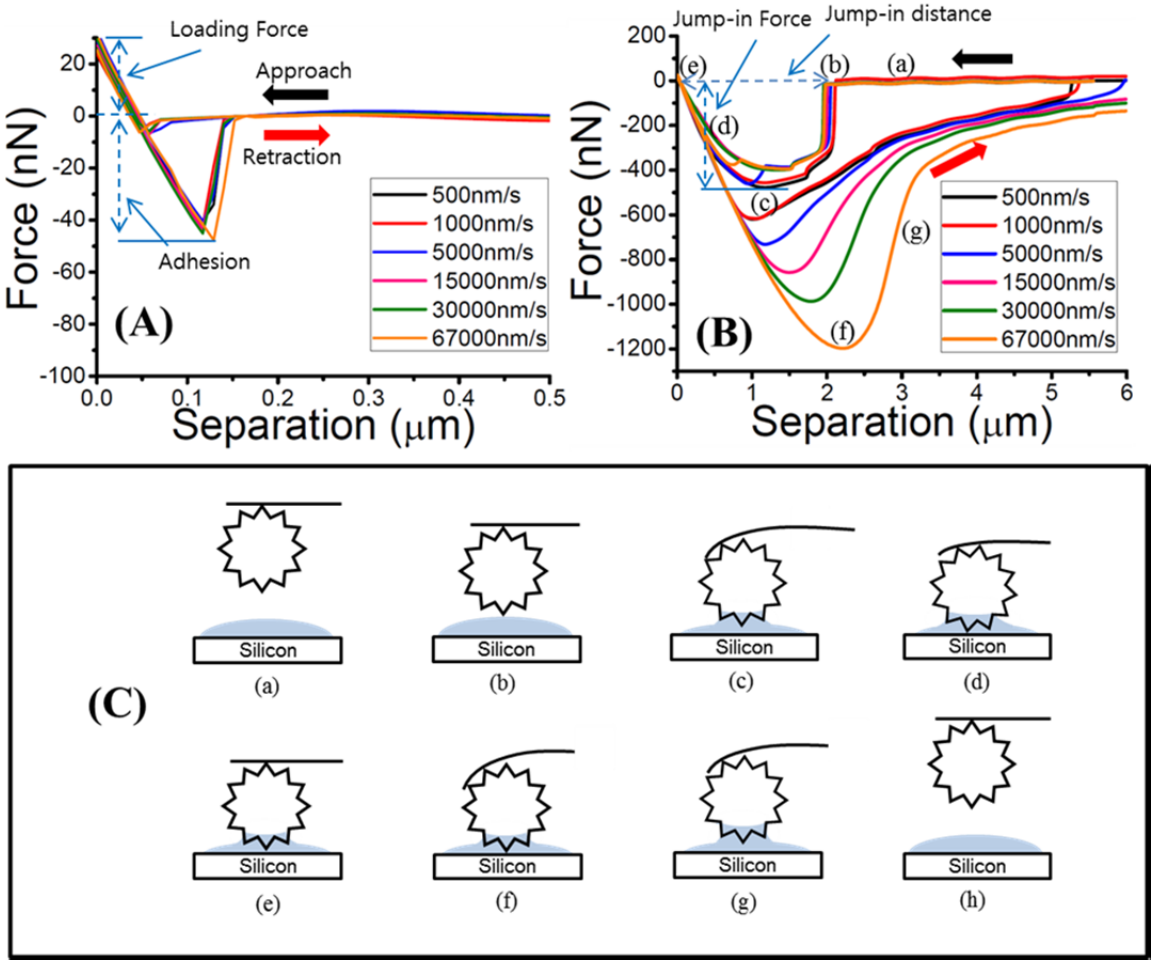

Figure 14 – Comparison of AFM force-distance curves at different separation rates from 500 nm/s to 67000 nm/s. (A) Dry adhesion of ragweed pollen on Si substrate. (B) Wet adhesion between ragweed pollen and pollenkitt film on Si substrate. (C) Schematic of the wet adhesion events ((a) ~ (g) of the curves in (B)) of pollen and pollenkitt showing the response of cantilever bending.

The force magnitude and separation rate dependence of the pollen wet adhesion were significantly different from those observed for dry adhesion. It is well known that two forces, the capillary force (F_c) and viscous force (F_v), mainly contribute to the wet adhesion (F_w) between two solid surfaces bridged by a liquid meniscus. [144][160][170]

$$F_w = F_c + F_v \tag{19}$$

The magnitude of the capillary and viscous forces of ragweed pollen (Figure 14 (B)) can be understood by a wet adhesion model of a spherical particle and a planar surface. This approximation considers the immersion of the core pollen in a liquid film, but ignores the contributions of spine features significantly smaller than the core, which is close to the case of ragweed pollen (Table 1). Multiple step-like features were not observed in the retraction curves of wet adhesion in Figure 14 (B), indicating that a single liquid bridge between the particle core and liquid film is present (as opposed to multiple bridges on individual spines). The SEM image in Figure 13 indicates that the average length of ragweed spines is about 900 nm, about half of the film thickness, allowing the spines to be fully immersed in the pollenkitt film (≈1.8 μm). Thus, the SEM and force profiles are consistent with formation of a single liquid bridge between the spherical core body of the pollen and the solid substrate, instead of having multiple liquid bridges with each spine.

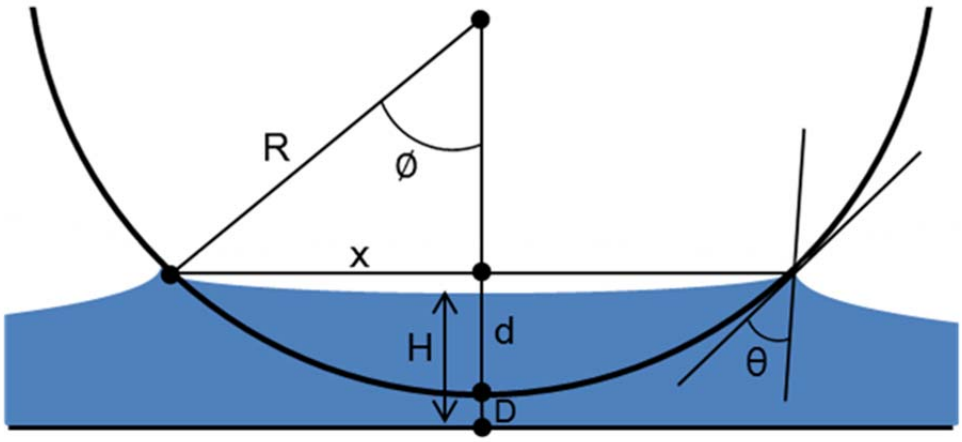

Figure 15 – Schematic of a liquid bridge between a sphere and liquid film. This schematic is relevant to cases in which pollen spines are short enough to be fully immersed in the liquid film, allowing wetting of liquid on the core pollen body.

A rate-dependent response was not observed at retraction rates below 5000 nm/s, and the force magnitude of wet adhesion in this range of separation rates could be explained by the estimated capillary force from the sphere–plane model (Figure 15). The surface tension and Laplace pressure are the two main components of the capillary force. [21][170] The contribution of surface tension to the capillary force at low H ($R >> H$) is small but increases very quickly as H approaches R. In contrast, the contribution of Laplace pressure is the dominant term in the capillary force at low H but decreases very quickly as H approaches R. [170] The capillary force was quantified as shown in Equation (20) by assuming that the Laplace pressure difference in the pollenkitt film is negligible, and evaporation and condensation of liquid during the force measurement are also negligible. [159] These assumptions are justified because the radius of curvature for the ragweed pollen will be in the range of 7.5 μm, which makes the magnitude of the force due to Laplace pressure about 76 nN, clearly low relative to the observed adhesion

forces. In addition, pollenkitt is not volatile and evidence of water condensation during measurements was not observed over the limited RH range used here.

$$F_c = 2\pi\gamma R sin(\emptyset) sin(\emptyset + \theta), \quad (20)$$

where γ is the surface tension of the liquid, θ is the contact angle between the sphere and liquid, and $\emptyset$ is the filling angle indicating the height of the wetting perimeter. One continuous capillary meniscus would encircle the pollen when the liquid film is thicker than the length of spines on the pollen, which is the case for ragweed in the thick film (Figure 14). In this case, the shape and size of the liquid bridge would be more dependent on the core size of the ragweed pollen than the fine-scale spine morphology. The surface tension (γ = 45 mJ/m^2) was taken from a previous study, where it was determined from contact angle measurements. [95] The thickness of the liquid pollenkitt film was approximated by the jump-in distance of the AFM approach curve in Figure 14 (B) as $d + D \approx 1.8$ μm, and the initial separation distance (D) was assumed to be equivalent to the average spine length of ragweed pollen (900 nm). The values of x (3.6 μm) and $\emptyset$ (28°) were estimated from the known values of R and d, by using Equation (21) and (22).

$$x = \sqrt{R^2 - (R - d)^2} \quad (21)$$

$$\emptyset = sin^{-1}(R/x) \quad (22)$$

Pollenkitt is known to wet the surface of pollen, and the contact angle of pollenkitt on pollen is between 0° and 30° as shown in a previous study. [95] Thus, a

value of 15° was assumed for the contact angle between pollen and pollenkitt. Based upon these values, the capillary force estimated by Equation (20) was 690 nN, reasonably close to the actual measured capillary force of 620 ± 15 nN. Both the estimated and measured capillary adhesion forces (Figure 14 (B)) were one order magnitude higher than the dry adhesion forces that are caused by vdW interactions (Figure 14 (A)).

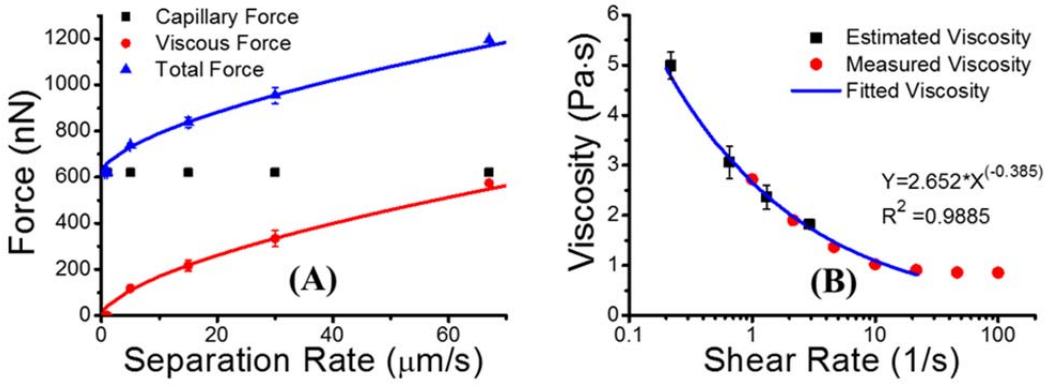

Figure 16 – (A) Capillary and viscous adhesive forces versus separation rate for ragweed pollen in thick (1.8 μm) pollenkitt films. The solid red line is estimated viscous force of ragweed by the proposed model (Equation (25)). The solid blue line is the summation of estimated viscous forces (red line) and the constant capillary force (621 nN) measured at low separation rate. (B) Viscosity of pollenkitt calculated from AFM adhesion forces and measured by rheometer, as a function of shear rate. The solid line is a fitted power law relationship between viscosity and shear rate.

As shown in the retraction curves for wet adhesion in Figure 14 (B), the adhesive forces begin to increase in both magnitude and range at separation rates above 5000 nm/s. The magnitude and range of wet adhesion eventually doubles at the highest rate probed of 67000 nm/s. An explanation of this dynamic response lies in understanding the combined effects of a static capillary force (independent of separation rate) and a dynamic viscous force (rate dependent). Since the capillary forces as modeled by Equation (20), and measured directly to be 620 nN for separation rates < 5000 nm/s, are independent of

separation rate, the added adhesive force that appears at rates exceeding 5000 nm/s is attributed to viscous response. Figure 16 (A) plots both contributions to the adhesive force versus separation rate, noting that all values are taken at the same approach rate of 500 nm/s and loading force of 25 nN. The viscous force between a spherical particle and flat plate, moving along a line normal to both surfaces can be approximated by [171]

$$F_v = 6\pi\eta R^2 \left(\frac{1}{D}\right)\frac{dD}{dt}, \tag{23}$$

which has the form of Stoke's drag on a sphere [$(6\pi\eta R) \times$ velocity] amplified by a geometric factor (*R/D*), where η is the viscosity of the liquid. A dependence of adhesive force on separation rate is described by Equation (23), and while this viscous term is expected to dominate the behavior of highly viscous liquids, it can also become very important for liquids of modest viscosity at high shear rate. The rate-dependent adhesive forces, which appear only at a rate of 5000 nm/s and higher, suggest that the magnitude of the viscous force exceeds the static capillary forces only above this separation rate. To estimate the viscous force by Equation (23), the viscosity of pollenkitt was required. It is well-known that pollenkitt is a viscous liquid, but the rheological property of pollenkitt has not been reported by others. The viscosity of pollenkitt was measured by a cone and plate viscometer (Figure 16 (B) red circles). The viscosity of pollenkitt has a notable shear thinning behavior between shear rates of 1 and 20 s^{-1}, but the shear thinning behavior is not significant at higher shear rates, as shown in Figure 16 (B). We also used Equation (23) and the measured viscous forces to estimate the viscosity of pollenkitt at the different separation rates. To compare the estimated viscosity to measured values, the separation rate (unit of μm/s) was converted to shear rate (s^{-1}) by dividing by the

perimeter of the liquid bridge, $2\pi x$ (x = 3.6 μm, from Equation (21)). The viscosity values calculated from AFM adhesion forces with Equation (23) are shown in Figure 16 (B) as black squares. The independently determined values of viscosity appear to agree well in the range of shear rates that were probed in both rheometry and AFM measurements. In the shear thinning region (below 20 s^{-1}) the rheometry and AFM-based viscosities were fitted to a power law with an exponent of -0.385 (with R^2 = 0.9885) as shown by the blue curve in Figure 16 (B). The relationship between shear rate and viscosity was used to develop a relationship between separation rate and viscosity by multiplying the shear rate by the perimeter ($2\pi x$), resulting in

$$\eta = 8.774 \times \left(\frac{dD}{dt}\right)^{-0.385}. \tag{24}$$

Combining Equation (23) with the viscosity given by Equation (24), the viscous forces over separation rates from 0.5 μm /s to 70 μm /s can be estimated by Equation (25) (solid red line in Figure 16 (A)).

$$F_v = (8.774)\left(6\pi R^2 \left(\frac{1}{D}\right)\right)\left(\frac{dD}{dt}\right)^{(1-0.385)} \tag{25}$$

By using this approach, the magnitude of the viscous forces between pollen and pollenkitt were successfully modeled. The calculated viscous and total adhesive forces in Figure 16 (A) (solid lines) also suggest that the contribution of viscous force on total wet adhesion is not significant (less than 6.3 % of total force) at separation rates below a critical value (5000 nm/s). However, the viscous forces become comparable to the capillary force near this critical value, and dominates the adhesion at higher separation rates.

3.4.2 The Influence of Pollen Surface Morphology on Wet Adhesion with a Thick Films (1~2 μm)

To investigate the effect of surface morphology on wet adhesion mechanisms, a pollen species with significantly larger spines than ragweed was also studied, sunflower pollen. Sunflower pollens have a larger core radius and possess spines that are more than twice as long as ragweed pollens (Table 1).

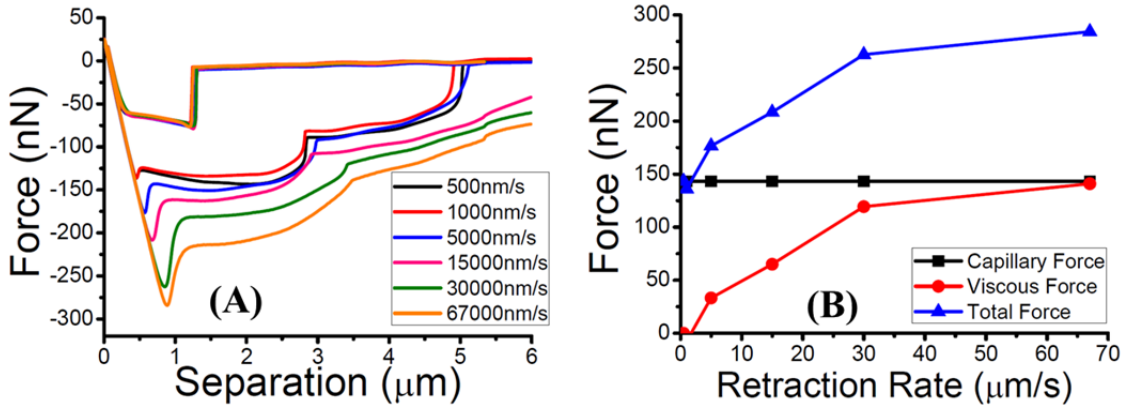

Figure 17 – (A) Adhesion versus separation distance for sunflower pollen and a thick pollenkitt liquid film (thickness, 1.2 μm) on a Si substrate. (B) Capillary and viscous forces from wet adhesion of sunflower pollen as a function of separation rate.

Figure 17 (A) shows the AFM force-distance curves for wet adhesion of sunflower pollen with a thick pollenkitt liquid bridge (initial thickness, 1.2 μm) at different separation rates (500 - 67000 nm/s) on Si. The loading force was set at 25 nN, and the separation distance was set at 6 μm. The sharp jump-in events in the force curves (Figure 17 (A)) showed that the sunflower probe reached a maximum bending sooner than ragweed ((b) and (c) in Figure 17 (B)). The dry adhesion force, reported previously to be 60 ± 8 nN [95], is significantly less than the wet adhesion observed here in the presence of pollenkitt. Like

the case for ragweed, sunflower wet adhesion increased with separation-rate at rates ≥ 5000 nm/s. However, compared to the wet adhesion of ragweed, the wet adhesion was one order lower magnitude for sunflower pollen. In addition, unlike ragweed, sunflower showed multiple step-like features during probe retraction.

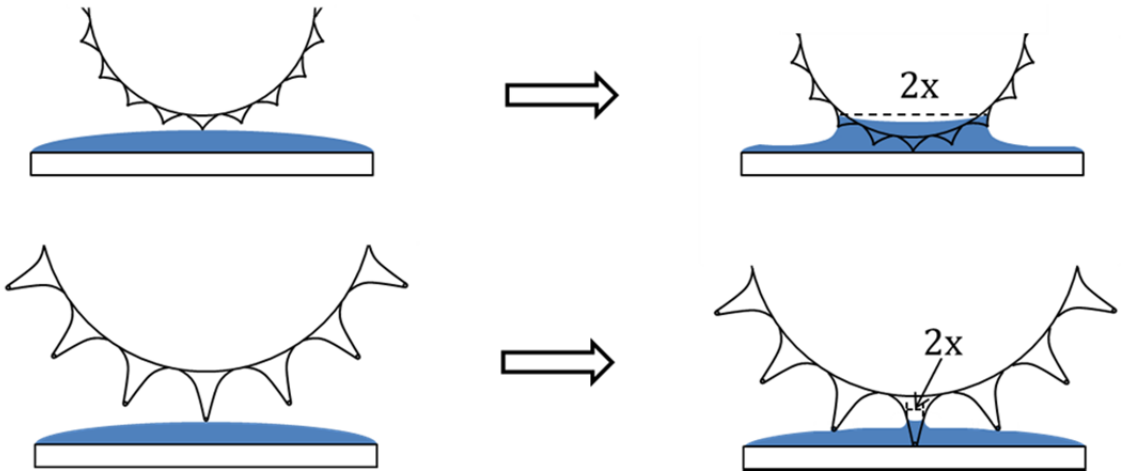

Figure 18 – (A) Schematics of liquid bridges formed by ragweed (top) and sunflower pollen (bottom) on a 1.5 µm thick pollenkitt film. The drawings are based on the known ratios of the sizes for pollens and pollenkitt films.

The magnitude and shape differences between the force-distance (both approach and retraction) curves of ragweed and sunflower pollen illustrate an important effect of fine-scale surface morphology on capillary adhesion. Figure 18 shows general features of the expected shapes of liquid bridges for ragweed and sunflower pollens immersed in a 1.5 µm thick pollenkitt film, based upon the known size and geometry of the spines and the core pollen. When the pollens contact the surface of the liquid film, the pollens are pulled toward the pollenkitt film due to an attractive capillary force. A liquid bridge with a larger radius (x) can be generated by ragweed because the longer spines of sunflower pollen (average length of spine, 3.5 µm) act as offsets that prevent contact between the core pollen and the liquid film. Therefore, a much smaller liquid bridge was generated

between the spine of sunflower pollen and the solid support (Figure 18 (bottom)). Based on geometry alone, it is apparent that compared to the sunflower pollen, a larger volume of pollenkitt can be contained in the meniscus of the approaching ragweed pollen. Therefore, the resistance of the approaching movement of ragweed pollen by shear stress was stronger than sunflower pollen, and it caused the delay of the snap-on event in the approach of the ragweed pollen, as shown in Figure 14 (B) (between (b) and (c)). On the other hand, the snap-on event in the approach curve of sunflower pollen didn't show notable delay, as shown in Figure 17 (A), because a relatively smaller volume of pollenkitt was associated with the approach of sunflower pollen. For the same reasons (volume of pollenkitt in liquid bridge), the retraction sunflower pollen shows a weaker wet adhesion magnitude than the ragweed pollen at this film thickness.

According to the approach curve of the sunflower pollen probe in Figure 17 (A), the thickness of the pollenkitt film can be estimated around 1.2 μm, much larger than the radius of sunflower spine (125 ± 10 nm), but smaller than the length of the spines (3-4 μm). This geometry resembles an immersed conical cylinder in an infinitely large film. The most common and simple method to calculate capillary adhesion in this geometry is the Wilhelmy equation [$F_c = \gamma \times$ perimeter $\times$ projection factor], which is the capillary force component of a cone-plane geometry due to the direct action of surface tension [21][172]

$$F_c = \gamma(2\pi x)\cos(\alpha - \theta). \tag{26}$$

The radius (x = 290 nm) of a contact line between liquid and the spine of a sunflower pollen was approximated as the spine cross-sectional radius when the spine is

immersed to the full depth of the liquid film (1.2 μm). Analysis of SEM images of single spines (Figure 13 (D)) allowed calculation of the cross-sectional radius based on knowledge of the average slant angle α, measured to be 9° (Table 1). The contact angle between pollen and pollenkitt was taken to be 15° as described in Table 1. Based on these values, the estimated capillary force between sunflower pollen and pollenkitt by Equation (26) was about 82 nN, a magnitude that is 58 % of the measured force, 140 nN (Figure 17). The orientation of the AFM probe pollen is not necessarily with one spine absolutely perpendicular to the substrate, i.e., more than one spine may make contact. Hence, the estimated force of 82 nN is reasonable for one spine. In fact, two retraction steps were observed on the retraction curves of sunflower pollen on Figure 17 (A), indicating that two liquid bridges were formed, which would lead to a force of approximately 160 nN, close to the measured result.

The measured and estimated capillary forces of sunflower pollen were about 4-5 times less than the estimated (690 nN) and measured (620 nN) capillary forces of ragweed pollen. The viscous force of ragweed was also 3-4 times stronger than the viscous force of sunflower pollen, and this force difference between both pollens can be explained by the meniscus area difference. According to a previous study of the effect of meniscus area on wet adhesion [144], meniscus area roughly scales as πx^2 and is an important factor in both capillary and viscous wet adhesion. When surface tension is dominant to capillary forces, viscous force, proportional to (meniscus radius)^2, is more sensitive to the meniscus radius and area than is the capillary force, proportional to meniscus radius, as seen in Equation (20), (5), and (8). The estimated meniscus area on a ragweed pollen immersed in a liquid with thickness of 1 - 2 μm was about 4.7 to 48 μm^2,

much larger than the meniscus area on an immersed sunflower pollen spine, 0.22 to 0.56 μm^2. These roughly 'order of magnitude' differences correlate approximately to differences observed in the adhesive forces between ragweed and sunflower pollen in liquid pollenkitt thick films.

3.4.3 The Influence of Surface Morphology on Wet Adhesion with Thin Films (below 800 nm)

Wet adhesion of both pollens was decreased as the pollenkitt thickness decreased. Figures 19 (A) and (B) show the force-distance curves of ragweed and sunflower pollen with thin pollenkitt films (thickness of 66 nm (sunflower) and 86 nm (ragweed)). The magnitude of wet adhesion for both pollens was much smaller compared to the wet adhesion with thick pollenkitt films (Figure 16 (A) and Figure 17 (A)). The magnitude of the capillary contribution of both pollens with thin films was not very different (Ragweed 48 nN and Sunflower, 52 nN), but the viscous force of the sunflower was much higher than the ragweed pollen, and it indicated that sunflower pollen had a more sensitive hydrodynamic response. This behavior of the viscous force is not observed for thick pollenkitt films.

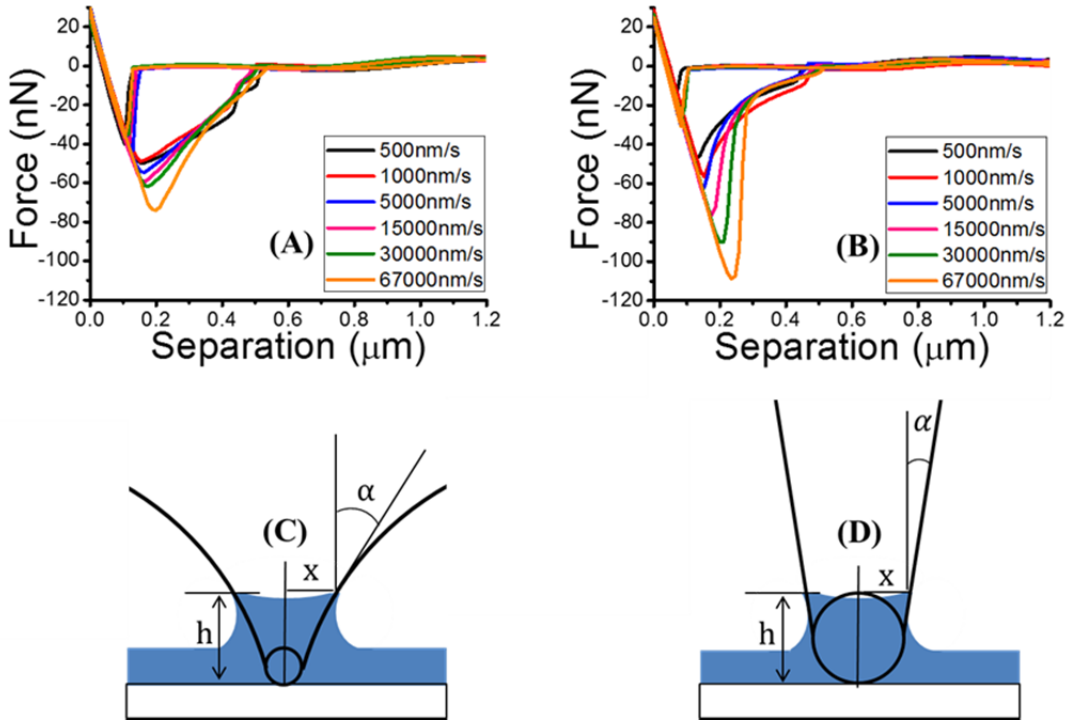

Figure 19 – Adhesion versus separation distance of pollen immersed and retracted from thin pollenkitt films: (A) ragweed pollen. (B) sunflower pollen. Schematics of the liquid bridges formed on a spine of ragweed (C) and sunflower pollen (D), drawn to scale based on the relative spine sizes.

By assuming that the surface tension dominates the capillary force, the capillary forces can be estimated by Equation (26). The values of $\boldsymbol{\alpha}$ and x (in Figure 19 (C) and (D)) of both pollen spines were directly measured from SEM image of the spines. The spines of ragweed are curved and the $\boldsymbol{\alpha}$ increases from 12° to 37° as h increases from 100 to 750 nm (Figure 20). The $\boldsymbol{\alpha}$ value of sunflower was comparatively constant around at 9° as h is above 300 nm, and the contact angle of pollenkitt on pollen was taken to be 15°. Based on Equation (26) and measured forces, the x values of the pollen liquid bridges were estimated. The x value of the liquid bridge of ragweed pollen was estimated to be 180 nm by using the measured capillary force at low separation rate in Equation (26) and solving for x. The corresponding height of the liquid bridge (h) was estimated

to be 450 nm based on the spine geometry determined from SEM analysis, as shown in Figure 20 (A). In the same manner, the x value of sunflower pollen was estimated to be 180 nm, and the height of the liquid (h) was estimated to be 375 nm (Figure 20 (B)), which is 17 % thinner than the h of ragweed. The thinner h value of sunflower pollen is reasonable because the initial pollenkitt film thickness of sunflower pollen was about 66 nm (jump-in distance from Figure 19 (A)), which was 23 % thinner than the initial pollenkitt film thickness used for the ragweed pollen experiments (86 nm, from Figure 19 (B)). The larger tip radius of spines on sunflower pollens resulted in a larger liquid bridge radius compared to ragweed. Therefore, the thinner h of the liquid bridge for sunflower 'corrects' for the effects of the larger sunflower spine size, and results in a similar magnitude of capillary force as the smaller sized ragweed pollen, as shown in Figure 19 (A) and (B).

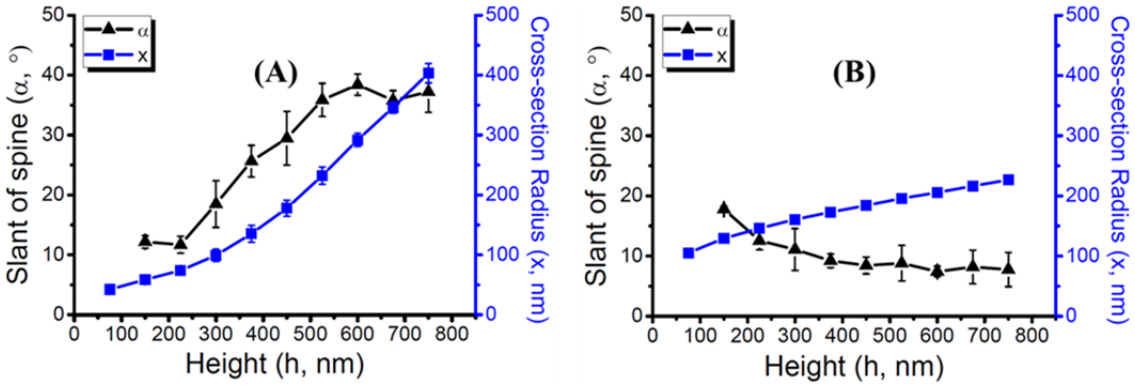

Figure 20 – The slant angle and cross-sectional radius based on SEM image analysis of (A) ragweed pollen, (B) sunflower pollen as a function of position along the spine length.

The remarkable difference in hydrodynamic response of the pollens in the thin pollenkitt films relative to the thick films can be explained by two different factors: the submerged volume and the separation distance between the spine and substrate. For

example, the estimated contact radii (x) of both pollen spines in Figure 20 were close when the h was around 450 nm, so the capillary forces (ragweed 48 nN, sunflower 52 nN) estimated by Equation (26) are also close at h = 450 nm. However, the volume of the solid sunflower pollen spine submerged to the 450 nm depth of liquid was about 0.027 μm^3, more than twice as large as the submerged volume of the ragweed spine of ragweed pollen (0.012 μm^3). The submerged volumes of the spine of both sunflower and ragweed were calculated by the summation of the local volumes of the 5 conical cylinders located on a spine at the different regions of height (between 75 ~ 150 nm, 150 ~ 225 nm, 225 ~ 300 nm, 300 ~ 375 nm, 375 ~ 450 nm), and the top and bottom radius of the cylinders for this estimation were achieved from the Figure 20 (A)). (The volumes below h < 75 nm were negligible for both pollens since those are much smaller than the rest of all, < 10 % of total volume) A larger volume of liquid must be displaced to 'fill' the space associated with the retraction of sunflower pollen than ragweed pollen. Moreover, the average separation distance between the immersed surface of the sunflower spine and the substrate is narrower than for the ragweed pollen, as shown in Figure 19 (C) and (D). We were not able to use viscous force model formulae for this thin film studies, because the separation distances between the spine tips and substrate surfaces are too problematic to be defined. Therefore, qualitative approach was utilized for explaining the influence of the surface morphology of both pollens on viscous force. As a result, a stronger viscous force can be generated during the retraction of the sunflower pollen due to the need to transfer a larger volume of liquid through a narrower path, compared to the ragweed. Therefore, the sunflower pollen is expected to have a stronger hydrodynamic response compared to the ragweed pollen in the case of thin films, as shown in Figure 19.

3.4.4 The Correlation of Surface Morphology and Film Thickness Effects

Based on the geometrical information of spines and pollens from SEM images (Figure 20), the relationship between capillary force and the height (h) of the liquid bridge from 150 nm to 2000 nm could be estimated as shown in Figure 21 (D). When h is below 800 nm (the length of the spine on ragweed pollen), Equation (26) (cone-plate model) was used to estimate the capillary forces of both pollens. As shown in Figure 20 (A), the x values (radius of liquid bridge) of ragweed pollen at different h values (h_0 = 75 nm, h_{n+1} = h_n +75 nm) were directly measured from SEM images of ragweed pollen (Figure 13 (B)), so α values (in Figure 21 (A)) can be estimated by

$$\alpha_{n+1} = tan^{-1}(\frac{x_{n+1} - x_n}{h_{n+1} - h_n}). \quad (27)$$

Therefore, the capillary forces of ragweed pollen at different h values (below 800 nm) can be defined as

$$F_{c,n+1} = \gamma(2\pi x_{n+1})cos(\alpha_{n+1} - \theta), \quad (28)$$

where the contact angle (θ) and surface tension (γ) are taken to be 15° and 45 mJ/m^2, respectively, based on previously reported measurements. [95]

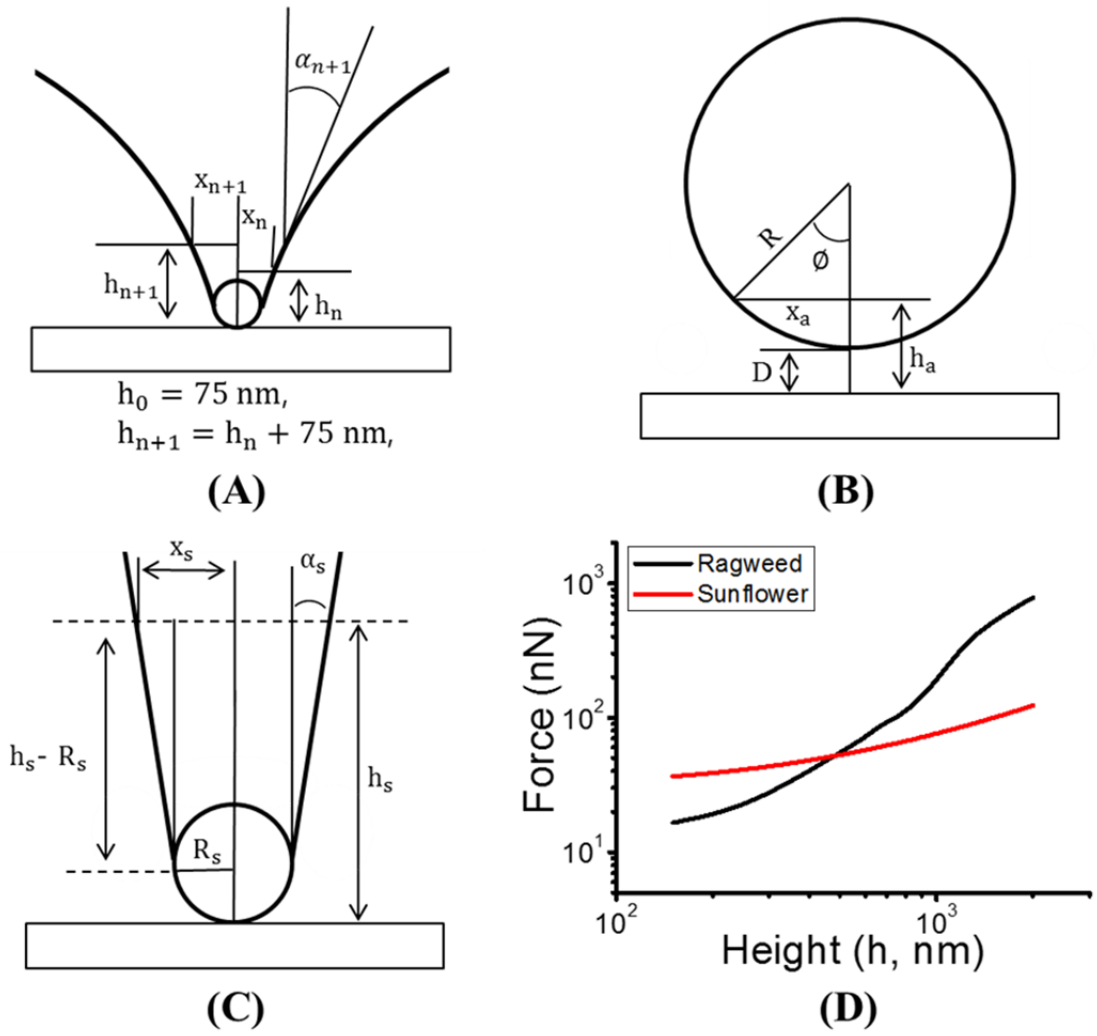

Figure 21 – The slant angle and cross-sectional radius based on SEM image analysis of (A) ragweed pollen, (B) sunflower pollen as a function of position along the spine length.

The spherical-planar surface model (Figure 21 (B)) was used to estimate the capillary force of ragweed pollen when the thickness of liquid film is above the length of the spine on ragweed (800 nm), h_a. The x_a on Figure 21 (B) was calculated by

$$x_a = (R^2 - (R + D - h_a)^2)^{0.5}, \quad (29)$$

where the R is the radius of ragweed pollen (7.5 μm) and the D is the length of ragweed spine (800 nm) and the filling angle $\emptyset_a$ value was calculated by

$$\emptyset_a = sin^{-1}(R/x_a). \quad (30)$$

Therefore, the capillary force of ragweed pollen at h values above 800 nm can be defined as [159]

$$F_{c,a} = 2\pi\gamma R sin(\emptyset_a) sin(\emptyset_a + \theta). \quad (31)$$

Equation (26) (conical-plate model) was used to estimate the capillary force of sunflower pollen, because over the thickness range explored, the sunflower spines are never fully submerged. The average slant of the spine of sunflower pollen (α_s) on Figure 21 (C) was measured around $9.4 \pm 0.8°$, and the x_s was calculated by

$$x_s = R_s + (h_s - R_s) tan(\alpha_s), \quad (32)$$

where R_s is the radius of the spine tip of sunflower pollen (125 nm). Therefore, the capillary forces of sunflower pollen at different h values can be defined as

$$F_{c,s} = \gamma(2\pi x_s) cos(\alpha_s - \theta). \quad (33)$$

When the height of the liquid bridge is below 485 nm, the model predicts that the sunflower pollen generates a stronger capillary force than ragweed pollen (Figure 21 (D)). The ragweed pollen is predicted to have a stronger capillary force than sunflower when the height of the liquid bridge is thicker than 485 nm. Especially, when the height was

above the length of the ragweed spine (> 800 nm), the capillary force of ragweed was dramatically increased because a large liquid bridge was formed on the core body of ragweed pollen (not just on one or two spines).

While the quantitative calculations of Figure 21 (D) are limited to the capillary static force, we can also speculate about the influence of spine length and liquid height on the viscous forces. A full calculation of the viscous forces for the spine geometry in transitioning from the cone-plane to sphere-plane geometry as *h* increases is beyond the scope of this work. As mentioned previously, the meniscus area plays a significant role in determining the magnitude of the viscous force. [144] As shown in Figure 20, the cross-sectional radius of the contact line (*x*) of ragweed pollen was smaller than the sunflower when the liquid height *h* was less than 485 nm, but it became much larger than the sunflower pollen when *h* was larger than 485 nm, so the meniscus areas (πx^2) of both pollens have a proportional relationship with the liquid height (*h*). Therefore, the ragweed pollen has stronger viscous forces at higher liquid height (*h*) as shown in Figure 14 (B) (570 nN, *h* = 1.8 μm and separation rate at 67 μm/s), but not at low *h* as shown in Figure 19 (A) (27 nN, *h* = 86 nm and the separation rate at 67 μm/s). The meniscus area of sunflower pollen does not change significantly with the liquid height because of the narrow slant angle, and the sunflower pollen had similarly strong hydrodynamic responses for both thin and thick films as shown in Figure 17 (A) (140 nN, *h* = 1.2 μm and separation rate at 67 μm/s) and Figure 19 (B) (60 nN, *h* = 66 nm and separation rate at 67 μm/s).

3.4.5 Relevance to Natural Pollen System and Structural Influence on Dynamic Sensitivity

Variation of stickiness of angiosperm pollens (both wind- and animal-pollinated pollens) as a function of pollenkitt and of fine-scale morphology on the pollen surface has been observed in Nature. [164] For example, it is well-known that animal-pollinated plant pollens are covered by a large volume of pollenkitt and these species tend to have more spiny surface morphologies, compared with wind-pollinated pollen species. [165] The animal-pollinated pollen should have more tunable adhesive strength, based on dynamic conditions for animal pollinators, than the wind-pollinated pollen because the zoophilous pollens should be held on an anther as pollinator arrives at the flower, but then be easily transferred to a pollinator surface. In contrast, anemophilous pollens need to be able to detach from the anther under drag forces produced by ambient wind flow. The drag forces can be roughly estimated as ~40 nN for a sphere (with a radius of 7.5 μm, same size as ragweed core) under a 13.8 m/s wind speed (a strong breeze based on Beaufort Wind Scale [173]) by using the Stokes' law. In addition, the zoophilous pollens must remain attached on a pollinator, resisting detachment due to the drag forces experienced during transport (flight), and the estimated drag forces on a sphere (based on a radius of 12.5 μm, same size as sunflower core) under the 13.8 m/s air flow is around ~60 nN. The quantitative analysis of dry and wet adhesion in this paper supports the previous qualitative understanding of the adhesive role of pollenkitt. The adhesion of sunflower pollen, which is on the order of 60 nN in the absence of pollenkitt, can be enhanced by pollenkitt by an order of magnitude, to the ~300 nN range under dynamic fast pull-off velocities. This increase is enough to resist detachment under drag forces produced by

winds in the range of 70 m/s, so it can be expected to resist detachment under the aerodynamic drag experienced during flying. A previous study proposed that the surface morphology of pollen, combined with the pollenkitt, can facilitate animal-pollinated pollen dispersal. [147] The animal-pollinated grains are packed by a large amount of fully hydrated pollenkitt, so the pollens become a mass of pollens and pollenkitt inside the developing anther. The mass of pollen and pollenkitt becomes partially dehydrated after anther opening, and the thickness of pollenkitt between the outer grains get thinner, so grains on the outside of this mass become easier to remove by a pollinator. [147] Pollens collected by pollinators might have different volumes of pollenkitt on their surfaces, and the volume could be changed by dehydration or water absorption [90], dependent on the environmental humidity, during their transport. In the previous sections, it was shown that the larger scale of the surface structure of sunflower pollens helps to keep the tunable adhesive property, based on dynamic condition, on both thin and thick pollenkitt films. This is consistent with the observation that sunflower is zoophilous whereas ragweed is primarily anemophilous, as well as the more general observation that zoophilous varieties have generally more elaborate morphology than smooth anemophilous ones. [165]

3.5 Conclusion

The wet adhesion of a pollen to pollenkitt has a strong dynamic response (viscous force) at separation rates of 5 μm/s and above, which is a lower threshold for dynamic response compared with other rate-dependent adhesives system in Nature, such as spider webs with adhesive glue (at 10 μm/s and above) [148], gecko setae (at 20 μm/s and above) [174], and stick insect's pads (above 100 μm/s) [88]. This special feature is due to the relatively high viscosity (above 1 Pa·s) at low shear rate, even though the fluid

exhibits some shear thinning between shear rates of 0.1 to 20 s^{-1}. The contribution of viscous force to wet adhesion increased with separation rate and the viscous force approached or exceeded the capillary force at separation rates above 67 μm/s. The rate-dependence of the adhesion between ragweed pollen and pollenkitt was successfully modeled by a combination of capillary and viscous force models. The required information for both models was available from AFM force-distance curves (liquid film thickness and force magnitude) and SEM image analysis (distance between the core body and surface and contact radius of liquid bridge). The size and shape of the pollen external surface features tunes the sensitivity of hydrodynamic response to the thickness of pollenkitt films. The ragweed pollen had stronger capillary and viscous forces in thicker liquid films (1-2 μm), compared to sunflower pollen, but the sunflower pollen had stronger wet adhesion and more sensitive hydrodynamic response in thinner liquid films (below 800 nm). The reversal of the wet adhesion magnitude of both pollens is affected by both the length and shape of spines on the surface of both pollens as well as the thickness of the fluid layer. These sensitivities of dynamics to geometry suggest new approaches to tuning particle adhesion and detachment in applications ranging from target drug delivery to reversible adhesives.

CHAPTER 4. HUMIDITY-STABILIZED VISCOUS ADHESION OF THE HONEY BEE POLLEN BASKET FLUID

4.1 Overview

Honey bees are well known to utilize secretions to moisturize and adhere pollen grains in their pollen baskets. Many bee-pollinated plant pollens are also pre-coated with plant-derived liquid pollenkitt. Herein, we reveal for the first time the presence of two immiscible liquid phases in the bioadhesive of the pollen basket. The bioadhesive consists of a sugar-based adhesive (aqueous phase, 90 wt%) generated by bees and pollenkitt-derived (oily phase, 10 wt%) coated on pollens. We demonstrate the separate functions of each phase in generating reliable wet adhesion under widely varying humidity. The sugary aqueous phase shows a remarkable rate-dependent capillary adhesion force attributed to a hydrodynamic force that dominates above a critical separation rate. However, the performance of the sugar-based adhesive phase alone is very sensitive to humidity due to water loss or uptake. Interestingly, the pollenkitt-based oily phase contributed very little to the observed wet adhesion. Rather, it spreads over the aqueous phase and serves as a barrier that tempers the effects water transport under high or low humidity conditions. This action stabilizes the viscosity of the aqueous phase during humidity changes, thereby stabilizing the viscous force contributed by this phase. This finding serves to support a continuing understanding of the physical mechanisms of pollination, and as the basis to inspire the development of humidity-stable adhesive materials.

4.2 Introduction

Bioadhesive systems often show unpredictable functionalities, inspiring many studies to elucidate their adhesive mechanisms [13, 88, 93, 95, 175] and mimic their functionality to improve the performance of synthetic adhesive systems. [85, 97, 176–178] For example, the adhesive pads on geckos suggest methods for creating strong and reversible dry adhesion [177] and numerous as a result various groups have tried to mimic gecko adhesive functionalities. [37][179] The barbed proboscis of an endoparasitic worm swells to create strong mechanical interlocking after embedding in the soft tissue of its host, [180] inspiring improved attachment reliability of microneedle patches on human skin [97]. Structural and experimental investigations of insect adhesive systems encourage the development of micropatterned adhesive tape for robotic applications. [181]

Pollen is a significant nutrient source for bees, [182] and their efficient collection and transport is essential for survival. Pollen grains (reported loading range from 8.4 to 23.4 mg [183]) are packed by the bees into pellets, carried on each hind leg in a structure called a corbicula, or “pollen basket”. [184] Generally, two full pollen pellets is known to have a mass near 20 mg, [183] which is more than 25% of the average body mass of the honey bee. [185] Reliable attachment of the heavy pollen pellets on the hind legs is essential during flight (average velocity, 19 km/h). [186] Honey bees utilize salivary secretions or nectar to adhere pollens together into a pellet and hold them on the corbicula hair. [187][188] The bees harvest pollens at a wide range of humidity since the relative humidity in natural environment keeps changing hourly and daily. Therefore, one may expect the liquid adhesive in the pellets to employ a mechanism to counteract

changes in physical properties due to water loss or uptake associated with variations in humidity. Despite the importance of these fluids in pollinator health, the adhesive mechanisms of the liquid secretion in the bee pollen pellets have not been studied extensively.

Maintaining the performance of synthetic adhesives after water uptake is a crucial challenge for the adhesive applications [189] and synthetic adhesives exhibit adhesion loss when a critical relative humidity is exceeded. The mechanisms of adhesion loss are still an issue of adhesive studies, and it is generally agreed that the absorbed moisture from the humid air changes physical and chemical properties of the adhesive. [190] Evolutionary-adapted adhesive systems in nature show strategies for maintaining adhesive properties under high relative humidity or even under water. For examples, geckos [191] and ladybird beetles [192] show higher adhesion under a humid environment because absorbed moisture causes adhesive structures to swell and soften, leading to larger contact areas between their adhesive systems and rough surfaces. Some spiders utilize the moisture from the humid air to manipulate the viscosity of spider glue to maximize adhesion. [193] Furthermore, mussels, [176] torrent frogs, [86] and beetles [194] utilize structural or chemical properties of their adhesive systems to generate reliable underwater adhesion. An understanding of the adhesive mechanism and humidity dependence of the liquid secretion used in bee pollen pellets may enable a better understanding of environmental factors affecting pollinator nutrition. In addition, it is expected to support novel biomimicry strategies to develop humidity-tolerant synthetic adhesives.

Herein, we investigate the adhesive properties of the liquid secretion in the pollen basket (named as pb-adhesive in this paper) of honey bees. We observed that aqueous and oily phases are present in the pb-adhesive of honey bees. The aqueous phase was a well-known adhesive secretion generated in the honey stomach of bees, reported by other studies, [187, 195] and the oily phase was suspected to be a pollenkitt, a lipid oil coat on pollen grains. [196] We measured the wet adhesion of sunflower pollen on the both phases via colloidal probe microscopy, and remarkable rate-dependent and strong adhesive properties were observed from the wet adhesion of the aqueous phase generated by bees. We also observed the ability of the oily phase coat (pollenkitt) to stabilize the physical properties of the aqueous adhesive relative to humidity changes. Without the pollenkitt, significant adhesion loss was observed for the aqueous phase at low and high relative humidity extremes. Adhesion loss was significantly curtailed (by a factor or more than 2) with the oily phase coat present.

4.3 Materials and Methods

4.3.1 Bee pollen and Bioadhesive Sample Preparation

The bee pollens (Dandelion, *Taraxacum officinale*) collected by honey bees (*Apis mellifera)* were purchased from Greer Laboratories (Lenoir, NC), stored in unopened container at -18 °C and used as received without further purification. To collect sufficient quantities of pb-adhesive fluid, 35 mg of dandelion pollen was deposited on a piranha-etched silicon wafer and held at 20 °C (57% RH) for 24 h to allow time for the fluid to drain. The pollen grains were subsequently removed by blowing with nitrogen gas, leaving pb-adhesive droplets on the silicon wafer. These droplets were used for

characterizations described below. To isolate the aqueous phase of the pb-adhesive without the oily phase, droplet samples were immersed in toluene for 1 min, followed by drying in a fume hood for 30 min. Prepared samples were stored in chambers at different relative humidities of 15, 35, 57, 75, and 92% RH for 24 h. Humidity in the chambers was controlled by solid salt (15% RH - calcium chloride) and supersaturated salt solutions (35% RH - calcium chloride, 57% RH - calcium chloride and sodium chloride, 75% RH - sodium chloride, and 92% RH – sodium bicarbonate). Three humidity-conditioned pb-adhesive droplets (with similar thicknesses in the range 1.5-1.7 μm) in each of the humidity chambers were chosen for the adhesion measurements. The thicknesses of the droplets were measured by an atomic force microscope (AFM; Veeco Dimension 3100, Santa Barbara, CA) with pyramidal-tipped scanning cantilevers (tapping mode, 0.75 Hz scanning rate) (ACTA, AppNano Inc., Santa Clara, CA).

4.3.2 Solvent Extraction

The two liquid phases in the pb-adhesive were extracted and separated by a solvent extraction with toluene and water. 2 g of the dandelion pollens were dispersed in 20 ml of toluene, and the solution was gently shaken for 30 s. Most of the pollens settled on the bottom of the container within 30 s after shaking stopped. Only the toluene solution (orange color) was carefully transferred to another container by syringes with syringe filters (1μm, 200 nm). 20 ml of water were added to the toluene washed pollens remaining in the container, and the pollens were dispersed in the water for 60 s. The pollens dispersed in the water solution were filtered by syringes with syringe filters (1 μm, 200 nm) to collect the water solution. Each solution was moved to a vacuum chamber, and the solvents (water and toluene) were evaporated under vacuum.

4.3.3 Sample Characterization

4.3.3.1 Confocal Fluorescence Microscopy.

Raman spectra of samples were obtained using a Thermo Scientific Nicolet Almega XR spectrometer (Waltham, MA) with a 488 nm laser excitation source at 20 °C (40 ± 5% RH), and 10 scans were obtained for each sample. The laser beam was focused on the samples by using a 50X objective. A confocal aperture of 100 μm pinhole was chosen, and the estimated spot size was 0.7 μm.

4.3.3.2 Confocal Raman Spectroscopy

Raman spectra of samples were obtained using a Thermo Scientific Nicolet Almega XR spectrometer (Waltham, MA) with a 488 nm laser excitation source at 20 °C (40 ± 5% RH), and 10 scans were obtained for each sample. The laser beam was focused on the samples by using a 50X objective. A confocal aperture of 100 μm pinhole was chosen, and the estimated spot size was 0.7 μm.

4.3.3.3 Physical Properties

Density of both phases was estimated by measuring the mass of the each phase in unit volume, and the surface tension of both phases was measured using a ramé-hart automated goniometer (290-G1, Succasunna, NJ) with DROPimage Advanced software at 20° C and at 57% RH. For the viscosity test of the aqueous phase, three aqueous phase samples (1 mL) were stored in different relative humidity chambers (30%, 57%, 75% RH) for three days, and the viscosity of the samples was measured using a parallel-plate rheometer (MCR 302, Anton Paar, Austria) at 20° C as a function of shear rate. In

addition, the viscosity at the different temperature in the range of 20-40° C (the step size of the temperature change, 0.1° C/s) were also observed at a 10 s^{-1} shear rate.

4.3.4 Adhesion Measurement

Adhesion of a sunflower pollen (*Helianthus annuus*) (Greer Laboratories, Lenoir, NC) on a pb-adhesive and an extracted aqueous phase droplet was measured by colloidal probe microscopy by using the same AFM described above. Sunflower pollens were utilized in adhesion force measurement of pb-adhesive obtained from dandelion pollens. They have much more uniformly distributed surface features than dandelion, [95] and that allows precise control over the wetting volume of fluid for wet adhesion measurement. The dandelion pollens were chosen simply because they are known to carry a large quantity of pollenkitt. [95] The pollenkitt of sunflower and dandelion pollens are known to have almost same surface tension and composition due to their derivation from the same family (*Asteraceae*). [95] To fabricate sunflower pollen probes, native non-defatted sunflower pollens were washed by an organic solvent mixture, as described in detail elsewhere. [167] One of the washed sunflower pollens was attached to a rectangular tipless AFM cantilever (ACST-TL, AppNano Inc., Santa Clara, CA), which has spring constants in the range 3.0-17.9 N/m (nominal 7.8 N/m), by a small amount of epoxy glue using a procedure described in detail elsewhere. [197] The spring constants of the fabricated cantilevers were determined according to the method described by Burnham and Hutter. [168, 169] The approaching velocity was maintained at a small value of 500 nm/s, in order to minimize the viscous resistance to the pollen probes penetrating into the liquid droplet samples. The retraction rates of the probes were manipulated in the range of 0.5-117 μm/s in order to probe both static and hydrodynamic

contributions to capillary adhesion. All force measurements were performed under normal air condition (RH of 35-45%), and the loading forces on the cantilevers were controlled at 500 nN in all experiments.

4.3.5 Droplet Volume Measurement

10 μL of the extracted aqueous phase was deposited on a polystyrene surface (D210-16, Simport, Beloeil, QC, Canada) to make a droplet sample and placed into a sealed quartz cell (100-07-50, ramé-hart Instrument Co., Succasunna, NJ). The relative humidity in the cell was controlled by a salt (calcium chloride) at 15% RH (20° C) for first 12 h and by a supersaturated solution of sodium chloride at 75% RH (20° C) for the next 12 h. The volume of the droplet was measured and recorded every 5 min using a ramé-hart automated goniometer (290-G1, Succasunna, NJ) with DROPimage Advanced software. The volume changes of an aqueous phase droplet with oily phase coat (10 wt%) was also measured using the same procedure by adding an extracted oily phase back onto the aqueous droplet phase.

4.4 Results and Discussion

4.4.1 Presence of Two Phases in Pb-adhesive.

Pb-adhesive droplet samples were prepared as explained in the materials and methods section. The structure of the pb-adhesive droplets was investigated using an optical microscope and confocal Raman spectroscopy. Figure 22 (a) shows an optical reflection-mode image of the droplet on a silicon wafer and indicates that there are two different colored regions in the droplet. A core liquid region, which is bright white at the

center, is surrounded by a distinct dark yellow liquid. To confirm that the color difference (white and yellow) was related to chemical difference between two separate phases and not due solely to thickness differences of the two fluid regions, the Raman spectrum of both regions was obtained using confocal Raman spectroscopy (Figure 22 (b)).

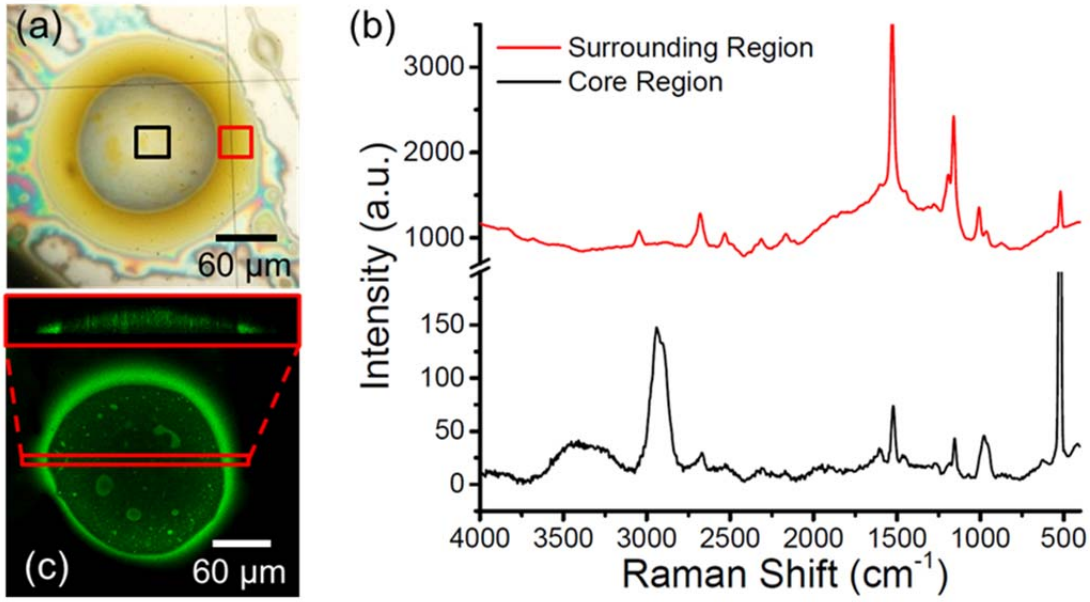

Figure 22 – Two different liquid phases in a pb-adhesive droplet. (a) Optical microscope image of the droplet on a silicon wafer (core region - black box, surrounding region – red box). (b) Confocal Raman spectroscopy spectra of the surrounding (red) and the core (black) regions of the droplet (488 nm laser excitation) (c) Confocal fluorescence microscopy images of the droplet, top view with side view shown in smaller in red box.

Honey bees are known to utilize a mouth secretion to attach pollens to their pollen baskets, and nectar and/or honey (predominantly glucose and fructose dissolved in water) are known as the main components of the bioadhesive. [188] However, there is no prior reported evidence of the presence of a yellow pigmented separate phase, which is observed in Figure 22 (a), in the bioadhesive from bees. We hypothesize that the surrounding yellow region is pollenkitt, a plant-based lipid oil coat found in almost all

entomophilous pollens. [196] The dandelion pollens used to make the pb-adhesive droplets are known to carry pollenkitt on their surface, which can be up to 60 wt% of the pollen. [95] Pollenkitt is a hydrophobic mixture containing mainly saturated and unsaturated lipids, carotenoids, flavonoid, proteins, and carbohydrates. [196] The mixture of flavonoids and carotenoids cause a typical yellow to orange color. [198] The bioadhesive secretion from bees is an aqueous solution, so the oily pollenkitt appears as a separated phase as shown in Figure 22(a). The confocal Raman spectrum of the core (black line) and surrounding (red line) regions in Figure 22 (b) also support this hypothesis. The broadband between 3700 cm^{-1} and 3000 cm^{-1} (assigned to O-H stretching vibrations) and the intense peaks centered around 2,941 and 2,904 cm^{-1} (assigned to C-H stretching vibrations) were only observed in the core region, and these are typically detected in the Raman spectra of honey and sugars dissolved in water. [199] The intense peaks (2669, 1520, 1150, and 1004 cm^{-1}) of the Raman spectrum of the surrounding region are assigned to carotenoids. [200] The Raman peaks assigned to the carotenoids also existed in the Raman spectrum of the aqueous phase (black line in Figure 22 (b)), and they could be caused by a small amount of the oily phase dispersed in the aqueous phase, which is also evident in the microscopy images. The liquid phase structure of the pb-adhesive droplet was investigated using confocal fluorescence microscopy. One of the carotenoids (β-carotene) in pollenkitt is autofluorescent with an excitation wavelength of 488 nm. [198] The top and side view confocal images were taken under 488 nm excitation wavelength (Figure 22 (c)). The confocal image shows that colloidal droplet containing carotenoids are dispersed in the aqueous phase, but the main domain of the

aqueous phase is not fluorescent. On the other hand, the surrounding outer phase is predominantly fluorescent.

4.4.2 Physical Properties of the Two Phases

The aqueous and oily phases were extracted and separated using solvent extraction with toluene and water, as described in materials and methods section. Pollenkitt is a hydrophobic mixture, and low polarity organic solvents were generally utilized for the extraction of pollenkitt in previous studies. [196, 201] Otherwise, the main components in the aqueous phase are glucose and fructose, [184, 195] which are well-known water-soluble polar compounds. It might be possible some polar components from the pollenkitt could dissolve in water and some organic from sugar solution could dissolve in toluene. Therefore, the confocal Raman spectrum of both extracted aqueous and oily phases was obtained and compared to the Raman spectrum of the pb-adhesive droplet in Figure 22 (b), and we don't see any notable component change of both phases after extraction as shown in Figure 23 (e).

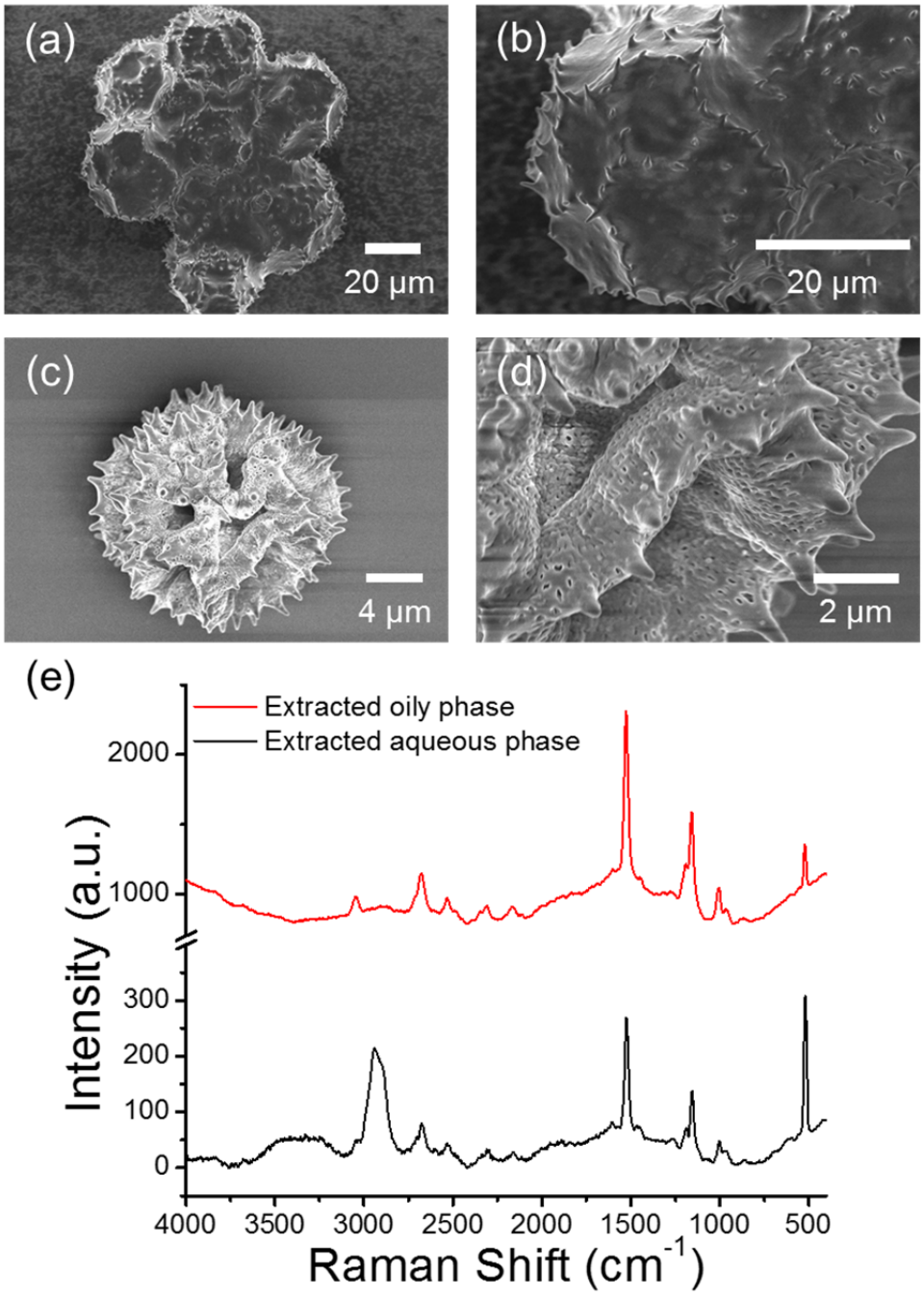

Figure 23 – SEM images of dandelion pollens collected from honey bees, (a) and (b). The pollens are aggregated and coated with liquid pb-adhesive (a mixture of aqueous and oily phases). SEM images of a dandelion pollen after solvent extraction (water and toluene), (c) and (d). The pb-adhesive is not observed after the solvent washing. (e) Confocal Raman spectroscopy spectra of the extracted oily (red) and aqueous (black) phases. (488 nm laser excitation)

The SEM images of bee pollens before (Figure 23 (a) and (b)) and after (Figure 23 (c) and (d)) the solvent extraction indicate that the pb-adhesive on the pollen surface was washed away during the extraction. A quantity of 5.8 g of aqueous phase and 0.6 g of oily phase were extracted from 10 g of bee pollens into water and toluene, respectively, and density and surface tension of each phase are shown in Table 2. as described in materials and methods. The density and surface tension of the aqueous shows a similarity to the physical properties of honey (density in the range of 1.45-1.58 g/ml and surface tension in the range of 54.4-62.8 mN/m), according to a previous study. [202] The density of oily phase is in the range of common vegetable oils, which is 0.919-0.965 g/ml, [203] and it shows a lower surface tension than common vegetable oils (31-39.15 mN/m). [204]

Table 2 – Physical properties of the aqueous and the oily phases in pb-adhesive.

	Solvent	Mass fraction	Density (g/ml)	Surface tension (mN/m)
Aqueous Phase	Water	0.906	1.547	52.5
Oily phase	Toluene	0.094	0.948	22.5

4.4.3 Adhesive Property of the Two Phases

Adhesion of sunflower pollen (*Helianthus annuus*) on the core and surrounding liquid phases was measured using AFM colloidal probe microscopy at 20 °C and 35% RH, as described in material and method section. The pollen attached on a tipless AFM cantilever was brought into contact with either the core or surrounding region of pb-adhesive droplets (Figure 24 (a)), and the pollen was retracted at different rates while the force was recorded as a function of distance. For consistency, only force measurements in regions of similar thickness, in the range of 0.8-1.1 μm, are studied, and the thicknesses

of each point was estimated using the jump-in distance of the approach curves, as described in Chapter 3.

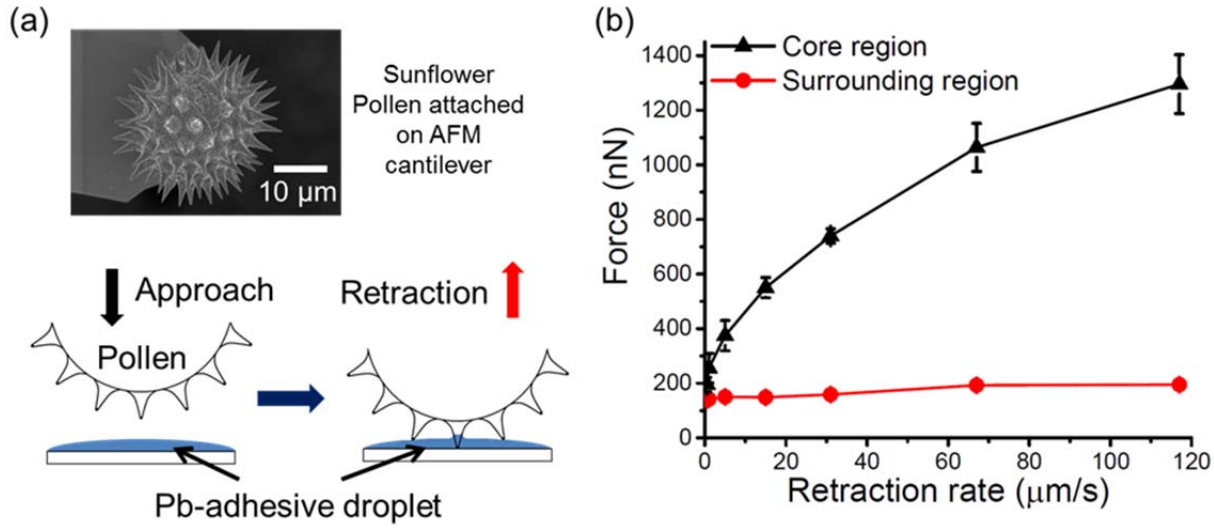

Figure 24 – (a) Schematic of adhesive force measurement using AFM colloidal probe microscopy. (b) Adhesion force versus retraction rate of a sunflower pollen (*Helianthus annuus*) on the core (mainly aqueous phase) and the surrounding (oily phase) liquid regions of a pb-adhesive droplet. The error bars represent 95% C.I.

The measured adhesion on the core region in Figure 24 (b) shows a remarkable rate-dependence when the retraction rate exceeded a critical velocity (5 μm/s). The wet adhesion on the oily phase didn't depend significantly on the retraction rate. The adhesion magnitude generated on the core regions (195 ± 27 nN) was 29% stronger than the adhesion on surrounding regions (139 ± 4nN) at the retraction rate 0.5 μm/s, but the wet adhesion of the core regions was 660% higher than surrounding regions at 67 μm/s and above. In previous chapter (Chapter 1), we showed that there are two main contributions, viscous and capillary forces, to generate wet adhesion, and only viscous force is a rate-dependent adhesion attributed to the contained hydrodynamic component. The rate-dependent wet adhesion on the core region indicates that the aqueous phase of

the pb-adhesive is a much more viscous liquid than the oily phase. The mass fraction of the aqueous phase in the pb-adhesive was more than 9 times larger than the oily phase (Table 2), and wet adhesion on the core regions (mainly aqueous phase) shows a much stronger force magnitude than the surrounding regions. Therefore, we can conclude that the aqueous phase from honey bees is a highly viscous liquid and a main contributor to the adhesive properties of pb-adhesive.

4.4.4 Humidity Dependence of the Aqueous Phase

The pb-adhesive droplets on a silicon wafer were washed with toluene, as described in the material and method section. After the toluene washing, the surrounding region (oily phase) was clearly removed, and no notable shape or size change of the core region (aqueous phase) was observed (Figure 25 (a)). The washed samples were utilized for investigating the wet adhesive properties of the aqueous phase without the oily phase coating. Before the force measurement, the thicknesses of the aqueous phase droplets were measured using the method described in materials and methods. Three aqueous phase droplets (total 15 droplets), each with a thickness in the range 1.5-1.7 μm were chosen for the wet adhesion measurement and were kept at the same relative humidity (15%, 35%, 57%, 75%, and 92% RH) for 24 h prior to measurement.

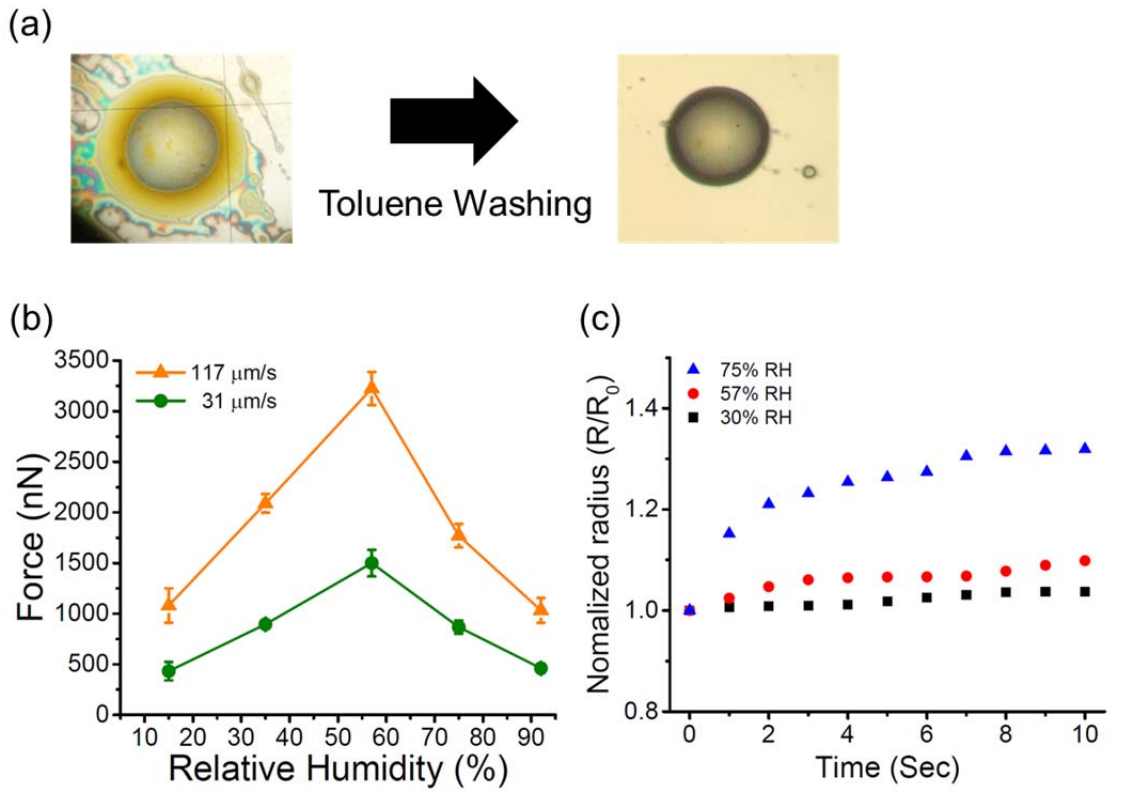

Figure 25 – (a) Optical microscope images of a pb-adhesive droplet on a silicon wafer before and after toluene washing. After the washing, the aqueous phase in the droplet remained, but the oily phase was washed away. (b) Adhesive force of a sunflower pollen on the aqueous phase droplets, stored in different relative humidity levels, at retraction rates of 31 and 117 µm/s. The error bars represent standard error. (c) Normalized spreading radius of the aqueous phase droplets (13 ± 2µL) on a silicon wafer. Before spreading the droplets on the surface, 1mL of three aqueous phase samples was stored in three different humidity levels (30%, 57%, 75% RH) for 3 days. The spreading radius of the droplets was measured at 20°C and at 45% RH.

In Figure 25 (b), more than 60% adhesion loss of the aqueous phase occurred when the relative humidity was increased from 57 to 92% RH. In addition, unexpected adhesion loss was observed when transitioning to low relative humidity (15% and 35% RH). The force variation of a water absorbing adhesive at different relative humidity levels was explained by the counteractive relationship of the viscous dissipation and the spreading rate of the viscous adhesive, according to the study of Amarpuri et al. (2015).

[193] Glucose and fructose, which are the main components in the aqueous phase, are well-known water absorbing materials. When the droplet samples were stored at high relative humidity (75% and 92% RH), the aqueous phase, originally a viscous adhesive, became a less viscous liquid by absorbing water. As we showed in Chapter 1, the magnitude of viscous force is decreased with the reduction of liquid viscosity. Thus, the viscous dissipation of the aqueous phase meniscus on the sunflower pollen could be reduced at the highest relative humidity. The wet adhesion at low relative humidity (15% and 35% RH) was also decreased even though the viscosity of the samples was expected to be increased. The adhesion loss can be attributed to the reduced spreading rate of a liquid adhesive when it has excessively high viscosity. The spreading rates of the aqueous phase reported in Figure 25 (c) show a dramatic drop in the spreading rate of the samples stored at low relative humidity. All adhesion AFM measurements were performed with the same approach rate of pollen to the droplet (0.5 μm/s), so the estimated contact period during the approach step was estimated to be around 3 s. An increasingly smaller contact area will be created as viscosity increases as humidity drops.

We hypothesized that the aqueous phase could be diluted by absorbing moisture from humid air or concentrated by evaporating water molecules to dry air, so the water composition changes of the aqueous phase under different humidity-environment were investigated. The aqueous phase was initially stored at 45 ± 5% RH for 2-3 days.

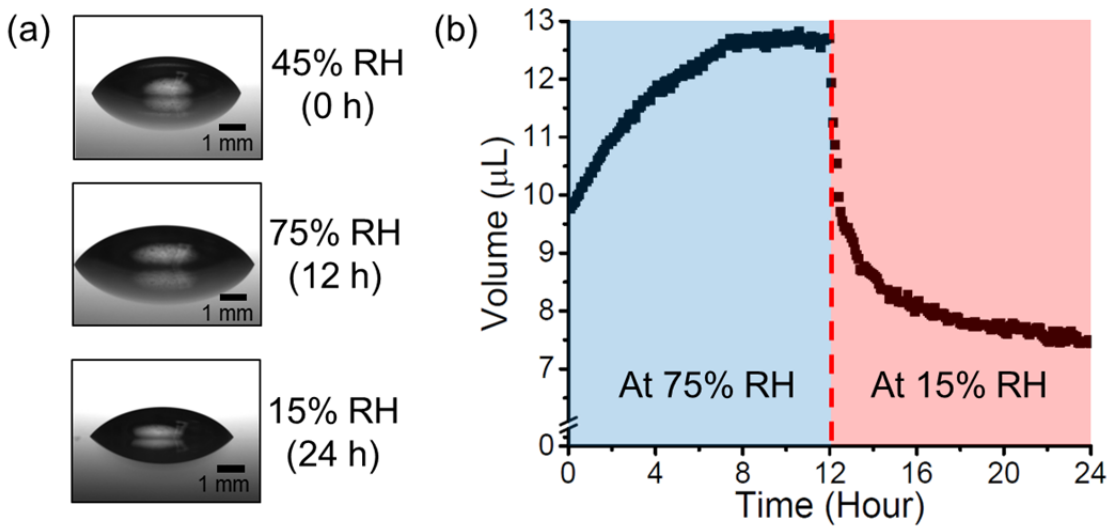

Figure 26 – (a) Images of the aqueous phase droplet on a polystyrene surface, stored at 75% RH for the first 12 h and at 15% RH for the next 12 h. The droplet was initially saturated at 45% RH for 2-3 days. (b) Droplet volume as a function of time.

As shown in Figure 26 (a) and (b), the volume of the aqueous phase was increased by 30% from the original volume when it was exposed to a high humidity environment (75% RH) for 12 h. The enhanced volume was dramatically decreased by 24 %, compared to the initial droplet volume when the environmental humidity decreased to 15% RH for 12 h. This result indicates that the water composition of the aqueous phase is strongly dependent on the relative humidity of surrounding air, and supports the prior hypothesis that adhesive property changes of the aqueous phase are attributed to the water-uptake or -loss.

4.4.5 Humidity-dependent Viscosity

The viscosity of the aqueous phase stored at different relative humidity levels was measured to understand the influence of the water-uptake or -loss on the physical property of the aqueous phase as described in materials and method section.

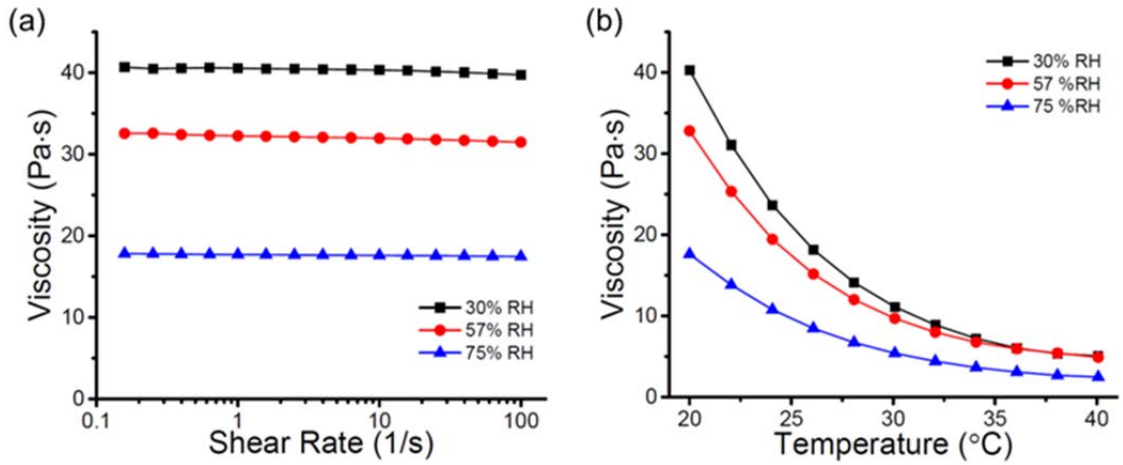

Figure 27 – Viscosity of the aqueous phase samples stored at different relative humidity levels (30%, 57%, and 75% RH for 3 days) as a function of (a) shear rate at 20° C and (b) temperature at 10 s^{-1} shear rate.

Figure 27 (a) and (b) show that the viscosity of the aqueous phase is strongly dependent on the relative humidity. The viscosity was increased from 32 to 40 Pa·s athumidity (30% RH), but viscosity was reduced to 18 Pa·s at high humidity (75% RH), compared to the intermediate humidity (57% RH). A notable volume change of the samples was observed after the saturation at different humidity levels for three days, and the change of the water content of the samples led a large impact upon the sample viscosity. The viscosity of the aqueous phase shows Newtonian fluid behavior in Figure 27 (a), and the viscosity of the samples was dependent on the experimental temperature (Figure 27 (b)). A previous study reported that these (Newtonian fluid and temperature-dependent viscosity) features are common rheological properties of honey and sugar solutions. [205]

4.4.6 Influence of the Viscosity Changes on the Wet Adhesive Mechanism of the Aqueous Phase

The previous section shows that the viscosity of the aqueous phase is strongly dependent on environmental humidity. In this section, we discuss how the changed viscosity affects the wet adhesive mechanism of the aqueous phase. To minimize the influence of geometrical factors associated with pollen and droplet, we designed an adhesion test based on the separation of two parallel flat surfaces connected by the aqueous phase. A droplet of 15.8 ± 0.2 µl of the aqueous phase was placed on a glass slide, and a liquid bridge of the aqueous phase was formed in between the two flat glass surfaces as shown in Figure 28 (a). Multiple capillary bridge samples were prepared in the same manner and stored in different relative humidity chambers (30 %, 57%, and 90% RH) for 24 h before the adhesion measurement. The dimensions of the capillary bridges were measured using a goniometer immediately before the test. A customized high-throughput mechanical characterization apparatus (HT-MECH) was used to measure the adhesion magnitude of the liquid bridges with separation rates in the range of 5 to 20 mm/s (Figure 28 (b)). The details of the customized equipment were described previously [206]. Figure 28 (d) shows the measured force-time curves using the HT-MECH.

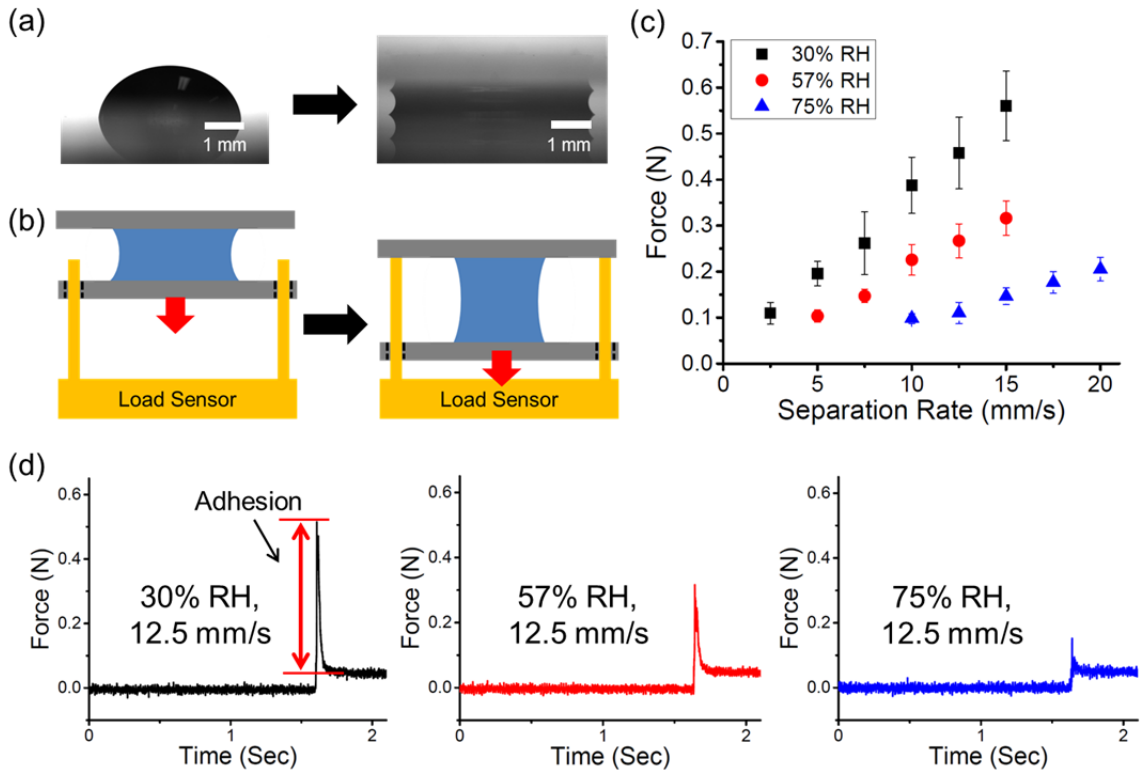

Figure 28 – (a) Image of the pb-adhesive aqueous phase liquid bridge between two glass slides. (b) Schematic illustration of the wet adhesion measurement. (c) Adhesion force due to the liquid bridge as a function of separation rate and humidity. (d) HT-MECH force-time curves of the liquid bridges of the aqueous phase stored in different relative humidity levels with separation rates at 12.5 mm/s.

As shown in Figure 28 (c), we observed that the adhesive force magnitude of the aqueous phase was very sensitive to the relative humidity, and the adhesion shows a nearly linear relationship to the separation rate. Wet adhesion models for the separation of two parallel flat surfaces [207] were used to understand the humidity dependence and the linear relationship. It is well-known that capillary and viscous forces are two main contributors for the adhesion of thin liquid bridges, and the total adhesion of liquid bridges can be estimated by the summation of these forces. The contribution of these components can be determined by considering the meniscus curvatures, dynamics and viscosity of liquid bridges. [207]

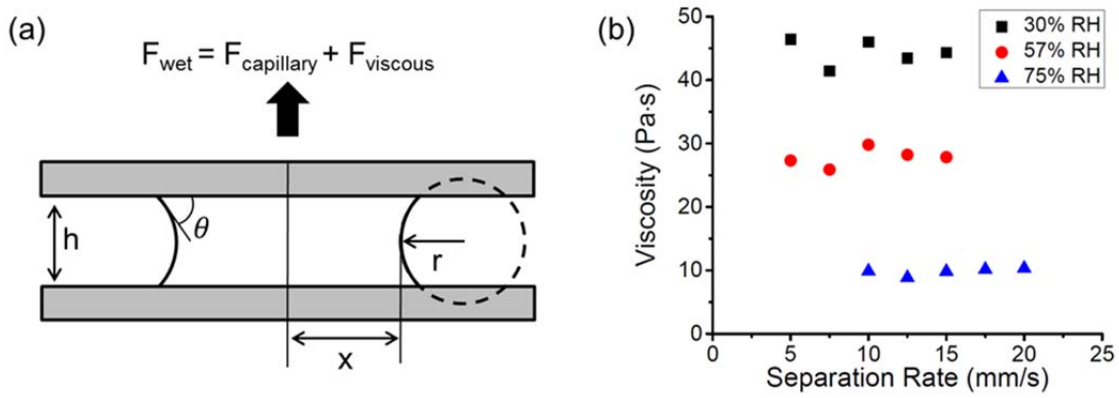

Figure 29 – (a) Schematic of the separation of two parallel flat surfaces joined by a liquid bridge. (b) Viscosity of the aqueous phase stored at different humidities as estimated by the wet adhesion model (equation (37)) by using the measured liquid-bridge forces (Figure 28(c)).

The capillary force is caused by a liquid bridge between the two separated surfaces, and the curvature of the liquid meniscus is characterized by two radii which are the azimuthal radius (x) and the meridional radius (r), indicated in Figure 29 (a). The total capillary force can be defined as the summation of the surface tension and Laplace pressure contribution [21] as shown in equation (34), and the physical configurations of the wet adhesive model are shown schematically in Figure 29 (a).

$$F_{Capillary} = 2\pi\gamma x \sin\theta + \Delta P \pi x^2, \tag{34}$$

where γ is the surface tension of the liquid bridge, θ is contact angle between the liquid bridge and the flat surfaces, and ΔP is Laplace pressure, estimated by the Young-Laplace equation:

$$\Delta P = \gamma\left(\frac{1}{x} + \frac{1}{r}\right). \tag{35}$$

The surface tension (γ = 52.5 ± 0.1 N/m at 57% RH) of the aqueous phase was measured using the pendant drop method. The azimuthal radius (x), the meridional radius (r), the height (h), and contact angles (θ) of the liquid bridges were determined from optical images, taken immediately before the force measurement, as shown in Table 3.

Table 3 – Dimensions of the liquid bridge of the aqueous phase stored in different humidity levels.

	Azimuthal radius (x, mm),	Meridional radius (r, mm)	Height (h, mm)	Contact angle (θ, °)	Estimated capillary force (mN)
30% RH	2.68 ± 0.08	0.34 ± 0.02	0.66 ± 0.01	26.2 ± 2.3	4.34
57% RH	2.60 ± 0.07	0.36 ± 0.01	0.66 ± 0.01	36.7 ± 3.1	4.00
75% RH	2.81 ± 0.07	0.34 ± 0.01	0.67 ± 0.03	36.3 ± 4.2	4.87

Based on the measured configurations, the static capillary forces of the liquid bridges were estimated by equation (34) as shown in Table 3. The estimated static capillary forces were two orders of magnitude lower than the measured adhesion in Figure 28 (c). Even if one uses the pure water surface tension (72.8 N/m), the estimated static capillary contribution is much smaller than the measured forces in Figure 28 (c). These results indicate that the viscous force governs the wet adhesion magnitude of the aqueous phase, a common phenomenon when the liquid bridge is a highly viscous liquid. [52]

The viscous force is an effect of the hydrodynamic response of the liquid bridge, resisting the separation of the two flat surfaces. The viscous force of a Newtonian fluid for a non-slip boundary condition can be predicted by the Reynolds lubrication equation. The average pressure difference, caused by the hydrodynamic response, between the liquid bridge and ambient air during the separation was estimated previously by Cai and Bhushan (2007) [207]:

$$\Delta P_{avg} = \frac{3\eta}{2h^3} x^2 \frac{\partial h}{\partial t}, \tag{36}$$

where η is the viscosity of the liquid, and $\partial h/\partial t$ indicates the separation rate. Therefore, the viscous force of the liquid bridge, having a meniscus area of πx^2, at a constant separation rate $\dot{h}$ can be approximated as

$$F_{Viscous} = \frac{3\eta\pi}{2h^3} x^4 \dot{h} \tag{37}$$

The aqueous phase shows a Newtonian fluid behavior as shown in Figure 27 (a), so the viscous force and the separation rate ($\dot{h}$) should have a linear relationship with the slope of $3\eta\pi x^4/(2h^3)$ as shown in equation (36). This linear relationship was observed from the measured adhesion (Figure 28 (c)). In Figure 29 (b), the viscosity of the aqueous phase samples was estimated by the measured forces in Figure 28 (c) and equation (37)). This result, taken with the viscosity and water absorption data presented previously, indicates that the viscosity changes induced by changes in environmental humidity were the main cause of the humidity-dependent adhesion of the aqueous phase. The viscosity estimated from the adhesion results (Figure 27 (b)) agrees reasonably with the viscosity measured with by a rheometer in Figure 27 (a). Quantitative differences in the rheologically-determined and adhesion-determined viscosity values were possibly related to the different volumes of the samples and water saturation in the different instruments. The volumes of the aqueous phase used to measure the forces (15.8 μL, saturated for 24 h) were much less than the volume used for the rheometer tests (1 mL, saturated for 3 days).

4.4.7 Oily Phase as a Semi-permeable Membrane

In the previous sections, we discussed the adhesive property of the aqueous phase and the influence of humidity on its functionality, but the role of the oily phase (pollenkitt) was not discussed. As shown in Figure 24 (b), the oily phase contributed very little to the adhesive property of the pb-adhesive. Interestingly, pollens from some plant species are known to use the pollenkitt to slow down water loss because the viability of pollen is quickly decreased with dehydration. [196] Thin films of the oily phase spread over the aqueous phase could also serve to prevent excessive water uptake under elevated humidity and water loss under reduced humidity, helping to mitigate the effects of humidity on the pb-adhesive. However, quantitatively studies of the ability of pollenkitt to inhibit moisture transport have not been reported in the literature studied yet.

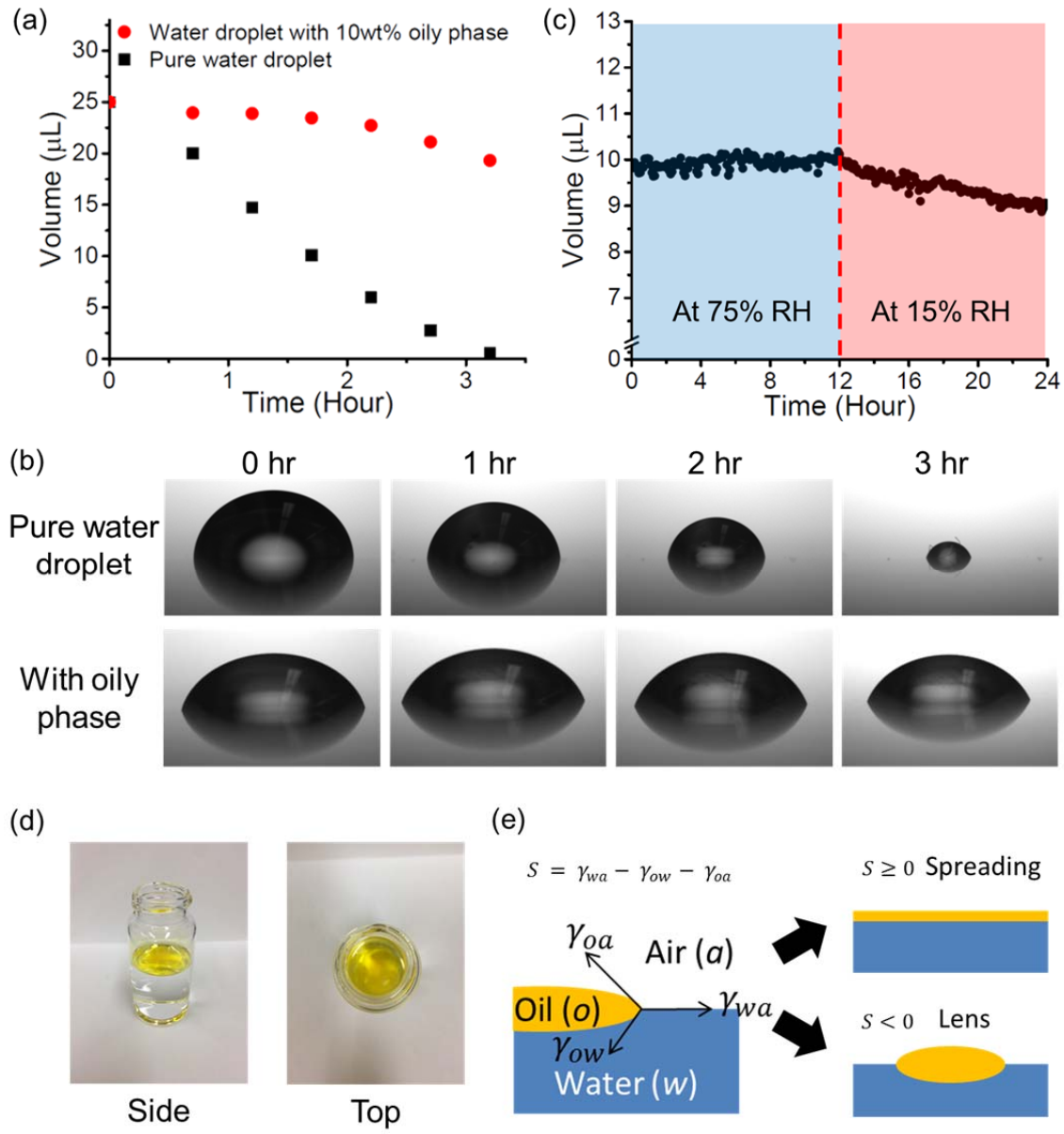

Figure 30 – (a) Volume of a pure water droplet (black squares) and a water droplet with 10 wt% of the oily phase coat (red circles) at 15 %RH. (b) Images of the droplets in Figure 30 (a). (c) Volume changes of the aqueous phase droplet with oily phase coat stored at 75 %RH for the first 12 hr, and at 15 %RH for the next 12 hr. (d) Images of the oily phase dropped on a water surface. (e) Spreading of oil on a water-air interface, determined by the spreading coefficient, *S*. γ is the interfacial tension between the two phases designated by subscripts w (water), o (oil), and a (air).

In Figure 30 (a) and (b), we investigated the volume changes of a water droplet coated with the extracted oily phase under low humidity (15% RH) and the results were compared to a pure water droplet. A 25ml uncoated water droplet and a water droplet coated with a quantity of pb-adhesive oil extract equal to 10 wt% (the mass fraction of oily phase in the pb-adhesive) of the extracted oily phase from the bee pollens were kept at 15% RH (20° C), and the volume changes of the droplets were measured every 40 minutes). The pure water droplet was completely evaporated after 3.2 hr, but the volume of the droplet with the oil coat was reduced by only 20% of the original volume for the same time period. To confirm the wetting behavior of the oily phase placed on the water and air interface, a single drop of the oily phase (5 μL) was placed on the water (10 ml) and air interface as shown in Figure 30 (d). A thin oil layer was observed (Figure 30 (e)), and it indicates that the spreading coefficient, (S) in Figure 30 (f), is a positive number, which is complete wetting. Therefore, we can conclude that the oily phase (pollenkitt) coat covered the interface between the water droplet and dry air. The oily phase also hindered water uptake from the humid air when it was coating on the water absorbing adhesive (aqueous phase) from honey bees. The aqueous phase droplet with the oily phase coating (Figure 30 (c)) was significantly less humidity-dependent compared to the droplet without the pollenkitt oil in Figure 26 (b). Therefore, we can conclude that the pollenkitt coat works as a semi-permeable membrane to inhibit water transport.

4.4.8 Humidity-stabilized Adhesive with Oily Phase Coat

We have shown that the adhesion loss of the aqueous phase was attributed to the water uptake or loss of the bio-adhesive at high or low humidity. Consequently, if the water loss or gain is slowed of the aqueous phase by the pollenkitt oily phase, the adhesive's sensitivity to changes in humidity can be lessened. We measured the adhesion of a sunflower pollen on the pb-adhesive droplets stored at different relative humidity levels to confirm the stabilizing ability of pollenkitt on the wet adhesion. Before the force measurement, the thicknesses of the pb-adhesive droplets were measured using an AFM. The adhesion of the pollen was measured on the total 12 different aqueous phase droplets stored in 4 different relative humidity chambers (each 3 droplets stored at15%, 35%, 57%, and 75% RH), and the measured thicknesses were in the range of 1.1-1.2 μm. The procedure of adhesion measurement was the same method used for the study of the toluene-washed aqueous phase in Figure 25 (b).

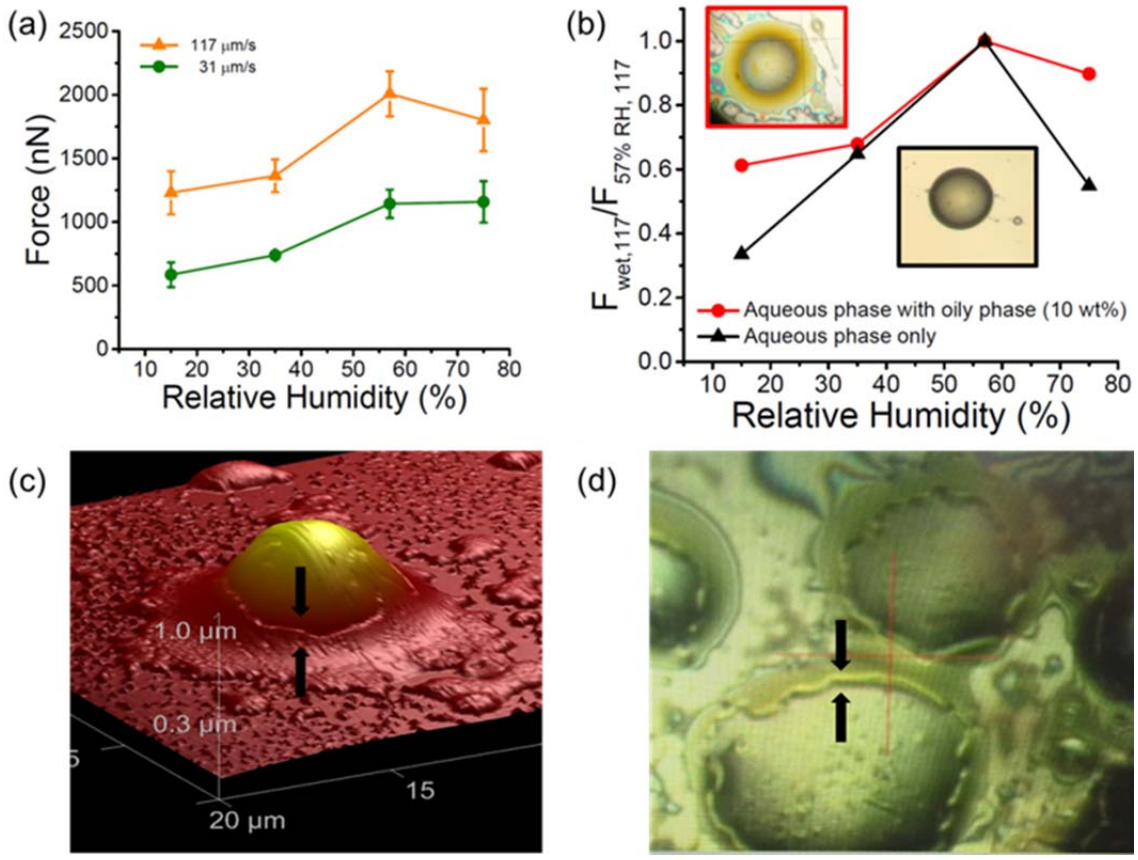

Figure 31 – (a) Adhesive force of a sunflower pollen on pb-adhesive droplets (the aqueous phase with the oily phase coat), stored in different relative humidity levels, with retraction rates at 31 and 117 μm/s. The error bars represent standard error. (b) Normalized adhesion of the aqueous phase droplet with and without oily phase coat by the adhesion of 57% RH sample. (c) AFM and (d) optical microscope images of the pb-adhesive droplets stored in 92% RH for 24 hr. The aqueous phase directly contacts to the humid air due to the rupture of the oily phase coat.

The aqueous phase coated with oily phase shows a strong adhesion at 57% RH (Figure 31 (a)), like the adhesion of the toluene-washed aqueous phase in Figure 25 (b), but the adhesion loss was relieved at low (15% RH) and the high (75% RH) relative humidity, compared to the case of the washed phase in Figure 25 (b). Figure 31 (b) shows the ratio of the wet adhesion at different relative humidity levels and the adhesion at 57% RH with a retraction rate of 117μm/s. The adhesion loss of the samples with the oily phase was only half of the reduction of the aqueous-only phase at both low (15%) and

high (75%) relative humidity. The wet adhesion of the droplet samples with the oily phase coat at 92% RH was not measured due to the rupture of the coat, which led a direct contact between humid air and the aqueous phase as shown in Figure 31 (c) and (d). A triple phase boundary (air-aqueous phase-oily phase) was observed at 92% RH, and the water content of the aqueous phase was not conserved.

4.5 Conclusion

This study has revealed for the first time the presence of two immiscible liquid phases in the bio-adhesive (called 'pb-adhesive' in this paper) of the pollen basket of honey bees. In previous studies, bee mouth secretion was only recognized as a sugar-based aqueous phase bioadhesive to hold pollens on their pollen baskets. We have demonstrated the presence and function of the oily phase (pollenkitt) from pollens in the pb-adhesive. The oily phase spreads on the aqueous phase and significantly relieves the influence of environmental humidity on the aqueous phase water content. The adhesion of the aqueous phase without the oily phase was reduced to under half (low RH) or near half (high RH) of the maximum adhesion observed at intermediate humidity (57 % RH). However, the magnitude of the adhesion loss decreased by about half of the original reduction when the adhesive samples coated by the oily phase. The oily phase served to prevent excessive water absorption under elevated humidity and excessive drying under reduced humidity, compared to intermediate humidity values. This action stabilized the viscosity of the aqueous phase during humidity changes, thereby stabilizing the hydrodynamic adhesion contributed by the aqueous phase. This result provides inspiration for the future development of novel humidity-stabilized adhesive materials.

CHAPTER 5. CONCLUSIONS AND RECOMMENDATIONS FOR FUTURE WORK

5.1 Summary and Conclusion

5.1.1 Simultaneously Controlled Short and Long Range Forces of Pollen-shaped Microparticles

I have found the way to manipulate the adhesive force magnitude and range of microparticle. I utilized fabricated $CoFe_2O_4$ pollen replicas, which have a strong magnetic moment, to apply long-range magnetic force on the pollen-shaped microparticle. The remnant and saturation magnetic moment were enhanced with the increase of the metal crystal size, and the magnetic force magnitude and range were successfully manipulated via controlling the crystal size. The controlled crystal size also affected the magnitude of vdW interaction (short-range force). I found a reproducible non-monotonic relationship was attributed to the counteracting effects of crystal size and the number of crystals within the vdW interaction range, and the counteracting effects were validated via computational simulation based the Hamaker approach. In previous studies [208, 209], the magnetic force of pollen-shaped microparticles was manipulated via controlling the total volume of magnetic materials. However, these approaches were not able to control the both short and long range forces simultaneously. This study can supply information for the future development of water purification, particle separations, particulate removal from exhaust streams, targeted drug delivery, catalysis, composite processing, and assembly of hierarchical structures.

5.1.2 Influence of Surface Morphology on Wet Adhesion of Microparticles, and Bio-adhesive with Sensitive Hydrodynamic Response to Retraction-rates

I have studied the influence of the surface morphology of pollens on the wet adhesive mechanism. The adhesion magnitude of the microparticles on pollenkitt films was strongly dependent on the surface structure of the particles. Especially, a correlation between the structural effects and the thickness of liquid adhesive (pollenkitt) films was investigated. Ragweed pollens with a short length of spines showed stronger wet adhesion on thick adhesive film (thicker than the length of the spines) than sunflower pollens, but sunflower pollens with large spine tip radius showed stronger wet adhesion when the film thickness was in the range of tip radius. A rate-dependent adhesive property was observed from wet adhesion of the pollens on both thin and thick liquid films. The wet adhesion of pollenkitt showed a more sensitive hydrodynamic response to retraction rates (at 5 μm/s and above), which is lower threshold, compared with the other known bio-adhesive systems such as spider webs with adhesive glue (at 10 μm/s and above) [148], gecko setae (at 20 μm/s and above) [174], and stick insect's pads (above 100 μm/s) [88]. This special feature is due to the relatively high viscosity (above 1 Pa·s) at low shear rate. The viscosity of the pollenkitt was studied by using a viscous force model for sphere-plane geometries and cone-plane viscometer. These sensitivities of dynamics to geometry suggest new approaches to tuning particle adhesion and detachment in applications ranging from target drug delivery to reversible adhesives.

5.1.3 Novel Strategy to Stabilize the Humidity-dependence of Water-based Adhesives

I have studied the adhesive property of the liquid adhesive in bee-pollens. In previous studies [187, 188], only a sugary and water-based liquid adhesive from bees was reported as the component of the bio-adhesive. However, I revealed for the first time the presence of two immiscible liquid phases in the bio-adhesive. One liquid is an aqueous phase adhesive from bees as reported, and the adhesive properties of the aqueous phase showed a dramatic adhesion loss, attributed to moisture content change, under dry and humid air condition. The other liquid is an oily phase (pollenkitt) from the collected pollens. The study of the liquid phase structure showed that the oily phase spread over the aqueous phases. The reduced volume changes of aqueous phase droplet under relative humidity changes indicate that the oily phase coat serves as a barrier that tempers the effects water transport under high or low humidity conditions. With the oily phase coat, the adhesion loss of the aqueous phase under humid and dry environments was reduced notably. Compared to the other known bio-adhesives systems [148, 193], the bee-pollen adhesive showed more active tuning strategies to preserve the adhesive property under humidity changes via having a multiphase liquid structure. This result provides inspiration for the future development of novel humidity-stabilized adhesive materials.

5.2 Recommendations for Future Work (Bio-inspired Water-harvesting System)

5.2.1 Water Droplet Motion Observed from Pb-adhesive Droplet Samples in Extremely Humid Environment

Water droplet motion was observed when the multiphase adhesive (named, pb-adhesive in Chapter 4) droplet samples from bee pollens (discussed in Chapter 4) were placed in extremely high relative humidity (≈ 100% RH). The supporting material of droplets was a piranha-etched silicon wafer, which was a hydrophilic surface, and small water droplets were spontaneously growing on the open area of the wafer surface as shown in Figure 32 (a) (0-2 sec).

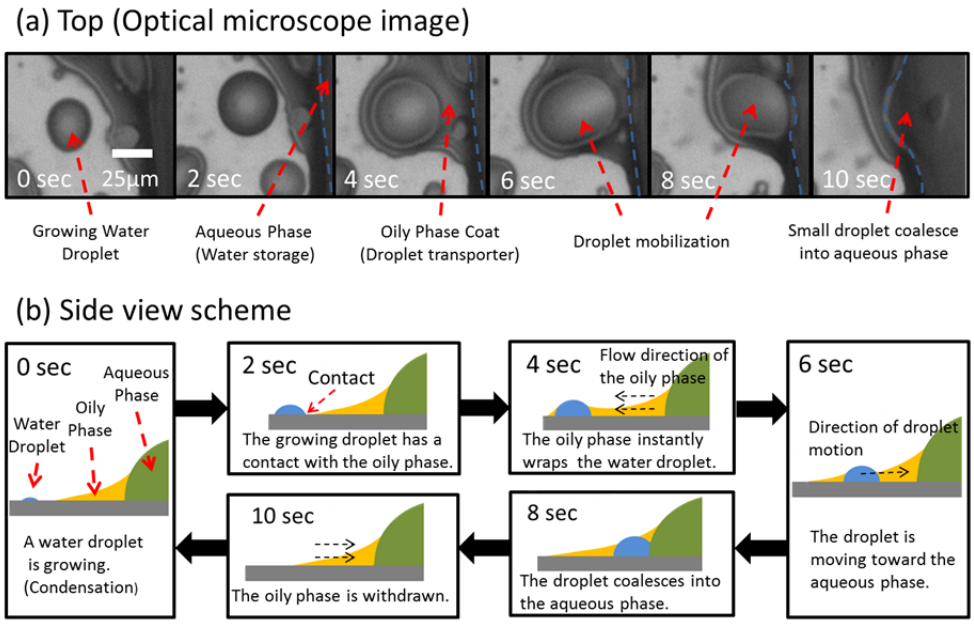

Figure 32 – Pb-adhesive droplet sample (discussed in Chapter 4) in extremely high relative humidity. (a) Observation (optical microscope images) of water droplet motion. (b) Schemes demonstrate the droplet motion.

The liquid structure of pb-adhesive droplets on a silicon wafer was discussed in Chapter 4. The droplets have a core aqueous phase region, and the core region is surrounded by an oily phase. The water droplet motion was initiated when the growing water droplet (condensation) had a contact with the boundary of the oily phase as shown in Figure 32 (a) and (b) (4-6 sec). Interestingly, this droplet motion occurred spontaneously and repeatedly. (Figure 32 (a) and (b) (8-10 sec))

5.2.2 Addressed Scientific Questions and Suggested Answers

Two major scientific questions were addressed in this phenomena: i) what types of forces are associated with the droplet motion, ii) how are the forces related to the interfacial properties of the four phases (water, oil, air, and solid surface)? Clear answers to the questions are not able to give at this moment, but we propose possible answers in here, based on other related studies, and suggest future works for finding the answers.

In a previous study by David Hu and John Bush in 2005, water-walking insects showed an interesting strategy to climb the slippery slopes of the menisci, the border of the water's edge, when they moved from the water surface to land. [210] The previous study reported that the insects generate capillary forces, attributed to the deformed the water surface, to overcome gravitational force for their uphill motion as shown in Figure 33 (a). The physical mechanism of the insects' motion shows a similarity to the lateral capillary forces between two immersed (or floating) particles. In the previous studies of the lateral capillary forces [211–213], it was suggested that two positive (or two negative) menisci attract one another, but a positive meniscus repels a negative meniscus as shown in Figure 33 (b). This mechanism explains the reason why the climbing motion of the

larva in Figure 33 (a) was initiated by arching its back. Meniscus curvature surrounding the larva became more positive after the bending posture, so the capillary attraction between the border of the water's edge and the larva became stronger. In the case of the water droplet motion system, lateral capillary forces can be a driving force to move the small water droplet when the menisci surrounding the aqueous phase and water droplet are positive. Therefore, the shape of the menisci should be studied in the future.

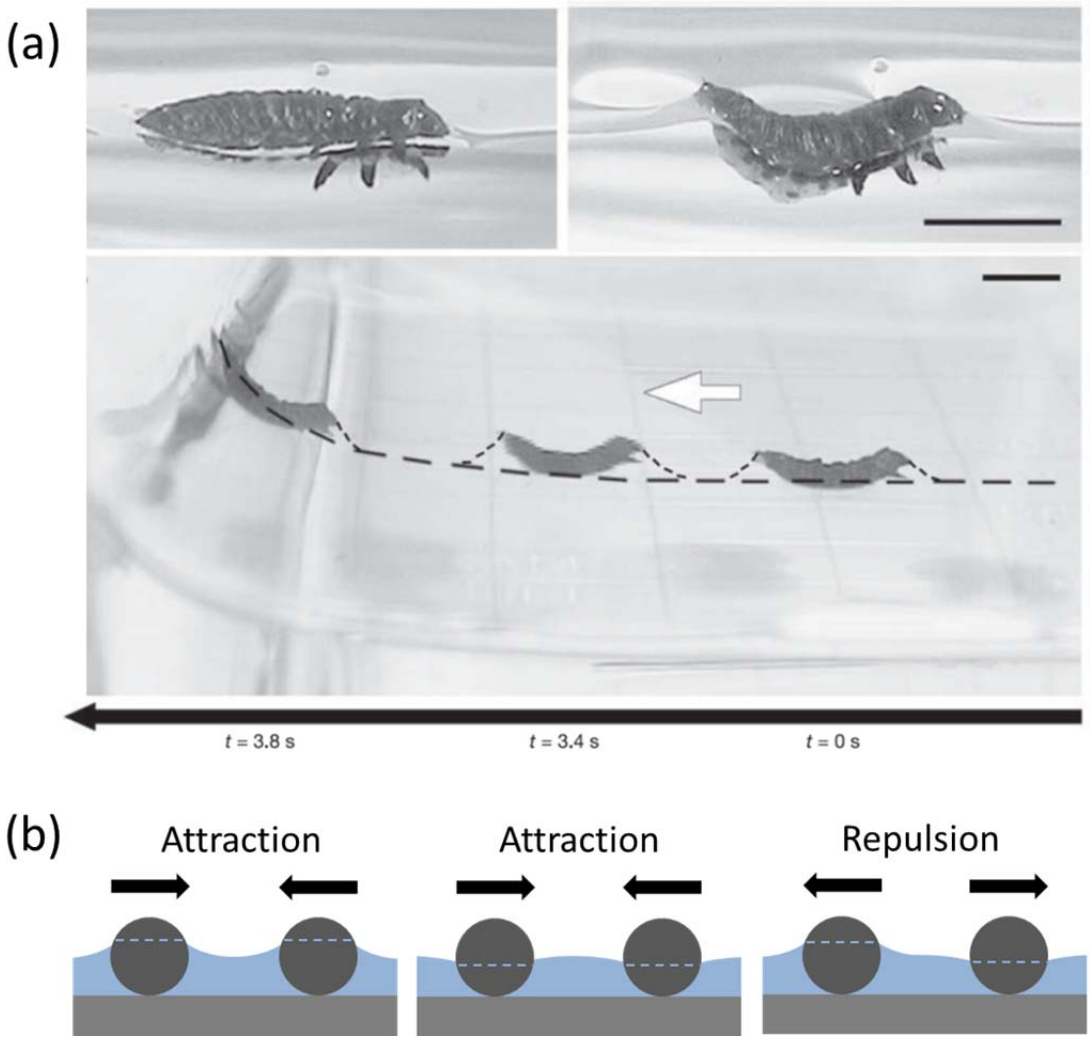

Figure 33 – (a) Mesniscus climbing by the larva of the waterlily leaf beetle. The aching posture generates a positive meniscus surrounding the larva. Scale bar = 1 mm. Reproduced with permission from [210] **(b) Schemes demonstrate the direction of lateral capillary forces. Two positive (or negative) menisci attract one another, but a positive meniscus repels a negative meniscus.** [211–213]

In the small water droplet motion, the interaction between the droplet and the solid surface can work as a resistance to the droplet motion. Advancing and receding contact angles are formed when a liquid droplet is moving on a solid surface because of the solid-liquid interaction. Previous studies of water droplet motion on solid surfaces suggest that contact angle hysteresis works as a resistance to the droplet motion [214, 215], and the magnitude of the resistance is proportional to the difference between advancing and receding contact angles. In the future studies of this bio-inspired droplet harvesting system, measuring the advancing and receding contact angles of the small water droplet is suggested for understanding the influence of the resistance on the droplet motion.

The magnitude of the driving force and resistance of the droplet motion system can be controlled by the interfacial properties of the 4 phases (water, oil, air, and solid surface). With the same volumes of water and oil phases, lateral capillary attraction is stronger when the oil phase completely coats the water-air interface, compared to the partially coated interface, as shown in Figure 34 (a). The criterion for complete coating is given by the spreading coefficient ($S_{ow(a)}$),

$$S_{ow(a)} = \gamma_{wa} - \gamma_{wo} - \gamma_{oa}, \tag{38}$$

where γ is the interfacial tension between the two phases designated by subscripts w (water), o (oil), s (solid surface), and a (air). [216–218] The positive value of $S_{ow(a)}$ implies a complete wetting, whereas the negative value of $S_{ow(a)}$ implies a partial wetting. The resistance of the droplet motion can be minimized or neglected when the oil phase fills underneath the water droplet as shown in Figure 34 (b). The criterion for floating

droplet in Figure 34 (b) is given by the spreading coefficient, $S_{os(w)} = \gamma_{sw} - \gamma_{so} - \gamma_{ow}$. [216–218] The positive value of $S_{ow(a)}$ implies no interaction between the water droplet and solid surface.

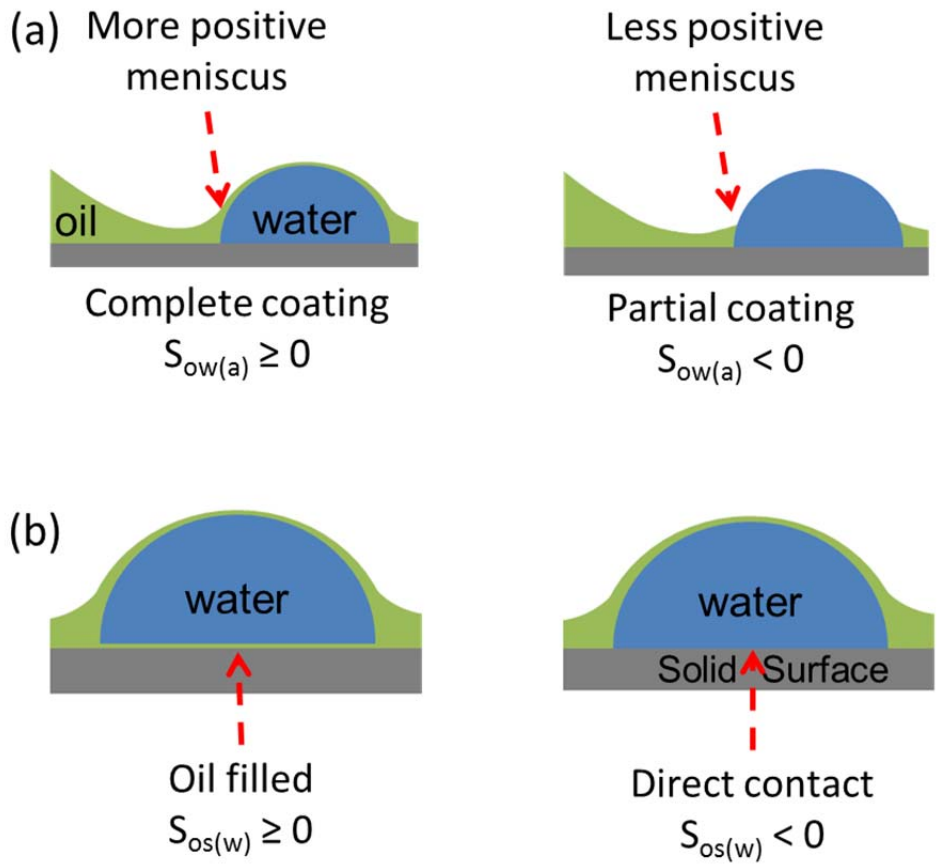

Figure 34 – Schematic illustrations show the relationship between (a) the surface coefficient, $S_{ow(a)}$, and the configuration of the oil meniscus surrounding water droplet, (b) the surface coefficient, $S_{os(w)}$, and the wetting configuration underneath the water droplet.

5.2.3 Bio-mimicry and Suggestion for Future Works

A simple experiment was designed to mimic the water droplet motion of the pb-adhesive as shown in Figure 35 (a). The added small water droplet shows a similar motion as to the original system as shown in Figure 35 (b). (The motion of the water

large droplet was also expected, but it was hard to be recognized.) For this bio-mimic system, oleic acid and polystyrene were used as an oil phase and as a solid surface. The spreading coefficient of the oil-water-air interface ($S_{ow(a)}$) was estimated as 18.7 mN/m by equation (38). For this estimation, the γ_{wa} was measured using pendant drop method after the water was saturated in oleic acid for 3 days. The γ_{wo} (32.5 mN/m) and γ_{oa} (15.7 mN/m) values were obtained from a literature. [219] The perfect oil coating on the water droplets (positive value of $S_{ow(a)}$) is expected to create two positive menisci surrounding the large and small water droplets, so lateral capillary forces are a driving force for the attraction. The presence of the resistance force (interaction between the water droplets and polystyrene surface) of the droplet motion in this bio-mimic system was investigated by the suggested experiment in Figure 35 (c). The droplet motion was observed even with a small tilting (< 0.5°) of the polystyrene surface. There was no (or negligible) interaction between the water droplet and the solid surface, and it indicates that the spreading coefficient, $S_{os(w)}$, might be a positive value. In this biomimetic system, we show that the water droplet motion can be reproducible with commercial materials (oleic acid, and polystyrene). In the future, control experiments with different materials (different oils and solid surfaces) with various interfacial properties will provide inspiration for the future development of designing sustainable water-harvesting systems.

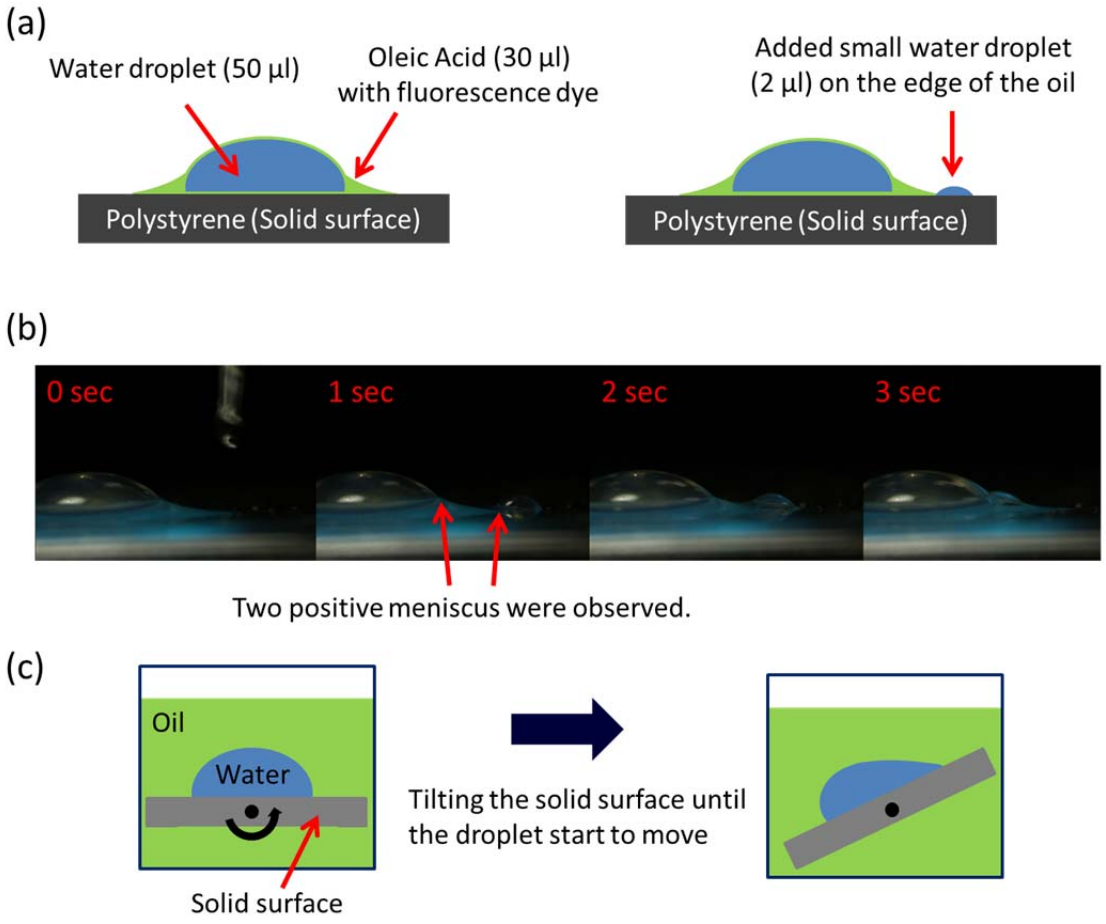

Figure 35 – (a) Schematic illustrations of the bio-mimic water droplet motion system. (b) Observation of the water droplet motion. (c) Schematic illustrations of the contact angle hysteresis test.

REFERENCES

1. Shirtcliffe NJ, McHale G, Atherton S, Newton MI (2010) An introduction to superhydrophobicity. Adv Colloid Interface Sci 161:124–138. doi: 10.1016/j.cis.2009.11.001

2. Lv J, Song Y, Jiang L, Wang J (2014) Bio-inspired strategies for anti-icing. ACS Nano 8:3152–3169. doi: 10.1021/nn406522n

3. Lee A, Moon MW, Lim H, et al (2012) Water harvest via dewing. Langmuir 28:10183–10191. doi: 10.1021/la3013987

4. Park K-C, Kim P, Grinthal A, et al (2016) Condensation on slippery asymmetric bumps. Nature 531:78–82. doi: 10.1038/nature16956

5. Gu ZZ, Uetsuka H, Takahashi K, et al (2003) Structural color and the lotus effect. Angew Chemie - Int Ed 42:894–897. doi: 10.1002/anie.200390235

6. Bechert DW, Bruse M, Hage W, et al (1997) Experiments on drag-reducing surfaces and their optimization with an adjustable geometry. J Fluid Mech 338:59–87. doi: 10.1017/S0022112096004673

7. Geim a K, Dubonos S V, Grigorieva I V, et al (2003) Microfabricated adhesive mimicking gecko foot-hair. Nat Mater 2:461–463. doi: 10.1038/nmat917

8. Hao P, Yao Z, Zhang X (2011) Study of dynamic hydrophobicity of micro-structured hydrophobic surfaces and lotus leaves. Sci China Physics, Mech Astron 54:675–682. doi: 10.1007/s11433-011-4269-1

9. Barthlott W, Neinhuis C (1997) Purity of the sacred lotus, or escape from contamination in biological surfaces. Planta 202:1–8. doi: 10.1007/s004250050096

10. Parker AR, Lawrence CR (2001) Water capture by a desert beetle. Nature 414:33–34. doi: 10.1038/35102108

11. Parker AR, Townley HE (2007) Biomimetics of photonic nanostructures. Nat Nanotechnol 2:347–353. doi: 10.1038/nnano.2007.152

12. Luo Y, Liu Y, Anderson J, et al (2015) Improvement of water-repellent and hydrodynamic drag reduction properties on bio-inspired surface and exploring sharkskin effect mechanism. Appl Phys A Mater Sci Process 120:369–377. doi: 10.1007/s00339-015-9198-9

13. Autumn K, Liang Y a, Hsieh ST, et al (2000) Adhesive force of a single gecko foot-hair. Nature 405:681–685.

14. Federle W, Barnes WJP, Baumgartner W, et al (2006) Wet but not slippery: Boundary friction in tree frog adhesive toe pads. J R Soc Interface 3:689–697. doi: 10.1098/rsif.2006.0135

15. Varenberg M, Pugno NM, Gorb SN (2010) Spatulate structures in biological fibrillar adhesion. Soft Matter 6:3269. doi: 10.1039/c003207g

16. Spolenak R, Gorb S, Gao H, Arzt E (2005) Effects of contact shape on the scaling of biological attachments. Proc R Soc A Math Phys Eng Sci 461:305–319. doi: 10.1098/rspa.2004.1326

17. Dirks JH, Li M, Kabla A, Federle W (2012) In vivo dynamics of the internal fibrous structure in smooth adhesive pads of insects. Acta Biomater 8:2730–2736. doi: 10.1016/j.actbio.2012.04.008

18. Lin H, Qu Z, Meredith JC (2016) Pressure Sensitive Microparticle Adhesion through Biomimicry of the Pollen-Stigma Interaction. Soft Matter 12:2965–2975. doi: 10.1039/C5SM02845K

19. Edlund AF, Swanson R, Preuss D (2004) Pollen and Stigma Structure and Function: The Role of Diversity in Pollination. Plant Cell 16:S84–S97. doi: 10.1105/tpc.015800

20. Hamaker HC (1937) The London—van der Waals attraction between spherical particles. Physica 4:1058–1072.

21. Butt H-J, Kappl M (2009) Normal capillary forces. Adv Colloid Interface Sci 146:48–60. doi: 10.1016/j.cis.2008.10.002

22. Mehrotra VP, Sastry KVS (1980) Pendular bond strength between unequal-sized spherical particles. Powder Technol 25:203–214. doi: 10.1016/0032-5910(80)87031-8

23. Gu Y, Li D (1999) The van der Waals Interaction between a Spherical Particle and a Cylinder. J Colloid Interface Sci 217:60–69. doi: 10.1006/jcis.1999.6349

24. Hartmann U (1991) Van der Waals interactions between sharp probes and flat sample surfaces. Phys Rev B 43:2404–2407. doi: 10.1103/PhysRevB.43.2404

25. Tselishchev YG, Val'tsifer VA (2003) Influence of the type of contact between particles joined by a liquid bridge on the capillary cohesive forces. Colloid J Russ Acad Sci Kolloidn Zhurnal 65:385–389. doi: 10.1023/A:1024275327145

26. Tadmor R (2001) The London-van der Waals interaction energy between objects of various geometries. J Phys Condens Matter 13:L195–L202. doi: 10.1088/0953-8984/13/9/101

27. Gorb SN (2008) Biological attachment devices: exploring nature's diversity for biomimetics. Philos Trans A Math Phys Eng Sci 366:1557–74. doi: 10.1098/rsta.2007.2172

28. Gorb SN (2011) Biological fibrillar adhesives: functional principles and biomimetic applications. Handb Adhes Technol 1409–1436. doi: 10.1007/978-3-642-01169-6_54

29. Derks D, Lindner A, Creton C, Bonn D (2003) Cohesive failure of thin layers of soft model adhesives under tension. J Appl Phys 93:1557–1566. doi: 10.1063/1.1533095

30. Croll S (2002) DLVO theory applied to TiO2 pigments and other materials in latex paints. Prog Org Coatings 44:131–146. doi: 10.1016/S0300-9440(01)00261-2

31. Lin L (2003) Mechanisms of pigment dispersion. Pigment Resin Technol 32:78–88. doi: 10.1108/03699420310464784

32. Leite FL, Bueno CC, Da Róz AL, et al (2012) Theoretical models for surface forces and adhesion and their measurement using atomic force microscopy. Int J Mol Sci. doi: 10.3390/ijms131012773

33. Israelachvili JN (2010) Intermolecular and Surface Forces Third Edition. Acad Press 710. doi: 10.1016/B978-0-12-375182-9.10025-9

34. Hertz H (1896) Miscellaneous papers. Macmillan, London, UK

35. Johnson KL, Kendall K, Roberts AD (1971) Surface Energy and the Contact of Elastic Solids. Proc R Soc A Math Phys Eng Sci 324:301–313. doi: 10.1098/rspa.1971.0141

36. Grierson DS, Flater EE, Carpick RW (2005) Accounting for the JKR-DMT transition in adhesion and friction measurements with atomic force microscopy. J Adhes Sci Technol 19:291–311. doi: 10.1163/1568561054352685

37. Kamperman M, Kroner E, Del Campo A, et al (2010) Functional adhesive surfaces with “Gecko” effect: The concept of contact splitting. Adv Eng Mater 12:335–348. doi: 10.1002/adem.201000104

38. Derjaguin B V., Muller VM, Toporov YP (1975) Effect of contact deformations on the adhesion of particles. J Colloid Interface Sci 53:314–326. doi: 10.1016/0021-9797(75)90018-1

39. Götzinger M, Peukert W (2004) Particle adhesion force distributions on rough surfaces. Langmuir 20:5298–5303. doi: 10.1021/la049914f

40. Rabinovich YI, Adler JJ, Ata A, et al (2000) Adhesion between Nanoscale Rough Surfaces. J Colloid Interface Sci 232:10–16. doi: 10.1006/jcis.2000.7167

41. Fuller KNG, Tabor D (1975) The Effect of Surface Roughness on the Adhesion of Elastic Solids. Proc R Soc A Math Phys Eng Sci 345:327–342. doi: 10.1098/rspa.1975.0138

42. Persson BNJ, Tosatti E (2001) The effect of surface roughness on the adhesion of elastic solids. J Chem Phys 115:5597–5610. doi: 10.1063/1.1398300

43. Rumpf H (1974) Die Wissenschaft des Agglomerierens. Chemie Ing Tech 46:1–11. doi: 10.1002/cite.330460102

44. Gao H, Yao H (2004) Shape insensitive optimal adhesion of nanoscale fibrillar structures. Proc Natl Acad Sci U S A 101:7851–6. doi: 10.1073/pnas.0400757101

45. Eichenlaub S, Kumar G, Beaudoin S (2006) A modeling approach to describe the adhesion of rough, asymmetric particles to surfaces. J Colloid Interface Sci 299:656–664. doi: 10.1016/j.jcis.2006.03.010

46. Prokopovich P, Starov V (2011) Adhesion models: From single to multiple asperity contacts. Adv Colloid Interface Sci 168:210–222. doi: 10.1016/j.cis.2011.03.004

47. Yu J, Chary S, Das S, et al (2012) Friction and adhesion of Gecko-Inspired PDMS flaps on rough surfaces. Langmuir 28:11527–11534. doi: 10.1021/la301783q

48. Cai S, Bhushan B (2007) Meniscus and viscous forces during normal separation of liquid-mediated contacts. Nanotechnology 18:465704. doi: 10.1088/0957-4484/18/46/465704

49. Dirks J-H, Federle W (2011) Fluid-based adhesion in insects – principles and challenges. Soft Matter 7:11047. doi: 10.1039/c1sm06269g

50. Dirks JH (2014) Physical principles of fluid-mediated insect attachment-Shouldn't insects slip? Beilstein J Nanotechnol 5:1160–1166. doi: 10.3762/bjnano.5.127

51. Orr FM, Scriven LE, Rivas AP (1975) Pendular rings between solids: meniscus properties and capillary force. J Fluid Mech 67:723. doi: 10.1017/S0022112075000572

52. Matthewson MJ (1988) Adhesion of spheres by thin liquid films. Philos Mag A 57:207–216. doi: 10.1080/01418618808204510

53. Ata A, Rabinovich Y, Singh R (2002) Role of surface roughness in capillary adhesion. J Adhes Sci Technol 4243:37–41. doi: 10.1163/156856102760067145

54. Willett CD, Adams MJ, Johnson SA, Seville JPK (2000) Capillary bridges between two spherical bodies. Langmuir 16:9396–9405. doi: 10.1021/la000657y

55. Rabinovich YI, Esayanur MS, Moudgil BM (2005) Capillary forces between two spheres with a fixed volume liquid bridge: Theory and experiment. Langmuir 21:10992–10997. doi: 10.1021/la0517639

56. Bhushan B (2003) Adhesion and stiction: Mechanisms, measurement techniques, and methods for reduction. J Vac Sci Technol B Microelectron Nanom Struct 21:2262. doi: 10.1116/1.1627336

57. Lee T, Charrault E, Neto C (2014) Interfacial slip on rough, patterned and soft surfaces: A review of experiments and simulations. Adv Colloid Interface Sci 210:21–38. doi: 10.1016/j.cis.2014.02.015

58. Mongruel A, Chastel T, Asmolov ES, Vinogradova OI (2013) Effective hydrodynamic boundary conditions for microtextured surfaces. Phys Rev E - Stat Nonlinear, Soft Matter Phys 87:1–4. doi: 10.1103/PhysRevE.87.011002

59. Kunert C, Harting J, Vinogradova OI (2010) Random-roughness hydrodynamic boundary conditions. Phys Rev Lett 105:2–5. doi: 10.1103/PhysRevLett.105.016001

60. Maali A, Pan Y, Bhushan B, Charlaix E (2012) Hydrodynamic drag-force measurement and slip length on microstructured surfaces. Phys Rev E - Stat Nonlinear, Soft Matter Phys 85:1–5. doi: 10.1103/PhysRevE.85.066310

61. Vinogradova OI (1995) Drainage of a Thin Liquid Film Confined between Hydrophobic Surfaces. Langmuir 11:2213–2220. doi: 10.1021/la00006a059

62. Pilkington GA, Gupta R, Fréchette J (2016) Scaling Hydrodynamic Boundary Conditions of Microstructured Surfaces in the Thin Channel Limit. Langmuir 32:2360–2368. doi: 10.1021/acs.langmuir.5b04134

63. Nizkaya T V, Dubov AL, Mourran A, Vinogradova OI (2016) Probing effective slippage on superhydrophobic surfaces by atomic force microscopy. Soft Matter 12:6910–6917. doi: 10.1039/C6SM01074A

64. Creton C, Gorb SN (2007) Sticky Feet : From Animals to Materials. MRS Bull 32:466–472.

65. Huber G, Gorb SN, Hosoda N, et al (2007) Influence of surface roughness on gecko adhesion. Acta Biomater 3:607–610. doi: 10.1016/j.actbio.2007.01.007

66. Lake GJ, Thomas AG (1967) The Strength of Highly Elastic Materials. Proc R Soc A Math Phys Eng Sci 300:108–119. doi: 10.1098/rspa.1967.0160

67. Arzt E, Gorb S, Spolenak R (2003) From micro to nano contacts in biological attachment devices. Proc Natl Acad Sci U S A 100:10603–6. doi: 10.1073/pnas.1534701100

68. Peattie AM, Full RJ (2007) Phylogenetic analysis of the scaling of wet and dry biological fibrillar adhesives. Proc Natl Acad Sci 104:18595–18600. doi: 10.1073/pnas.0707591104

69. Labonte D, Clemente CJ, Dittrich A, et al (2016) Extreme positive allometry of animal adhesive pads and the size limits of adhesion-based climbing. Proc Natl Acad Sci 113:201519459. doi: 10.1073/pnas.1519459113

70. Gao H, Wang X, Yao H, et al (2005) Mechanics of hierarchical adhesion structures of geckos. Mech Mater 37:275–285. doi: 10.1016/j.mechmat.2004.03.008

71. Bullock JMR, Drechsler P, Federle W (2008) Comparison of smooth and hairy attachment pads in insects: friction, adhesion and mechanisms for direction-dependence. J Exp Biol 211:3333–3343. doi: 10.1242/jeb.020941

72. Autumn K, Sitti M, Liang Y a, et al (2002) Evidence for van der Waals adhesion in gecko setae. Proc Natl Acad Sci U S A 99:12252–6. doi: 10.1073/pnas.192252799

73. Bhushan B, Sayer R a (2007) Gecko Feet : Natural Attachment Systems for Smart Adhesion. Appl Scanning Probe Methods VII 41–76. doi: 10.1007/11785705

74. Autumn K, Majidi C, Groff RE, et al (2006) Effective elastic modulus of isolated gecko setal arrays. J Exp Biol 209:3558–68. doi: 10.1242/jeb.02469

75. Tian Y, Pesika N, Zeng H, et al (2006) Adhesion and friction in gecko toe attachment and detachment. Proc Natl Acad Sci U S A 103:19320–19325. doi: 10.1073/pnas.0608841103

76. Drechsler P, Federle W (2006) Biomechanics of smooth adhesive pads in insects: Influence of tarsal secretion on attachment performance. J Comp Physiol A

Neuroethol Sensory, Neural, Behav Physiol 192:1213–1222. doi: 10.1007/s00359-006-0150-5

77. Gorb E V, Hosoda N, Miksch C, Gorb SN (2010) Slippery pores: anti-adhesive effect of nanoporous substrates on the beetle attachment system. J R Soc Interface 7:1571–1579. doi: 10.1098/rsif.2010.0081

78. De Souza EJ, Brinkmann M, Mohrdieck C, Arzt E (2008) Enhancement of capillary forces by multiple liquid bridges. Langmuir 24:8813–8820. doi: 10.1021/la8005376

79. Su Y, Ji B, Huang Y, Hwang K (2007) Effects of contact shape on biological wet adhesion. J Mater Sci 42:8885–8893. doi: 10.1007/s10853-007-1759-7

80. Gorb S, Varenberg M (2007) Mushroom-shaped geometry of contact elements in biological adhesive systems. J Adhes Sci Technol 21:1175–1183. doi: 10.1163/156856107782328317

81. Barnes WJP (2007) Functional morphology and design constraints of smooth adhesive pads. MRS Bull 32:479–485. doi: 10.1557/mrs2007.81

82. Barnes WJP, Goodwyn PJP, Nokhbatolfoghahai M, Gorb SN (2011) Elastic modulus of tree frog adhesive toe pads. J Comp Physiol A Neuroethol Sensory, Neural, Behav Physiol 197:969–978. doi: 10.1007/s00359-011-0658-1

83. Scholz I, Barnes WJP, Smith JM, Baumgartner W (2009) Ultrastructure and physical properties of an adhesive surface, the toe pad epithelium of the tree frog, Litoria caerulea White. J Exp Biol 212:155–162. doi: 10.1242/jeb.019232

84. Barnes WJP, Oines C, Smith JM (2006) Whole animal measurements of shear and adhesive forces in adult tree frogs: Insights into underlying mechanisms of adhesion obtained from studying the effects of size and scale. J Comp Physiol A Neuroethol Sensory, Neural, Behav Physiol 192:1179–1191. doi: 10.1007/s00359-006-0146-1

85. Iturri J, Xue L, Kappl M, et al (2015) Torrent frog-inspired adhesives: Attachment to flooded surfaces. Adv Funct Mater 25:1499–1505. doi: 10.1002/adfm.201403751

86. Endlein T, Barnes WJP, Samuel DS, et al (2013) Sticking under Wet Conditions: The Remarkable Attachment Abilities of the Torrent Frog, Staurois guttatus. PLoS One. doi: 10.1371/journal.pone.0073810

87. Dirks J-H, Clemente CJ, Federle W (2010) Insect tricks: two-phasic foot pad secretion prevents slipping. J R Soc Interface 7:587–593. doi: 10.1098/rsif.2009.0308

88. Labonte D, Federle W (2015) Rate-dependence of "wet" biological adhesives and the function of the pad secretion in insects. Soft Matter 11:8661–8673. doi: 10.1039/C5SM01496D

89. Thio BJR, Lee JH, Meredith JC (2009) Characterization of ragweed pollen adhesion to polyamides and polystyrene using atomic force microscopy. Environ Sci Technol 43:4308–4313.

90. Lin H, Lizarraga L, Bottomley L a, Carson Meredith J (2015) Effect of water absorption on pollen adhesion. J Colloid Interface Sci 442:133–9. doi: 10.1016/j.jcis.2014.11.065

91. Zinkl GM, Zwiebel BI, Grier DG, Preuss D (1999) Pollen-stigma adhesion in Arabidopsis: a species-specific interaction mediated by lipophilic molecules in the pollen exine. Development 126:5431–5440.

92. Luu DT, Passelègue E, Dumas C, Heizmann P (1998) Pollen-stigma capture is not species discriminant within the Brassicaceae family. Comptes Rendus l'Academie des Sci - Ser III 321:747–755. doi: 10.1016/S0764-4469(98)80015-2

93. Cho WK, Ankrum J a, Guo D, et al (2012) Microstructured barbs on the North American porcupine quill enable easy tissue penetration and difficult removal. Proc Natl Acad Sci U S A 109:21289–94. doi: 10.1073/pnas.1216441109

94. Ling J, Jiang L, Chen K, et al (2016) Insertion and Pull Behavior of Worker Honeybee Stinger. J Bionic Eng 13:303–311. doi: 10.1016/S1672-6529(16)60303-7

95. Lin H, Gomez I, Meredith JC (2013) Pollenkitt wetting mechanism enables species-specific tunable pollen adhesion. Langmuir 29:3012–3023.

96. Zhao Z-L, Zhao H-P, Ma G-J, et al (2015) Structures, properties, and functions of the stings of honey bees and paper wasps: a comparative study. Biol Open 4:921–8. doi: 10.1242/bio.012195

97. Yang SY, O'Cearbhaill ED, Sisk GC, et al (2013) A bio-inspired swellable microneedle adhesive for mechanical interlocking with tissue. Nat Commun 4:1702. doi: 10.1038/ncomms2715

98. Ott ML, Mizes HA (1994) Atomic force microscopy adhesion measurements of surface-modified toners for xerographic applications. Colloids Surfaces A Physicochem Eng Asp 87:245–256. doi: 10.1016/0927-7757(94)80072-3

99. Richard Bowen W, Doneva T (2000) Atomic Force Microscopy Studies of Membranes: Effect of Surface Roughness on Double-Layer Interactions and Particle Adhesion. J Colloid Interface Sci 229:544–549. doi: 10.1006/jcis.2000.6997

100. Cooper K, Gupta A, Beaudoin S (2001) Simulation of the Adhesion of Particles to Surfaces. J Colloid Interface Sci 234:284–292. doi: 10.1006/jcis.2000.7276

101. Meitl M a., Zhu Z-T, Kumar V, et al (2006) Transfer printing by kinetic control of adhesion to an elastomeric stamp. Nat Mater 5:33–38. doi: 10.1038/nmat1532

102. Mitragotri S, Lahann J (2009) Physical approaches to biomaterial design. Nat Mater 8:15–23. doi: 10.1038/nmat2344

103. Huang Y, Liu M, Wang J, et al (2011) Controllable underwater oil-adhesion-interface films assembled from nonspherical particles. Adv Funct Mater 21:4436–4441. doi: 10.1002/adfm.201101598

104. Fischer KE, Nagaraj G, Hugh Daniels R, et al (2011) Hierarchical nanoengineered surfaces for enhanced cytoadhesion and drug delivery. Biomaterials 32:3499–3506. doi: 10.1016/j.biomaterials.2011.01.022

105. Zhang L, Shi J, Jiang Z, et al (2011) Facile preparation of robust microcapsules by manipulating metal-coordination interaction between biomineral layer and bioadhesive layer. ACS Appl Mater Interfaces 3:597–605. doi: 10.1021/am101184h

106. Stassi S, Canavese G (2012) Spiky nanostructured metal particles as filler of polymeric composites showing tunable electrical conductivity. J Polym Sci Part B Polym Phys 50:984–992. doi: 10.1002/polb.23091

107. Lee I (2013) Molecular self-assembly: Smart design of surface and interface via secondary molecular interactions. Langmuir 29:2476–2489. doi: 10.1021/la304123b

108. Wen W, Wang N, Zheng DW, et al (1999) Two-and three-dimensional arrays of magnetic microspheres. J Mater Res 14:1186–1189.

109. Maugis D (1992) Adhesion of spheres: The JKR-DMT transition using a dugdale model. J Colloid Interface Sci 150:243–269. doi: 10.1016/0021-9797(92)90285-T

110. Ducker WA, Senden TJ, Pashley RM (1991) Direct measurement of colloidal forces using an atomic force microscope. Nature 353:239–241. doi: 10.1063/1.344961

111. Muller VM, Yushchenko VS, Derjaguin B V. (1994) On the influence of molecular forces on the deformation of an elastic sphere and its sticking to a rigid plane. Prog Surf Sci 45:157–167. doi: 10.1016/0079-6816(94)90048-5

112. Tabor D (1977) Surface forces and surface interactions. J Colloid Interface Sci 58:2–13. doi: 10.1016/0021-9797(77)90366-6

113. Maugis D, Pollock HM (1984) Surface forces, deformation and adherence at metal microcontacts. Acta Metall 32:1323–1334. doi: 10.1016/0001-6160(84)90078-6

114. Rimai DS, Dejesus M, Weiss D (2008) The effect of surface-adhering nanoclusters on the adhesion and cohesion of micrometer-size particles. J Adhes Sci Technol 22:529–543. doi: 10.1163/156856108x295572

115. Horn E (1933) A Summer Hay Fever Plant Survey of Manhattan, Kansas. Trans Kansas Acad Sci 36:91–97.

116. Ressayre A, Godelle B, Raquin C, Gouyon PH (2002) Aperture pattern ontogeny in angiosperms. J Exp Zool 294:122–135. doi: 10.1002/jez.10150

117. Ziska LH, Gebhard DE, Frenz DA, et al (2003) Cities as harbingers of climate change: Common ragweed, urbanization, and public health. J Allergy Clin Immunol 111:290–295. doi: 10.1067/mai.2003.53

118. Fumanal B, Chauvel B, Bretagnolle F (2007) Estimation of pollen and seed production of common ragweed in France. Ann Agric Environ Med 14:233–236. doi: 10.1089/eco.2009.0025

119. Bajin MD, Cingi C, Oghan F, Gurbuz MK (2013) Global warming and allergy in Asia Minor. Eur Arch Oto-Rhino-Laryngology 270:27–31. doi: 10.1007/s00405-012-2073-9

120. Beggs PJ (2004) Impacts of climate change on aeroallergens: Past and future. Clin Exp Allergy 34:1507–1513. doi: 10.1111/j.1365-2222.2004.02061.x

121. Rogers CA, Wayne PM, Macklin EA, et al (2006) Interaction of the onset of spring and elevated atmospheric CO2 on ragweed (Ambrosia artemisiifolia L.) pollen production. Environ Health Perspect 114:865–869. doi: 10.1289/ehp.8549

122. Hesse M, Zetter R, Buchner R, et al (2009) Pollen Terminology : An illustrated handbook. Vienna : Springer Vienna

123. Ziska L, Knowlton K, Rogers C, et al (2011) Recent warming by latitude associated with increased length of ragweed pollen season in central North America. Proc Natl Acad Sci U S A 108:4248–51. doi: 10.1073/pnas.1014107108

124. Botanical M, Press G, Garden MB (2010) The Bases of Angiosperm Phylogeny : Palynology Author (s): James W . Walker and James A . Doyle Source : Annals of the Missouri Botanical Garden , Vol . 62 , No . 3 , The Bases of Angiosperm Published by : Missouri Botanical Garden Press Stable URL : ht. Garden 62:664–723.

125. Grater WC, Stemen TR (1967) The Plant, the Pollen and the Patient. Rev Palaeobot Palynol 4:187–192.

126. Ichinose I, Senzu H (1997) A Surface Sol-Gel Process of TiO 2 and Other Metal Oxide Films with Molecular. Chem Mater 4756:1296–1298. doi: 10.1021/cm970008g

127. Brandon Goodwin W, Gomez IJ, Fang Y, et al (2013) Conversion of pollen particles into three-dimensional ceramic replicas tailored for multimodal adhesion. Chem Mater 25:4529–4536. doi: 10.1021/cm402226w

128. Ichinose I, Senzu H, Kunitake T (1996) Stepwise adsorption of metal alkoxides on hydrolyzed surfaces: A surface sol-gel process. Chem Lett 831–832. doi: Doi 10.1246/Cl.1996.831

129. Cao F, Li D-X (2009) Morphology-controlled synthesis of SiO2 hollow microspheres using pollen grain as a biotemplate. Biomed Mater 4:25009. doi: 10.1088/1748-6041/4/2/025009

130. Hall SR, Bolger H, Mann S (2003) Morphosynthesis of complex inorganic forms using pollen grain templates. Chem Commun (Camb) 44:2784–2785. doi: 10.1039/b309877j

131. Wang Y, Liu Z, Han B, et al (2005) Replication of biological organizations through a supercritical fluid route. Chem Commun 2948–50. doi: 10.1039/b502491a

132. Yang X, Song X, Wei Y, et al (2011) Synthesis of spinous ZrO2 core-shell microspheres with good hydrogen storage properties by the pollen bio-template route. Scr Mater 64:1075–1078. doi: 10.1016/j.scriptamat.2011.02.015

133. Rosi NL, Thaxton CS, Mirkin CA (2004) Control of nanoparticle assembly by using DNA-modified diatom templates. Angew Chemie - Int Ed 43:5500–5503. doi: 10.1002/anie.200460905

134. Gaddis CS, Sandhage KH (2004) Freestanding microscale 3D polymeric structures with biologically-derived shapes and nanoscale features. J Mater Res 19:2541–2545. doi: 10.1557/JMR.2004.0342

135. Zhao J, Gaddis CS, Cai Y, Sandhage KH (2005) Free-standing microscale structures of nanocrystalline zirconia with biologically replicable three-dimensional shapes. J Mater Res 20:282–287. doi: 10.1557/JMR.2005.0046

136. Anderson MW, Holmes SM, Hanif N, Cundy CS (2000) Hierarchical pore structures through diatom zeolitization. Angew Chemie - Int Ed 39:2707–2710. doi: 10.1002/1521-3773(20000804)39:15<2707::AID-ANIE2707>3.0.CO;2-M

137. Weatherspoon MR, Dickerson MB, Wang G, et al (2007) Thin, conformal, and continuous SnO2 coatings on three-dimensional biosilica templates through hydroxy-group amplification and layer-by-layer alkoxide deposition. Angew Chemie - Int Ed 46:5724–5727. doi: 10.1002/anie.200701297

138. Weatherspoon MR, Cai Y, Crne M, et al (2008) 3D rutile titania-based structures with Morpho butterfly wing scale morphologies. Angew Chemie - Int Ed 47:7921–7923. doi: 10.1002/anie.200801311

139. Fransen MJ (2005) On The Influence of Generator and Detector Settings in X-ray Powder Diffractometry. Adcancs X-ray Anal 48:143–149. doi: 10.1081/E-EPT-100200014

140. Goodwin WB (2015) Controlled modulation of short-and long-range adhesion of microscale biogenic replicas. Georgia Institute of Technology

141. Van Raap MBF, Zélis PM, Coral DF, et al (2012) Self organization in oleic acid-Coated CoFe 2O 4 colloids: A SAXS study. J Nanoparticle Res 14:1072. doi: 10.1007/s11051-012-1072-5

142. Sato Turtelli R, Duong G V., Nunes W, et al (2008) Magnetic properties of nanocrystalline CoFe2O4 synthesized by modified citrate-gel method. J Magn Magn Mater 320:339–342. doi: 10.1016/j.jmmm.2008.02.067

143. Kumar V, Rana A, Yadav MS, Pant RP (2008) Size-induced effect on nano-crystalline CoFe2O4. J Magn Magn Mater 320:1729–1734. doi: 10.1016/j.jmmm.2008.01.021

144. Cai S, Bhushan B (2007) Meniscus and viscous forces during normal separation of liquid-mediated contacts. Nanotechnology 18:465704. doi: 10.1088/0957-4484/18/46/465704

145. Palacio M, Bhushan B (2008) Ultrathin Wear-Resistant Ionic Liquid Films for Novel MEMS/NEMS Applications. Adv Mater 20:1194–1198. doi: 10.1002/adma.200702006

146. Pitois O, Moucheront P, Chateau X (2000) Liquid Bridge between Two Moving Spheres: An Experimental Study of Viscosity Effects. J Colloid Interface Sci 231:26–31. doi: 10.1006/jcis.2000.7096

147. Pacini E, Hesse M (2005) Pollenkitt – its composition, forms and functions. Flora - Morphol Distrib Funct Ecol Plants 200:399–415. doi: 10.1016/j.flora.2005.02.006

148. Sahni V, Blackledge T a, Dhinojwala A (2010) Viscoelastic solids explain spider web stickiness. Nat Commun 1:19. doi: 10.1038/ncomms1019

149. Eisner T, Aneshansley DJ (2000) Defense by foot adhesion in a beetle (Hemisphaerota cyanea). Proc Natl Acad Sci 97:6568–6573. doi: 10.1073/pnas.97.12.6568

150. Persson BNJ (2007) Wet adhesion with application to tree frog adhesive toe pads and tires. J Phys Condens Matter 19:376110. doi: 10.1088/0953-8984/19/37/376110

151. Huber G, Mantz H, Spolenak R, et al (2005) Evidence for capillarity contributions to gecko adhesion from single spatula nanomechanical measurements. Proc Natl Acad Sci U S A 102:16293–6. doi: 10.1073/pnas.0506328102

152. Grof Z, Lawrence CJ, Stepánek F (2008) The strength of liquid bridges in random granular materials. J Colloid Interface Sci 319:182–92. doi: 10.1016/j.jcis.2007.11.055

153. Mate CM, Novotny VJ (1991) Molecular conformation and disjoining pressure of polymeric liquid films. J Chem Phys 94:8420. doi: 10.1063/1.460075

154. Mullins BJ, Agranovski IE, Braddock RD (2003) Particle Bounce During Filtration of Particles on Wet and Dry Filters. Aerosol Sci Technol 37:587–600. doi: 10.1080/02786820300923

155. Eichelsdoerfer DJ, Brown K a, Mirkin C a (2014) Capillary bridge rupture in dip-pen nanolithography. Soft Matter 10:5603–8. doi: 10.1039/c4sm00997e

156. Schu S, Geiser M, Lee MM, et al (1999) Particles at the airway interfaces of the lung. Colloids Surfaces B Biointerfaces 15:339–353. doi: 10.1016/S0927-7765(99)00099-5

157. Orr FM, Scriven LE, Rivas a. P (2006) Pendular rings between solids: meniscus properties and capillary force. J Fluid Mech 67:723. doi: 10.1017/S0022112075000572

158. Matthewson MJ (1988) Adhesion of spheres by thin liquid films. Philos Mag A 57:207–216. doi: 10.1080/01418618808204510

159. Ally J, Vittorias E, Amirfazli a, et al (2010) Interaction of a microsphere with a solid-supported liquid film. Langmuir 26:11797–803. doi: 10.1021/la1010924

160. Bowen J, Cheneler D, Andrews JW, et al (2011) Application of colloid probe atomic force microscopy to the adhesion of thin films of viscous and viscoelastic silicone fluids. Langmuir 27:11489–500. doi: 10.1021/la202060f

161. Langer MG, Ruppersberg JP, Gorb S (2004) Adhesion forces measured at the level of a terminal plate of the fly's seta. Proc Biol Sci 271:2209–15. doi: 10.1098/rspb.2004.2850

162. Labonte D, Williams J a, Federle W (2014) Surface contact and design of fibrillar "friction pads" in stick insects (Carausius morosus): mechanisms for large friction coefficients and negligible adhesion. J R Soc Interface 11:20140034. doi: 10.1098/rsif.2014.0034

163. Peattie AM, Dirks J-H, Henriques S, Federle W (2011) Arachnids Secrete a Fluid over Their Adhesive Pads. PLoS One 6:e20485. doi: 10.1371/journal.pone.0020485

164. Scientific E, Company P, Hesse M (1981) The Fine Structure of the Exine in Relation to the Stickness of Angiosperm Pollen. Rev Palaeobot Palynol 35:81–92.

165. Culley TM, Weller SG, Sakai AK (2002) The evolution of wind pollination in angiosperms. Trends Ecol Evol 17:361–369. doi: 10.1016/S0169-5347(02)02540-5

166. Domínguez E, Mercado JA, Quesada MA, Heredia A (1999) Pollen sporopollenin : degradation and structural elucidation. Sex Plant Reprod 12:171–178.

167. Dobson H (1988) Survey of Pollen and Pollenkitt Lipids--Chemical Cues to Flower Visitors? Am J Bot 75:170–182. doi: 10.2307/2443884

168. Burnham N a, Chen X, Hodges CS, et al (2003) Comparison of calibration methods for atomic-force microscopy cantilevers. Nanotechnology 14:1–6. doi: 10.1088/0957-4484/14/1/301

169. Hutter JL, Bechhoefer J (1993) Calibration of atomic-force microscope tips. Rev Sci Instrum 64:1868. doi: 10.1063/1.1143970

170. Xiao X, Qian L (2000) Investigation of Humidity-Dependent Capillary Force. Langmuir 16:8153–8158. doi: 10.1021/la000770o

171. Chan DYC, Horn RG (1985) The drainage of thin liquid films between solid surfaces. J Chem Phys 83:5311. doi: 10.1063/1.449693

172. Boucher EA, Kent HJ (1977) Capillary Phenomena. J Chem Soc Faraday Trans 1 73:1882–1890.

173. Beer T (2013) Beaufort Wind Scale. Encycl Nat Hazards 42–45.

174. Gravish N, Wilkinson M, Sponberg S, et al (2010) Rate-dependent frictional adhesion in natural and synthetic gecko setae. J R Soc Interface 7:259–269.

175. Amarpuri G, Chaurasia V, Jain D, et al (2015) Ubiquitous distribution of salts and proteins in spider glue enhances spider silk adhesion. Sci Rep 5:9030. doi: 10.1038/srep09030

176. Lee H, Dellatore SM, Miller WM, Messersmith PB (2007) Mussel-inspired surface chemistry for multifunctional coatings. Science 318:426–430. doi: 10.1126/science.1147241

177. Boesel LF, Cremer C, Arzt E, Campo A Del (2010) Gecko-inspired surfaces: A path to strong and reversible dry adhesives. Adv Mater 22:2125–2137. doi: 10.1002/adma.200903200

178. Song Y, Dai Z, Wang Z, et al (2016) The synergy between the insect-inspired claws and adhesive pads increases the attachment ability on various rough surfaces. Sci Rep 6:26219. doi: 10.1038/srep26219

179. Creton C, Gorb S (2007) S ticky Feet : From Animals to Materials Overview : Reversible Adhesion. MRS Bull 32:466–472.

180. Dezfuli BS, Lui A, Giari L, et al (2008) Ultrastructural study on the body surface of the acanthocephalan parasite Dentitruncus truttae in brown trout. Microsc Res Tech 71:230–235. doi: 10.1002/jemt.20543

181. Gorb SN, Sinha M, Peressadko A, et al (2007) Insects did it first: a micropatterned adhesive tape for robotic applications. Bioinspir Biomim 2:S117–S125. doi: 10.1088/1748-3182/2/4/S01

182. Yang K, Wu D, Ye X, et al (2013) Characterization of chemical composition of bee pollen in China. J Agric Food Chem 61:708–718. doi: 10.1021/jf304056b

183. Vaissière BE, Vinson SB (1994) Pollen morphology and its effect on pollen collection by honey bees, Apis Mellifera L. (Hymenoptera: Apidae), with special Reference to Upland Cotton, Gossypium Hirsutum L. (Malvaceae). Grana 33:128–138. doi: 10.1080/00173139409428989

184. Cane JH (2008) Bees (Hymenoptera : Apoidea : Apiformes). Encycl Entomol 2:419–434.

185. Mares S, Ash L, Gronenberg W (2005) Brain allometry in bumblebee and honey bee workers. Brain Behav Evol 66:50–61. doi: 10.1159/000085047

186. Menzel R, Greggers U, Smith A, et al (2005) Honey bees navigate according to a map-like spatial memory. Proc Natl Acad Sci U S A 102:3040–3045. doi: 10.1073/pnas.0408550102

187. Komosinska-Vassev K, Olczyk P, Kaźmierczak J, et al (2015) Bee pollen: Chemical composition and therapeutic application. Evidence-based Complement Altern Med. doi: 10.1155/2015/297425

188. Campos MGR, Bogdanov S, Bicudo De Almeida-Muradian L, et al (2008) Pollen composition and standardisation of analytical methods. J Apic Res Bee World 47:156–163. doi: 10.3896/IBRA.1.47.2.12

189. Tan KT, Vogt BD, White CC, et al (2008) On the origins of sudden adhesion loss at a critical relative humidity: Examination of bulk and interfacial contributions. Langmuir 24:9189–9193. doi: 10.1021/la800632r

190. White C, Tan KT, Hunston D, et al (2015) Mechanisms of criticality in environmental adhesion loss. Soft Matter 11:3994–4001. doi: 10.1039/C4SM02725F

191. Puthoff JB, Prowse MS, Wilkinson M, Autumn K (2010) Changes in materials properties explain the effects of humidity on gecko adhesion. J Exp Biol 213:3699–704. doi: 10.1242/jeb.047654

192. Peisker H, Michels J, Gorb SN (2013) Evidence for a material gradient in the adhesive tarsal setae of the ladybird beetle Coccinella septempunctata. Nat Commun 4:1661. doi: 10.1038/ncomms2576

193. Amarpuri G, Zhang C, Diaz C, et al (2015) Spiders Tune Glue Viscosity to Maximize Adhesion. ACS Nano 9:11472–11478. doi: 10.1021/acsnano.5b05658

194. Chen Y, Shih M, Wu M, et al (2014) Underwater attachment using hairs: the functioning of spatula and sucker setae from male diving beetles. J R Soc Interface. doi: 10.1098/rsif.2014.0273

195. Haydak M (1970) Honey Bee Nutrition1. Annu. Rev. Entomol.

196. Pacini E, Hesse M (2005) Pollenkitt - Its composition, forms and functions. Flora Morphol Distrib Funct Ecol Plants 200:399–415. doi: 10.1016/j.flora.2005.02.006

197. Thio BJR, Lee JH, Meredith JC (2009) Characterization of ragweed pollen adhesion to polyamides and polystyrene using atomic force microscopy. Environ Sci Technol 43:4308–4313.

198. Pöhlker C, Huffman JA, Pöschl U (2013) Autofluorescence of atmospheric bioaerosols: Spectral fingerprints and taxonomic trends of pollen. Atmos Meas Tech 6:3369–3392. doi: 10.5194/amt-6-3369-2013

199. Pierna JAF, Abbas O, Dardenne P, Baeten V (2011) Discrimination of Corsican honey by FT-Raman spectroscopy and chemometrics. Biotechnol Agron Soc Environ 15:75–84.

200. He XN, Allen J, Black PN, et al (2012) Coherent anti-Stokes Raman scattering and spontaneous Raman spectroscopy and microscopy of microalgae with nitrogen depletion. Biomed Opt Express 3:2896–906. doi: 10.1364/BOE.3.002896

201. Piskorski R, Kroder S, Dorn S (2011) Can pollen headspace volatiles and pollenkitt lipids serve as reliable chemical cues for bee pollinators? Chem Biodivers 8:577–86. doi: 10.1002/cbdv.201100014

202. Ur-Rehman S, Khan ZF, Maqbool T (2008) Physical and spectroscopic characterization of Pakistani honey. Cienc e Investig Agrar 35:161–166. doi: 10.4067/S0718-16202008000200009

203. Subrahmanyam, MSR Vedanayagam, H Sumathi Venkatacharyulu P (1994) Estimation of the sharma constant and thermoacoustic properties of vegetable oils. J Am Oil Chem Soc 71:901–905.

204. Melo-Espinosa EA, Sánchez-Borroto Y, Errasti M, et al (2014) Surface tension prediction of vegetable oils using artificial neural networks and multiple linear regression. Energy Procedia 57:886–895. doi: 10.1016/j.egypro.2014.10.298

205. Recondo MP, Elizalde BE, Buera MP (2006) Modeling temperature dependence of honey viscosity and of related supersaturated model carbohydrate systems. J Food Eng 77:126–134. doi: 10.1016/j.jfoodeng.2005.06.054

206. Sormana JL, Meredith JC (2004) High-throughput discovery of structure-mechanical property relationships for segmented poly(urethane-urea)s. Macromolecules 37:2186–2195. doi: 10.1021/ma035385v

207. Cai S, Bhushan B (2008) Meniscus and viscous forces during separation of hydrophilic and hydrophobic surfaces with liquid-mediated contacts. Mater Sci Eng R Reports 61:78–106. doi: 10.1016/j.mser.2007.03.003

208. Lin H, Allen MC, Wu J, et al (2015) Bioenabled Core/Shell Microparticles with Tailored Multimodal Adhesion and Optical Reflectivity. Chem Mater 27:7321–7330. doi: 10.1021/acs.chemmater.5b02782

209. Gomez IJ, Goodwin WB, Sabo D, et al (2015) Three-dimensional magnetite replicas of pollen particles with tailorable and predictable multimodal adhesion. J Mater Chem C 3:632–643. doi: 10.1039/C4TC01938E

210. Hu DL, Bush JWM (2005) Meniscus-climbing insects. Nature 437:733–736. doi: 10.1038/nature03995

211. Kralchevsky PA, Denkov ND (2001) Capillary forces and structuring in layers of colloid particles. Curr Opin Colloid Interface Sci 6:383–401. doi: 10.1016/S1359-0294(01)00105-4

212. Kralchevsky PA, Nagayama K (2000) Capillary interactions between particles bound to interfaces, liquid films and biomembranes. Adv Colloid Interface Sci 85:145–192. doi: 10.1016/S0001-8686(99)00016-0

213. Bowden N, Arias F, Deng T, Whitesides GM (2001) Self-assembly of microscale objects at a liquid/liquid interface through lateral capillary forces. Langmuir 17:1757–1765. doi: 10.1021/la001447o

214. Bai H, Tian X, Zheng Y, et al (2010) Direction controlled driving of tiny water drops on bioinspired artificial spider silks. Adv Mater 22:5521–5525. doi: 10.1002/adma.201003169

215. Chaudhury MK, Whitesides GM (1992) How to make water run uphill. Science 256:1539–41. doi: 10.1126/science.256.5063.1539

216. Smith JD, Dhiman R, Anand S, et al (2013) Droplet mobility on lubricant-impregnated surfaces. Soft Matter 9:1772–1780. doi: 10.1039/c2sm27032c

217. Schellenberger F, Xie J, Encinas N, et al (2015) Direct observation of drops on slippery lubricant-infused surfaces. Soft Matter 11:7617–7626. doi: 10.1039/C5SM01809A

218. Anand S, Paxson AT, Dhiman R, et al (2012) Enhanced Condensation on Lubricant- Impregnated Nanotextured Surfaces. ACS Nano 6:10122–10129. doi: 10.1021/nn303867y

219. Girifalco L a., Good RJ (1957) A theory for the estimation of surface and interfacial energies. I. Derivation and application to interfacial tension. J Phys Chem 61:904--909. doi: 10.1021/j150553a013